

Silicate Dust in Active Galactic Nuclei

DRAFT: 2018.2.22.429

Yanxia Xie^{1,2,3}, Aigen Li², and Lei Hao¹

ABSTRACT

The unification theory of active galactic nuclei (AGNs) hypothesizes that all AGNs are surrounded by an anisotropic dust torus and are essentially the same objects but viewed from different angles. However, little is known about the dust which plays a central role in the unification theory. There are suggestions that the AGN dust extinction law appreciably differs from that of the Galaxy. Also, the silicate emission features observed in type 1 AGNs appear anomalous (i.e., their peak wavelengths and widths differ considerably from that of the Galaxy). In this work, we explore the dust properties of 147 AGNs of various types at redshifts $z \lesssim 0.5$, with special attention paid to 93 AGNs which exhibit the 9.7 and 18 μm silicate emission features. We model their silicate emission spectra obtained with the *Infrared Spectrograph* aboard the *Spitzer Space Telescope*. We find that 60/93 of the observed spectra can be well explained with “astronomical silicate”, while the remaining sources favor amorphous olivine or pyroxene. Most notably, all sources require the dust to be μm -sized (with a typical size of $\sim 1.5 \pm 0.1 \mu\text{m}$), much larger than sub- μm -sized Galactic interstellar grains, implying a flat or “gray” extinction law for AGNs. We also find that, while the 9.7 μm emission feature arises predominantly from warm silicate dust of temperature $T \sim 270 \text{ K}$, the $\sim 5\text{--}8 \mu\text{m}$ continuum emission is mostly from carbon dust of $T \sim 640 \text{ K}$. Finally, the correlations between the dust properties (e.g., mass, temperature) and the AGN properties (e.g., luminosity, black hole mass) have also been investigated.

Subject headings: dust, extinction — galaxies: nuclei — (galaxies:) quasars: general — infrared: galaxies

¹Shanghai Astronomical Observatory, Chinese Academy of Sciences, 80 Nandan Road, Shanghai 200030, China; xieya@missouri.edu, hao@shao.ac.cn

²Department of Physics and Astronomy, University of Missouri, Columbia, MO 65211, USA; lia@missouri.edu

³Kavli Institute for Astronomy and Astrophysics, Peking University, Beijing 100871, China; yanxia.xie@pku.edu.cn

1. Introduction

The unification theory of active galactic nuclei (AGNs) invokes an anisotropic dusty torus to account for the observational dichotomy of AGNs (Antonucci 1993, Urry & Padovani 1995). This theory assumes that, for type 2 AGNs, the dust torus blocks the photons from the broad line region and accretion disk when they are viewed through the edge of the torus. For type 1 AGNs, the line of sight is perpendicular to the dusty torus and allows the detection of the broad emission lines. The existence of such a dust torus around AGNs has been confirmed through the detection of polarized broad emission lines in type 2 AGNs. These polarized lines are believed to arise from the otherwise-blocked broad line regions in type 2 AGNs, and they are detected just because they are scattered by dust into the viewing line-of-sight (e.g., see Antonucci & Miller 1985, Lumsden et al. 2004).

What is the AGN dust torus composed of? essentially, the torus forms out of the original interstellar matter (gas and dust) of the host galaxies of AGNs. These dust grains of interstellar origin are processed by the X-ray and ultraviolet (UV) radiation of the central engine (e.g., see Voit 1991, Li 2007). They may also undergo coagulation growth in the torus (e.g., see Maiolino et al. 2001). As amorphous silicate and some sorts of carbonaceous dust are the major dust species of interstellar grains (e.g., see Mishra & Li 2015), one naturally expects amorphous silicate dust and carbon dust (e.g., graphite, amorphous carbon) to be present in the dust torus around AGNs. According to the unification theory, type 1 AGNs are expected to show silicate emission around 9.7 and 18 μm while type 2 AGNs are expected to show silicate absorption. The detection of silicate emission in a wide variety of type 1 AGNs ranging from luminous quasars to low-luminosity Seyfert galaxies (e.g., see Hao et al. 2005a, Siebenmorgen et al. 2005, Sturm et al. 2005, Hao et al. 2007, Xie et al. 2014) as well as silicate absorption in type 2 Seyfert galaxies (e.g., see Rieke & Low 1975, Jaffe et al. 2004, Roche et al. 2007, Shi et al. 2014) and type 2 QSOs (e.g., see Sturm et al. 2006, Nikutta et al. 2009) provides further support for the unification theory of AGNs.

However, the detection of silicate emission (and absorption as well) in AGNs is found to be rather diverse among different AGN types as revealed from the rich data set obtained by the *Infrared Spectrograph* (IRS) on board the *Spitzer Space Telescope* (Houck et al. 2004). Type 1 Seyfert galaxies are found equally displaying silicate emission and weak absorption in the mid infrared (IR; Hao et al. 2007), meanwhile some type 2 AGNs exhibit silicate emission rather than absorption (e.g., see Sturm et al. 2006, Mason et al. 2009, Nikutta et al. 2009). For those in which the silicate dust is seen in emission, the silicate feature often shows an “anomalous” spectral profile: the peak wavelength of the Si–O stretching feature which has a canonical wavelength of $\sim 9.7 \mu\text{m}$ in the Milky Way diffuse interstellar medium (ISM; e.g., see Kemper et al. 2004, Chiar & Tielens 2006, Henning 2010) often shifts to longer

wavelengths beyond $\sim 10\ \mu\text{m}$ in AGNs (e.g., see Sturm et al. 2005, Mason 2015). Also, this feature often shows a much broader width compared to that of the Milky Way diffuse ISM (see Li et al. 2008, Smith et al. 2010 and references therein).

The spectral profile of the $9.7\ \mu\text{m}$ silicate absorption feature seen in AGNs also exhibit spatial variations. Spatially-resolved observations of Circinus, a Seyfert 2 galaxy, made by Tristram et al. (2007) using the *Mid-Infrared Interferometric* (MIDI) instrument at the *Very Large Telescope* (VLT) reveals a two-component structure: an inner disk-like ($\sim 0.4\ \text{pc}$) component showing mild silicate emission around $\sim 10\ \mu\text{m}$, and an outer, extended, cooler torus ($\sim 2.0\ \text{pc}$) exhibiting silicate absorption. Both the emission and absorption features of Circinus resemble the spectral profile of the Milky Way diffuse ISM. On the other hand, the spatially-resolved mid-IR spectrum of NGC 1068, a prototypical type 2 AGN, shows that the silicate absorption profile varies with the distance to the nucleus, with the maximum absorption occurring around the innermost region (Rhee & Larkin 2006, Mason et al. 2006). Particularly, the *VLT*/MIDI observations of the central $\sim 2.0\ \text{pc}$ of NGC 1068 reveal that the silicate absorption profile also appears “anomalous”: differing from that of the Galactic ISM and that of common olivine-type silicate dust, the $9.7\ \mu\text{m}$ silicate absorption feature of NGC 1068 shows a relatively flat profile from ~ 8 to $9\ \mu\text{m}$ and then a sharp drop between ~ 9 and $10\ \mu\text{m}$, while the Galactic silicate absorption profiles already begin to drop at $\sim 8\ \mu\text{m}$ (see Figure 1 of Köhler & Li 2010).

Li et al. (2008) examined the anomalous redward-shifting of the peak wavelength and broadening of the width of the $9.7\ \mu\text{m}$ emission feature observed in the bright quasar 3C 273 and the low-luminosity AGN NGC 3998. They ascribed the anomalous silicate emission profile of 3C 273 and NGC 3998 to porous dust. Such an anomalous emission profile is also detected in the type 1 nucleus of M 81, a low-ionization nuclear emission-line region (LINER) and is explained in terms of μm -sized grains (Smith et al. 2010). In contrast, the anomalous spectral profile of the $9.7\ \mu\text{m}$ silicate feature observed in the innermost region of NGC 1068 was attributed to the presence of silicon carbide dust (Köhler & Li 2010) or to a less extent, gehlenite ($\text{Ca}_2\text{Al}_2\text{SiO}_7$), a high-temperature calcium aluminum silicate species. However, Nikutta et al. (2009) argued that, in the framework of a clumpy dust torus, the observed anomaly in the silicate emission and absorption profiles does not necessarily imply anomalies in dust size, structure or composition; instead, they argued that it could simply be caused by radiation transfer effects. But Xie et al. (2015, 2016) noted that the success of the “Clumpy” dust torus model (Nenkova et al. 2008a,b, Schartmann et al. 2008, Hönig & Kishimoto 2010) in explaining the much longer peak wavelength of the silicate Si–O emission feature (compared to that of the Galactic diffuse ISM) seems to be due to the adoption of a set of silicate opacity differing from that commonly adopted: Nikutta et al. (2009) adopted the silicate opacity of Ossenkopf et al. (1992) which peaks at $\sim 10.0\ \mu\text{m}$ while the

commonly-adopted opacity profile of “astronomical silicate” of Draine & Lee (1984) peaks at $\sim 9.5 \mu\text{m}$. Note that the observed silicate absorption profiles of the Galactic diffuse ISM peak at $\sim 9.7 \mu\text{m}$ (e.g., see Kemper et al. 2004, Chiar & Tielens 2006, Henning 2010).

The exact properties of the silicate dust component in AGN torus remain debated and no consensus has yet been reached. As elaborated above, the current knowledge about the silicate dust properties of AGNs are mainly derived from several individual sources. To address the observed silicate diversity among AGNs and to gain insight into the origin of the AGN dichotomy, it is necessary to study the silicate spectral profiles for a large and well defined AGN sample, taking into account a wide range of dust compositions and sizes. In this work we will model the *Spitzer*/IRS spectra of a large sample of 147 AGNs, including both type 1 and type 2 AGNs at both high and low luminosity levels. Such a large AGN sample will allow us to obtain a better understanding of the size and composition of the dust grains in AGN torus. For simplicity, we will focus on those AGNs showing silicate emission (see §2.1).

The structure of this paper is organized in the following sequence. We briefly describe the sample in §2 and elaborate the dust model in §3. We present in §4 the results derived from modeling the *Spitzer*/IRS spectra of 147 AGNs. Also in §4 we discuss the model-derived dust properties (e.g., composition, size, temperature) and their relations with the AGN parameters (e.g., accretion rate, luminosity, black hole mass). We summarize the major results of this paper in §5. Throughout the paper, we take the following cosmology parameters: $\Omega_m = 0.3$, $\Omega_\Lambda = 0.7$, and $H_0 = 70 h_{70} \text{ km s}^{-1} \text{ Mpc}^{-1}$.

2. Sample and Data

2.1. Samples

Our AGN sample is mainly collected from the literature. We consider all 87 PG quasars at $z \lesssim 0.5$ (Schmidt & Green 1983, Boroson & Green 1992) and all 52 *2MASS* quasars at $z \lesssim 0.3$ (Cutri et al. 2001, Smith et al. 2002). We also consider all 253 AGNs from the *Spitzer*/IRS-SDSS *Spectral Atlas of Galaxies and AGNs* (S³AGA; L. Hao et al. 2016, in preparation) at $z \lesssim 0.33$.

PG quasars are selected to have an average *B*-band absolute magnitude of ~ 16.16 , $U-B$ color of $\lesssim -0.44$, and a dominant point-like sources. All these objects show broad emission lines in optical, and thus are classified as type 1 quasars. Due to the large photographic magnitude errors and the simple color selection criterion, the PG sample is incomplete (e.g., see Goldschmidt et al. 1992, Jester et al. 2005), but the incompleteness is independent of

the optical magnitude and color (Jester et al. 2005). This indicates that the PG sample is still representative of bright optically selected quasars. In comparison with PG quasars, the *2MASS* quasars represent a redder population with $J - K_S \gtrsim 2$ (compared to a typical color of $J - K_S \gtrsim 1.5$ for PG quasars), but have a similar K_S -band luminosity of $K_S \lesssim 23$ (Smith et al. 2002). Unlike PG quasars, the *2MASS* sample includes objects with narrow, intermediate and broad emission lines. The *2MASS* sample is highly incomplete at $K_S \gtrsim 13$ (Cutri et al. 2001). Throughout the following text, we will refer to this sample as the quasar sample.

S³AGA is a heterogeneous collection of galaxies that have *Spitzer*/IRS low-resolution spectra (Houck et al. 2004) and *Sloan Digital Sky Survey* (SDSS) spectroscopic observations (Data Release 7; Abazajian et al. 2009) within a $\sim 3''$ searching radius. The whole S³AGA sample contains 139 type 1 AGNs, 114 type 2 AGNs, 241 star-forming (SF) galaxies, 103 AGN-SF composites, and one quiescent galaxy. The galaxy types are classified based on the *SDSS* optical emission line properties (see Hao et al. 2005b).¹ Throughout the following text, we will refer to this sample as S³AGA.

In this work we will disregard those sources which show silicate in absorption since they do not contain a sufficient amount of information for constraining the nature of the dust (particularly, the temperature of the dust). Also, the silicate absorption could have been contaminated by the interstellar silicate dust of the AGN’s host galaxy. Therefore, we are left with 147 sources (i.e., 85 PG quasars, 18 *2MASS* quasars, and 44 S³AGA AGNs). In Appendix we list the basic parameters including the redshift (z), type, black-hole mass (M_{BH}), and luminosity at $\lambda = 5100 \text{ \AA}$ for each of our 147 sources. Among these objects, the *Spitzer*/IRS spectra of 62 PG quasars, 13 *2MASS* quasars and 18 S³AGA AGNs show silicate in emission. We will focus on these 93 “silicate emission” sources which show silicate emission at 9.7 and 18 μm .

2.2. Data

For the selected sample sources, we utilize the low resolution mid-IR spectra obtained by *Spitzer*/IRS. The spectral wavelength ranges from $\sim 5 \mu\text{m}$ to $\sim 38 \mu\text{m}$ and the spectral resolution varies between ~ 60 and ~ 128 .

¹Type 1 AGNs are those exhibiting broad H α emission lines with an FWHM of $\gtrsim 1200 \text{ km s}^{-1}$. Type 2 AGNs are identified with the emission line ratios featuring the Baldwin, Phillips, & Terlevich (1989; BPT) diagram. This sample spans a redshift range of $z \sim 0.001\text{--}0.25$, corresponding to a physical size of $\sim 0.06\text{--}18 \text{ kpc}$ in the *SDSS* $3''$ aperture.

The *Spitzer*/IRS spectra for the quasar sample are compiled from Shi et al. (2014). The detailed observations and data reduction can be found in Shi et al. (2014) and reference therein. For the S³AGA sample, the mid-IR spectra are obtained from the *Cornell Atlas of Spitzer/IRS Sources* (CASSIS) which have been processed with Pipeline S18.7 (Lebouteiller et al. 2011). For more details we refer to L. Hao et al. (2016, in preparation).

We have not specifically applied any quantitative signal-to-noise (SNR) cut to the selected spectra; instead, the selection is mainly based on visual inspection and we require an apparent detection of the 9.7 and 18 μm silicate emission features or a flat, featureless emission continuum.² As demonstrated in §4.6, the “silicate emission” sources and the “flat continuum” sources appreciably distinguish themselves from each other in terms of the flux fraction of the silicate emission features in the total mid-IR emission. Finally, we note that for those sources whose *Spitzer*/IRS spectra are of a rather low SNR, we will exclude them when we statistically examine whether (and how) the dust properties are related to the AGN properties.

3. The Dust Model

We aim to constrain the dust chemical composition, size, and temperature through modeling the observed dust thermal IR emission. We will consider two kinds of dust: amorphous silicate and carbonaceous dust. For the former, we will consider a range of compositions: (1) the Draine & Lee (1984) “astronomical silicate”, (2) three pyroxene species ($\text{Mg}_x\text{Fe}_{1-x}\text{SiO}_3$ with $x = 0.4, 0.7, 1.0$), and (3) two olivine species ($\text{Mg}_{2x}\text{Fe}_{2(1-x)}\text{SiO}_4$ with $x = 0.4, 0.5$). For the latter, we will consider graphite and amorphous carbon. Although other dust species (e.g., SiC, oxides) may also be present in AGN torus (e.g., see Laor & Draine 1993, Markwick-Kemper et al. 2007, Köher & Li 2010), in this work they are not included in our model. The dust is expected to have a distribution of sizes. For simplicity, we will only consider 100 discrete sizes: $a = 0.1, 0.2, \dots, 10.0 \mu\text{m}$ at a step of $0.1 \mu\text{m}$ where a is the spherical radius of the dust (we assume a spherical shape for the dust). The dust is also expected to have a distribution of temperatures, with the dust temperature reaching $\gtrsim 1500 \text{ K}$ — the sublimation temperature of silicate, graphite and amorphous carbon and dropping to $\lesssim 100 \text{ K}$ in the outer boundary of the torus. Also for simplicity, we will only consider two temperatures — a warm component of temperature T_w and a cold component of temperature T_c — to represent the temperature distribution.

²For some sources, the flat emission continuum may be superimposed by several spectral features from polycyclic aromatic hydrocarbon (PAH) molecules (see §4.6).

Assuming that the torus is optically thin in the IR, we model the dust IR emission as

$$F_\nu = \frac{1}{d^2} \times \sum_i \{B_\nu(T_{w,i}) \times \kappa_{\text{abs},i}(\nu) \times M_{w,i} + B_\nu(T_{c,i}) \times \kappa_{\text{abs},i}(\nu) \times M_{c,i}\} \quad , \quad (1)$$

where the sum is over the two dust species (silicate and graphite or amorphous carbon), d is the luminosity distance of the object, $\kappa_{\text{abs},i}(\nu)$ is the mass absorption coefficient (in unit of $\text{cm}^2 \text{g}^{-1}$) of dust of type i , $B_\nu(T)$ is the Planck function of temperature T at frequency ν , $T_{w,i}$ and $T_{c,i}$ are respectively the temperatures of the warm and cold components of dust of type i , and $M_{w,i}$ and $M_{c,i}$ are respectively the masses of the warm and cold components of dust of type i . For a given composition and size, the mass absorption coefficient $\kappa_{\text{abs}}(\nu)$ is obtained from Mie theory (Bohren & Huffman 1983) using the refractive indices (1) of Draine & Lee (1984) for “astronomical silicate” and graphite, (2) of Dorschner et al. (1995) for amorphous pyroxene and amorphous olivine, and (3) of Rouleau & Martin (1991) for amorphous carbon. We refer the reader to Figure 2 of Xie et al. (2015) for the computed $\kappa_{\text{abs}}(\nu)$ profiles for different grain materials and sizes.

4. Results and Discussion

In fitting the observed IR emission, we have eight parameters: the temperature (T_w^S) and mass (M_w^S) for the warm silicate component, the temperature (T_c^S) and mass (M_c^S) for the cold silicate component, the temperature (T_w^G) and mass (M_w^G) for the warm carbon dust component, and the temperature (T_c^G) and mass (M_c^G) for the cold carbon dust component. We require the dust temperatures not to exceed the sublimation temperature ($T_{\text{subl}} \sim 1500 \text{ K}$) of silicate and graphite materials. By applying cosmic abundance constraints to $M_{\text{carb}}/M_{\text{sil}}$, the mass ratio of the silicate component to the carbon dust component, we require $0.2 < M_{\text{carb}}/M_{\text{sil}} < 2$ (see Xie et al. 2015). With these constraints taken into account, we obtain the best fit for each galaxy using the MPFIT code, an IDL χ^2 -minimization routine based on the Levenberg-Marquardt algorithm (Markwardt 2009). The quality of the fit is measured by the reduced χ^2 which is defined as follows:

$$\chi^2/\text{dof} = \sum_{j=1}^{N_{\text{obs}}} \left\{ \frac{F_\nu(\text{mod}) - F_\nu(\text{obs})}{\sigma_\nu(\text{obs})} \right\}^2 / \{N_{\text{obs}} - N_{\text{mod}}\} \quad , \quad (2)$$

where $F_\nu(\text{mod})$ is the model-calculated flux density, $F_\nu(\text{obs})$ is the observed flux density, $\sigma_\nu(\text{obs})$ is the observational uncertainty of the flux density $F_\nu(\text{obs})$, N_{obs} is the number of data points, and $N_{\text{mod}} = 8$ is the number of model parameters.

We note that the *Spitzer*/IRS spectra in the $\sim 5\text{--}14.5 \mu\text{m}$ wavelength interval have a lower SNR compared with that in the interval of $\sim 14.5\text{--}38 \mu\text{m}$. This is due to the different

observational modules, i.e., the $\sim 5\text{--}14.5\ \mu\text{m}$ *Short Low* (SL) IRS module has a slit width of $\sim 3.6''$, while the $\sim 14.5\text{--}38\ \mu\text{m}$ *Long Low* (LL) IRS module has a slit width of $\sim 11.2''$. To fit the $\sim 5\text{--}8\ \mu\text{m}$ continuum emission and the $9.7\ \mu\text{m}$ silicate emission feature, for those sources of which the SL spectra are rather noisy (including PG1352+183, 2MASSJ132917.5+121340, 2MASSJ234259.3+134750, 2MASXJ02335161+0108136, 2MASXJ13495283+0204456, and SDSSJ115138.24+004946.4), we arbitrarily increase the weights respectively by a factor of ten and two for the data points at $\sim 5\text{--}8\ \mu\text{m}$ and $\sim 8\text{--}14.5\ \mu\text{m}$ (relative to that at $\sim 14.5\text{--}38\ \mu\text{m}$). These sources will be excluded when we perform statistical analyses of the possible correlations between the dust properties and the AGN properties.

In Figure 1, we show the best-fit results to all 93 “silicate emission” sources which exhibit prominent silicate emission at 9.7 and $18\ \mu\text{m}$. The best-fit model parameters and their uncertainties are tabulated in Table 1. The uncertainties for the model parameters are derived by performing Monte-Carlo simulations. As illustrated in Figure 2 with PG 2233+134 as an example, we assume that the *Spitzer*/IRS flux density uncertainty statistically follows a normal distribution. The dispersion is taken to be the observed 1σ error, composed of the statistical and systematic errors, with the latter arising from the flux differences between the two nodes of the *Spitzer*/IRS spectra, the sky background contamination, and the *Spitzer*/IRS pointing and flux calibration errors (Lebouteiller et al. 2011). A new “observational” spectrum is generated through randomly sampling a point at each wavelength from the normal distribution. We then model the new spectrum and derive a set of model parameters. We conduct 100 simulations for each source as the parameters derived from 10,000 simulations only slightly differ from that derived from 100 simulations (Xie et al. 2015). The final model spectrum is calculated from the median values of the model parameters. The error of each parameter is derived from the standard deviation of 100 simulations.

4.1. Dust Composition

We find that the combination of the Draine & Lee (1984) “astronomical silicate” and graphite can closely reproduce the *Spitzer*/IRS spectra of 60 of our 93 AGNs. For 31 AGNs, amorphous olivine combined with graphite fits the observed spectra better than “astronomical silicate”. In contrast, amorphous pyroxene provides the best fit to two of our 93 AGNs (i.e, PG 1535+547 and PG 2214+139). For illustration, in Figure 3 we show the best-fit results for three PG quasars (PG 1004+130, PG 1351+640, and PG 2214+139) for which the best-fits are respectively provided by “astronomical silicate”, amorphous olivine $\text{Mg}_{1.2}\text{Fe}_{0.8}\text{SiO}_4$, and amorphous pyroxene $\text{Mg}_{0.3}\text{Fe}_{0.7}\text{SiO}_3$, again, together with graphite. Different silicate species have different band widths, peak wavelengths, and relative strengths

for the 9.7 and 18 μm features. For a given grain size, the Draine & Lee (1984) “astronomical silicate” results in an absorption profile at 9.7 μm much broader than amorphous olivine and pyroxene, while amorphous olivine gives the longest peak wavelength for the 9.7 μm feature and the highest ratio of the 18 μm feature to the 9.7 μm feature, and amorphous pyroxene has the smallest ratio of the 9.7 μm feature to the “trough” between the 9.7 and 18 μm features. As elaborated in Figure 3, the *Spitzer*/IRS spectra of PG 1004+130, PG 1351+640, and PG 2214+139 show considerable variations in the spectral profiles of the 9.7 and 18 μm emission features. For illustration, we display in Figure 4 the *Spitzer*/IRS spectra of several selected AGNs for which the best fits favor “astronomical silicate”, amorphous olivine, and amorphous pyroxene, respectively. Although complicated by the dust size and temperature effects, a first glance of Figure 4 would already tell that these AGNs differ in silicate composition and their spectral profiles appear consistent with the feature width and band ratio expected from “astronomical silicate”, amorphous olivine, or amorphous pyroxene, respectively.

There are also several AGNs for which their silicate emission features can not be closely fitted in terms of “astronomical silicate”, amorphous olivine, or amorphous pyroxene. We note that, except a couple of sources of which the *Spitzer*/IRS spectra are noisy (e.g., PG 1352+183), most of these AGNs probably have other dust species (e.g., crystalline silicates) present. In Figure 5 we display the *Spitzer*/IRS spectra of those sources which exhibit the crystalline silicate emission features at 11.3, 16.3, 18.5, 23.5, and 27.5 μm .

Finally, we note that our model fitting is not sensitive to the choice of graphite or amorphous carbon. However, the opacity profile of amorphous carbon exhibits several weak resonant structures in the wavelength range of $\sim 5\text{--}8\ \mu\text{m}$ (see Figure 3b of Xie et al. 2015) which are not seen in the *Spitzer*/IRS spectra of the AGNs considered here. Therefore, graphite appears more favorable.

4.2. Dust Sizes

From our fitting, we find that the *Spitzer*/IRS spectra of 70 of our 93 AGNs can be well reproduced with spherical grains of radii $a = 1.5\ \mu\text{m}$. Only three AGNs require grains smaller than $a = 1\ \mu\text{m}$. In Figure 6 we show the histogram of the best-fit grain sizes. Roughly speaking, the sizes of the grains in the torus around these 93 AGNs which show silicate emission are constrained to be $\sim 1.5 \pm 0.1\ \mu\text{m}$. This is consistent with our previous work that the dust grains in AGNs are micrometer-sized (e.g., Li et al. 2008, Smith et al. 2010, Xie et al. 2015).

We calculate the extinction as a function of inverse wavelength (λ^{-1}) expected from

mixtures of spherical amorphous silicate and graphite of radii $a = 1.5 \mu\text{m}$. We represent the extinction by $E(\lambda - V)/E(B - V)$, where $E(\lambda - V) \equiv A_\lambda - A_V$, $E(B - V) \equiv A_B - A_V$, and A_λ , A_B , and A_V are respectively the extinction at wavelength λ , and at the B and V bands. As shown in Figure 7, the extinction curve predicted from a mixture of silicate and graphite grains of $a = 1.5 \mu\text{m}$ is flat or gray at $\lambda^{-1} > 2.5 \mu\text{m}^{-1}$, i.e., the extinction varies little with λ^{-1} . Depending on the mass ratio of graphite to silicate, the extinction displays a gradual rise at $\lambda^{-1} > 4.5 \mu\text{m}$ and then flattens off at $\lambda^{-1} > 6 \mu\text{m}$. But overall, the extinction curve is flat. The resonant structures seen at $\lambda^{-1} < 2.5 \mu\text{m}^{-1}$ will be smoothed out if we consider a distribution of grain sizes instead of single sizes of $a = 1.5 \mu\text{m}$.

The predicted gray extinction curve generally agrees with that of Gaskell et al. (2004) who derived an AGN extinction curve based on the composite spectra of 72 radio quasars and 1018 radio-quiet AGNs. Czerny et al. (2004) also constructed a relatively featureless flat extinction curve for quasars based on the blue and red composite quasar spectra of Richards et al. (2003) obtained from the Sloan Digital Sky Survey (SDSS). It is interesting to note that, the extinction curve calculated from spherical silicate dust of $a = 1.5 \mu\text{m}$ closely agrees with that of Gaskell et al. (2004) except those resonant structures at $\lambda^{-1} < 2.5 \mu\text{m}^{-1}$ which are expected to be smoothed out if a distribution of grain sizes is considered. The Galactic extinction curve differs substantially from our model extinction curve as well as that of Gaskell et al. (2004) in that, the Galactic extinction curve shows a prominent extinction bump at 2175 \AA and a steep far-UV rise which is believed to arise from small graphite dust grains. In contrast, the extinction curve of the Small Magellanic Cloud (SMC) lacks the 2175 \AA bump and displays an even steeper far-UV rise than that of the Milky Way.

4.3. Dust Temperatures

Figure 8 presents the histograms of the dust temperatures derived from our best-fits to the *Spitzer*/IRS spectra of these 93 “silicate emission” sources (which show silicate emission). It is seen that the temperatures for the warm silicate dust component (T_w^S) span from $\sim 150 \text{ K}$ to $\sim 500 \text{ K}$, with a median value of $\sim 265 \text{ K}$ and a dispersion of $\sim 89 \text{ K}$. The temperatures for the cold silicate component (T_c^S) vary from $\sim 40 \text{ K}$ to $\sim 200 \text{ K}$. The median value is $\sim 66 \text{ K}$ for T_c^S and the dispersion is $\sim 89 \text{ K}$. For graphite, much higher temperatures are obtained: T_w^G is in the range of $\sim 200 \text{ K}$ to $\sim 1000 \text{ K}$, with a median value of $\sim 638 \text{ K}$ and a dispersion of $\sim 159 \text{ K}$; T_c^G is within $\sim 100 \text{ K}$ to $\sim 220 \text{ K}$, with a median value of $\sim 159 \text{ K}$ and a dispersion of $\sim 22 \text{ K}$. We note that, even if the spatial distributions of silicate and graphite are similar in an AGN torus, one expects graphite to be much hotter than silicate because of the much higher UV/optical absorptivities of graphite compared to that of silicate (see Draine & Lee

1984). Graphite grains could be distributed closer to the central engine of an AGN than silicate grains since graphite has a higher sublimation temperature (see Li 2009).

The grains in the AGN torus are heated by photons from the central engine. Let R be the distance of a silicate or graphite grain of size a from the central engine of luminosity L_λ . The steady-state temperature of the grain can be calculated from the energy balance between absorption and emission:

$$\int_0^\infty \frac{L_\lambda}{4\pi R^2} C_{\text{abs}}(a, \lambda) d\lambda = \int_0^\infty 4\pi B_\lambda[T(a, R)] C_{\text{abs}}(a, \lambda) d\lambda \quad , \quad (3)$$

where $C_{\text{abs}}(a, \lambda)$ is the absorption cross section of the spherical grain of radii a at wavelength λ , and $B_\lambda(T)$ is the Planck function of temperature T . For simplicity, in eq. 3 we neglect the extinction of the illuminating light in the torus. If the dust extinction is included, one would expect a smaller R for the same dust temperature. For the AGN luminosity L_λ , we take the tabulated $L_\lambda(5100 \text{ \AA})$ (see Table 4) and the spectral shape of Rowan-Robinson (1995). For each AGN and each dust component, we derive the distance of the dust from the central engine where the dust attains an equilibrium temperature exactly equaling that derived from the *Spitzer*/IRS spectral modeling. We find that the warm dust components are at several hundredth to tenth parsecs from the central engine and the cold dust components are at several parsecs from the central engine (see Figure 9). The actual distances could be smaller since the torus extinction is neglected in calculating the dust temperature. These results are consistent with Elitzur (2006) who argues for a torus size of no more than a few parsecs.

4.4. Dust Masses

We show in Figure 10 the mass ratios of the warm graphite component to the warm silicate component (M_w^G/M_w^S), and the mass ratios of the cold graphite component to the cold silicate component (M_c^G/M_c^S). We derive a mean ratio of ~ 0.33 for M_w^G/M_w^S , and a mean ratio of ~ 0.93 for M_c^G/M_c^S . However, these ratios should be treated with caution since for a substantial number of sources the mass ratio reaches the pre-set limiting values of $M_{\text{carb}}/M_{\text{sil}} = 0.2$ and $M_{\text{carb}}/M_{\text{sil}} = 2.0$ (see Figure 10). We find that reasonably good fits are still achievable as long as $M_{\text{carb}}/M_{\text{sil}} \gtrsim 0.05$.

For our “silicate emission” sources, the stellar mass (M_\star) is known for 39 PG quasars and two *2MASS* quasars (see Zhang et al. 2016). For each of these sources, we obtain M_{dust} , the total dust mass summed over all four dust components (i.e., $M_{\text{dust}} = M_w^S + M_c^S + M_w^G + M_c^G$). In Figure 11 we compare the dust mass with the stellar mass. On average, the dust-to-stellar mass ratio of these sources is $\sim 10^{-7}$, much smaller than that of the Milky Way ($\sim 10^{-3}$;

see Li 2004). This ratio appears reasonable since the mid-IR emission considered here only probes the dust in the torus while the bulk mass is in starlight-heated cold dust in the host galaxy which emits in the far-IR and escapes from detection by *Spitzer*/IRS.

4.5. Correlations between Dust and AGNs

With the dust properties determined, we now explore the possible connection between the fundamental properties of AGNs and the properties of the dust derived from the silicate emission modeling. If the dust in the torus is heated by the photons originating from the accretion disk, one would expect the dust properties to somewhat correlate with the AGN parameters. Therefore, we examine the correlation between the dust temperature and mass and the bolometric luminosity (L_{bol}), black hole mass (M_{BH}), and Eddington ratio ($L_{\text{bol}}/L_{\text{Edd}}$) of AGNs. We represent L_{bol} by $\lambda L_{\lambda}(5100 \text{ \AA})$, since the spectral region at this wavelength is barely contaminated by emission lines and is assumed to be purely from the AGN accretion disk. The Eddington ratio (ε) relates the AGN bolometric luminosity with the Eddington luminosity: $\varepsilon \equiv L_{\text{bol}}/L_{\text{Edd}}$, with $L_{\text{Edd}} = 4\pi cGMm_{\text{H}}/\sigma_T$, where c is the speed of light, G is the gravitational constant, and σ_T is the Thomson cross section. We compile these parameters from the literature and list them in Table 4.

In Figures 12, 13, 14 we present the correlations between the dust masses of the warm silicate, warm graphite, cold silicate and cold graphite components with the bolometric luminosity, the black hole mass, and the Eddington ratio of AGNs. While the dust masses show no correlation with the black hole mass or with the Eddington ratio, they do show a somewhat correlation with the bolometric luminosity (see Figure 12a,b,d). This suggests that the covering factor of the dust torus (i.e., the fraction of the sky covered by the torus as seen from the central engine) may increase with the bolometric luminosity of AGNs. Similarly, in Figures 15, 16, 17 we present the correlations between the temperatures (T) of the warm silicate, warm graphite, cold silicate and cold graphite components with the bolometric luminosity, the black hole mass, and the Eddington ratio of AGNs. No correlations are found. The lack of correlation between T and L_{bol} is not unexpected since T depends on both L_{bol} and R , the distance of the dust from the central engine.

4.6. Other Sources

Among our sample of 147 AGNs, there are 30 sources which do not show prominent silicate emission but a featureless thermal continuum in the mid-IR (hereafter we will call

these AGNs “flat continuum” sources). In addition, there are 24 sources exhibit weak PAH features superimposed on an otherwise featureless thermal continuum (hereafter we will call these AGNs “PAH + continuum” sources). In Figure 18 we show $F_{\text{silicate}}/F_{\text{MIR}}$, the fractional fluxes emitted in the 9.7 and 18 μm silicate features relative to the total mid-IR emission at $\sim 5\text{--}38\ \mu\text{m}$, for all three categories of sources.³ It is apparent that, with a considerably larger mean fractional flux ($\langle F_{\text{silicate}}/F_{\text{MIR}} \rangle \approx 0.13$), the “silicate emission” sources clearly distinguish them from those “flat continuum” sources (with $\langle F_{\text{silicate}}/F_{\text{MIR}} \rangle \approx 0.041$) and “PAH + continuum” sources (with $\langle F_{\text{silicate}}/F_{\text{MIR}} \rangle \approx 0.051$). This confirms that the silicate emission features in the 93 “silicate emission” sources are indeed prominent and therefore the silicate dust properties yielded from our modeling have a high level of significance.

We have also modeled the *Spitzer*/IRS spectra of those 30 “flat continuum” sources which do not show any silicate emission but a featureless thermal continuum. As shown in Figure 19, mixtures of μm -sized silicate and graphite also provide close fits to the observed spectra. Compared with those “silicate emission” sources (which show prominent silicate emission features; see Figure 1), these sources have lower dust temperatures (see Figure 20). In Figure 21 we show the graphite-to-silicate mass ratios.

We have also modeled the thermal continuum emission of these 24 “PAH + continuum” sources with mixtures of silicate and graphite grains. As shown in Figure 22, the best-fits to the observed spectra are provided by μm -sized dust grains. The graphite-to-silicate mass ratios are shown in Figure 24. The derived dust temperatures are shown in Figure 23 and they are rather close to that of those PAH-lacking “flat continuum” sources. This suggests that the thermal continuum emission seen in these “PAH + continuum” AGNs is not from their host galaxies but from the torus.

A wide variety of Galactic and extragalactic objects show a distinctive set of emission features at 3.3, 6.2, 7.7, 8.6, and 11.3 μm . These features are generally identified as the vibrational modes of PAH molecules (Léger & Puget 1984, Allamandola, Tielens, & Barker 1985). However, the PAH features are often absent in AGNs (e.g., see Roche et al. 1991). This is generally interpreted as the destruction of PAHs by extreme UV and soft X-ray photons in AGNs (Roche et al. 1991, Voit 1992, Siebenmorgen, Krügel, & Spoon 2004). If the PAH emission and the thermal emission continuum seen in these sources are contaminated by their host galaxies, one would expect the dust to be smaller and colder than that in those “flat continuum” sources of which the *Spitzer*/IRS spectra are characterized by a featureless, PAH-lacking thermal continuum. This is because the interstellar dust grains in the host galaxies of AGNs are believed to be around $\sim 0.1\ \mu\text{m}$ in size and $\sim 20\ \text{K}$ in temperature (see

³For the “flat continuum” sources and the “PAH + continuum” sources, F_{silicate} is actually an upper limit.

Li & Draine 2001). But as we see that this is not the case. The PAH emission features may as well arise from the AGN torus, i.e., some quantities of PAHs may survive in the hostile environments of AGNs (L.C. Ho, private communication).

5. Summary

We have investigated the dust properties of a sample of 147 AGNs compiled from PG quasars, *2MASS* quasars, and S³AGA AGNs which do not show silicate absorption features. Our principal results are as follows:

1. Through fitting the *Spitzer*/IRS spectra of 93 AGNs of various types in which the 9.7 and 18 μm emission features are seen in emission with mixtures of silicate and graphite grains, we find that the majority (60/93) of the observed spectra can be well reproduced by “astronomical silicate”, with the remaining 31 sources favoring amorphous olivine and two sources favoring amorphous pyroxene.
2. All sources require the dust to be μm -sized (with a typical size of $\sim 1.5 \mu\text{m}$), much larger than the sub- μm -sized Galactic interstellar dust. This implies a flat or “gray” extinction curve for AGNs.
3. The 9.7 μm emission feature arises predominantly from warm silicate dust of temperature $T \sim 270 \text{ K}$, while the $\sim 5\text{--}8 \mu\text{m}$ continuum emission is mostly from graphite of $T \sim 640 \text{ K}$.
4. We have examined the possible relations between the dust masses and temperatures and the bolometric luminosity, black hole masses, and Eddington ratios of AGNs. It is found that except the dust masses are somewhat correlated with the bolometric luminosity, we do not see any correlations between any other quantities.
5. We have also modeled the *Spitzer*/IRS spectra of 30 (of 147) sources which do not show silicate emission features but a featureless thermal continuum. Compared to those 93 sources which show silicate emission, μm -sized silicate and graphite grains with smaller silicate-to-graphite mass ratios and lower dust temperatures are preferred. We have also modeled the *Spitzer*/IRS spectra of 24 (of 147) sources which exhibit weak PAH emission features superimposed on an otherwise featureless thermal continuum. It is found that the derived dust sizes and temperatures are not appreciably different from that of those 30 sources which emit a featureless thermal continuum.

We thank B.T. Draine, L.C. Ho and the anonymous referee for stimulating discussions and suggestions. We thank Y. Shi for kindly providing us with the *Spitzer*/IRS spectra of PG quasars. A.L. and X.Y.X. are supported in part by NSF AST-1311804 and NASA NNX14AF68G. L.H. is supported by NSFC 11473305 and the CAS Strategic Priority Research Program XDB09030200. The Cornell Atlas of *Spitzer*/IRS Sources (CASSIS) is a product of the Infrared Science Center at Cornell University, supported by NASA and JPL.

A. Basic Parameters for Our Sample of 147 AGNs

In this appendix we list the redshift (z), type, black-hole mass (M_{BH}), and luminosity at $\lambda = 5100 \text{ \AA}$ for each of our 147 AGNs, which are divided into three categories: the “silicate emission” sources which exhibit the 9.7 and $18 \mu\text{m}$ silicate emission features (see Table 4), the “flat continuum” sources which exhibit a featureless emission continuum (see Table 5), and the “PAH + continuum” sources which show PAH emission features superimposed on an otherwise featureless continuum (see Table 6).

REFERENCES

- Abazajian, K. N., Adelman-McCarthy, J. K., Agüeros, M. A., et al. 2009, *ApJS*, 182, 543
- Allamandola, L. J., Tielens, A. G. G. M., & Barker, J. R. 1985, *ApJ*, 290, L25
- Antonucci, R. 1993, *ARA&A*, 31, 473
- Antonucci, R. R. J., & Miller, J. S. 1985, *ApJ*, 297, 621
- Bohren, C. F. & Huffman, D. R. 1983, *Absorption and scattering of light by small particles*, Wiley
- Boroson, T. A., & Green, R. F. 1992, *ApJS*, 80, 109
- Chiar, J. E., & Tielens, A. G. G. M. 2006, *ApJ*, 637, 774
- Cutri, R. M., Nelson, B.O., Kirkpatrick, J.D., Huchra, J.P. & Smith, P.S. 2001, in *ASP Conf. Ser. 232: The New Era of Wide Field Astronomy*, ed. R. Clowes, A. Adamson, & G. Bromage (San Francisco, CA: ASP), 78
- Czerny, B., Li, J., Loska, Z., & Szczerba, R. 2004, *MNRAS*, 348, 54
- Dasyra, K. M., Ho, L. C., Netzer, H., et al. 2011, *ApJ*, 740, 94

- Draine, B. T., & Lee, H. M. 1984, *ApJ*, 285, 89
- Dong, X.-B., Ho, L. C., Wang, J.-G., et al. 2010, *ApJ*, 721, L143
- Dorschner, J., Begemann, B., Henning, T., Jaeger, C., & Mutschke, H. 1995, *A&A*, 300, 503
- Du, P., Hu, C., Lu, K.-X., et al. 2014, *ApJ*, 782, 45
- Elitzur, M. 2006, *New Astro. Rev.*, 50, 728
- Elitzur, M., & Shlosman, I. 2006, *ApJ*, 648, L101
- Gaskell, C. M., Goosmann, R. W., Antonucci, R. R. J., & Whysong, D. H. 2004, *ApJ*, 616, 147
- Greene, J. E., Ho, L. C., & Barth, A. J. 2008, *ApJ*, 688, 159
- Goldschmidt, P., Miller, L., La Franca, F., & Cristiani, S. 1992, *MNRAS*, 256, 65P
- Hao, L., Spoon, H. W. W., Sloan, G. C., et al. 2005a, *ApJ*, 625, L75
- Hao, L., Strauss, M. A., Tremonti, C. A., et al. 2005b, *AJ*, 129, 1783
- Hao, L., Weedman, D. W., Spoon, H. W. W., et al. 2007, *ApJ*, 655, L77
- Henning, T. 2010, *ARA&A*, 48, 21
- Ho, L. C., & Kim, M. 2014, *ApJ*, 789, 17
- Hönig, S. F., & Kishimoto, M. 2010, *A&A*, 523, A27
- Houck, J. R., Roellig, T. L., van Cleve, J., et al. 2004, *ApJS*, 154, 18
- Jaffe, W., Meisenheimer, K., Röttgering, H. J. A., et al. 2004, *Nature*, 429, 47
- Jester, S., Schneider, D. P., Richards, G. T., et al. 2005, *AJ*, 130, 873
- Kaspi, S., Smith, P. S., Netzer, H., et al. 2000, *ApJ*, 533, 631
- Kemper, F., Vriend, W. J., & Tielens, A. G. G. M. 2004, *ApJ*, 609, 826
- Markwick-Kemper, F., Gallagher, S. C., Hines, D. C., & Bouwman, J. 2007, *ApJ*, 668, L107
- Köhler, M., & Li, A. 2010, *MNRAS*, 406, L6
- Laor, A., & Draine, B. T. 1993, *ApJ*, 402, 441

- Lebouteiller, V., Barry, D. J., Spoon, H. W. W., et al. 2011, *ApJS*, 196, 8
- Leger, A., & Puget, J. L. 1984, *A&A*, 137, L5
- Li, A. 2004, in *Penetrating Bars Through Masks of Cosmic Dust: The Hubble Tuning Fork Strikes a New Note*, ed. D.L. Block, I. Puerari, K.C. Freeman, R. Groess, & E.K. Block (Dordrecht: Kluwer) 535
- Li, A. 2007, in *The Central Engine of Active Galactic Nuclei (ASP Conf. Ser. 373)*, ed. L. C. Ho & J.-M. Wang (San Francisco, CA: ASP), 561
- Li, A. 2009, in *Small Bodies in Planetary Sciences (Lecture Notes in Physics vol. 758)*, ed. I. Mann, A. Nakamura, & T. Mukai, Springer, Chapter 6, 167
- Li, A., & Draine, B. T. 2001, *ApJ*, 554, 778
- Li, M. P., Shi, Q. J., & Li, A. 2008, *MNRAS*, 391, L49
- Lumsden, S. L., Alexander, D. M., & Hough, J. H. 2004, *MNRAS*, 348, 1451
- Maiolino, R., Marconi, A., & Oliva, E. 2001, *A&A*, 365, 37
- Mason, R. E. 2015, *Planet. Space Sci.*, 116, 97
- Mason, R. E., Wright, G., Pendleton, Y., & Adamson, A. 2004, *ApJ*, 613, 770
- Mason, R. E., Geballe, T. R., Packham, C., et al. 2006, *ApJ*, 640, 612
- Mason, R. E., Levenson, N. A., Shi, Y., et al. 2009, *ApJ*, 693, L136
- Mishra, A., & Li, A. 2015, *ApJ*, 809, 120
- Markwardt, C. B. 2009, *Astronomical Data Analysis Software and Systems XVIII*, 411, 251
- Marziani, P., Sulentic, J. W., Zamanov, R., et al. 2003, *ApJS*, 145, 199
- Nenkova, M., Sirocky, M. M., Ivezić, Ž., & Elitzur, M. 2008, *ApJ*, 685, 147
- Nenkova, M., Sirocky, M. M., Nikutta, R., Ivezić, Ž., & Elitzur, M. 2008, *ApJ*, 685, 160
- Neugebauer, G., Green, R. F., Matthews, K., et al. 1987, *ApJS*, 63, 615
- Nikutta, R., Elitzur, M., & Lacy, M. 2009, *ApJ*, 707, 1550
- Ossenkopf, V., Henning, T., & Mathis, J. S. 1992, *A&A*, 261, 567

- Rhee, J. H., & Larkin, J. E. 2006, *ApJ*, 640, 625
- Richards, G. T., Hall, P. B., Vanden Berk, D. E., et al. 2003, *AJ*, 126, 1131
- Rieke, G. H., & Low, F. J. 1975, *ApJ*, 199, L13
- Roche, P. F., Aitken, D. K., Smith, C. H., & Ward, M. J. 1991, *MNRAS*, 248, 606
- Roche, P. F., Packham, C., Aitken, D. K., & Mason, R. E. 2007, *MNRAS*, 375, 99
- Rose, M., Tadhunter, C. N., Holt, J., & Rodríguez Zaurín, J. 2013, *MNRAS*, 432, 2150
- Rouleau, F., & Martin, P. G. 1991, *ApJ*, 377, 526
- Rowan-Robinson, M. 1995, *MNRAS*, 272, 737
- Sani, E., Lutz, D., Risaliti, G., et al. 2010, *MNRAS*, 403, 1246
- Schartmann, M., Meisenheimer, K., Camenzind, M., et al. 2008, *A&A*, 482, 67
- Schmidt, M., & Green, R. F. 1983, *ApJ*, 269, 352
- Siebenmorgen, R., Krügel, E., & Spoon, H. W. W. 2004, *A&A*, 414, 123
- Siebenmorgen, R., Haas, M., Krügel, E., & Schulz, B. 2005, *A&A*, 436, L5
- Shen, Y., Richards, G. T., Strauss, M. A., et al. 2011, *ApJS*, 194, 45
- Shi, Y., Rieke, G. H., Ogle, P. M., Su, K. Y. L., & Balog, Z. 2014, *ApJS*, 214, 23
- Smith, P. S., Schmidt, G. D., Hines, D. C., Cutri, R. M., & Nelson, B. O. 2002, *ApJ*, 569, 23
- Smith, H. A., Li, A., Li, M. P., et al. 2010, *ApJ*, 716, 490
- Sturm, E., Schweitzer, M., Lutz, D., et al. 2005, *ApJ*, 629, L21
- Sturm, E., Rupke, D., Contursi, A., et al. 2006, *ApJ*, 653, L13
- Trichas, M., Green, P. J., Constantin, A., et al. 2013, *ApJ*, 778, 188
- Tristram, K. R. W., Meisenheimer, K., Jaffe, W., et al. 2007, *A&A*, 474, 837
- Urry, C. M., & Padovani, P. 1995, *PASP*, 107, 803
- Vestergaard, M., & Peterson, B. M. 2006, *ApJ*, 641, 689

- Voit, G. M. 1991, *ApJ*, 379, 122
- Voit, G. M. 1992, *MNRAS*, 258, 841
- Wandel, A., Peterson, B. M., & Malkan, M. A. 1999, *ApJ*, 526, 579
- Wang, J.-M., & Zhang, E.-P. 2007, *ApJ*, 660, 1072
- Woo, J.-H., Kim, J. H., Imanishi, M., & Park, D. 2012, *AJ*, 143, 49
- Wu, X.-B., & Liu, F. K. 2004, *ApJ*, 614, 91
- Xie, Y., Hao, L., & Li, A. 2014, *ApJ*, 794, L19
- Xie, Y., Li, A., Hao, L., & Nikutta, R. 2015, *ApJ*, 808, 145
- Xie, Y., Nikutta, R., Hao, L., & Li, A. 2016, *Planet. Space Sci.*, 133, 23 (arXiv:1605.06999)
- Zhu, L., Zhang, S. N., & Tang, S. 2009, *ApJ*, 700, 1173
- Zhang, Z., Shi, Y., Rieke, G. H., et al. 2016, *ApJ*, 819, L27

Table 1. Model Parameters for 93 AGNs Showing Silicate Emission around 9.7 and 18 μm

Source (1)	T_w^S (K) (2)	M_w^S (M_\odot) (3)	T_c^S (K) (4)	M_c^S (M_\odot) (5)	T_w^G (K) (6)	M_w^G (M_\odot) (7)	T_c^G (K) (8)	M_c^G (M_\odot) (9)
PG0003+158	358.00 \pm 73.60	4.32E1 \pm 2.00E1	174.33 \pm 7.98	2.53E3 \pm 1.64E2	790.57 \pm 59.82	8.64 \pm 4.00	182.83 \pm 3.77	5.06E3 \pm 3.28E2
PG0003+199	317.95 \pm 1.06	2.77 \pm 5.71E-2	40.00 \pm 3.10	1.42E3 \pm 2.51E1	744.55 \pm 4.43	5.54E-1 \pm 1.14E-2	187.60 \pm 0.66	2.84E2 \pm 5.05
PG0026+129	203.95 \pm 2.70	1.32E1 \pm 2.59E-1	193.68 \pm 0.69	2.72E2 \pm 6.92	671.86 \pm 3.34	2.65E0 \pm 5.18E-2	206.22 \pm 0.68	4.95E2 \pm 2.31E1
PG0043+039	482.21 \pm 17.11	3.17E1 \pm 3.67	40.00 \pm 0.00	4.45E4 \pm 2.46E3	884.88 \pm 3.94	7.84E0 \pm 1.27	149.29 \pm 0.79	1.47E4 \pm 1.20E3
PG0049+171	184.14 \pm 1.05	8.60E-1 \pm 1.24E-1	184.20 \pm 1.06	2.25E1 \pm 5.85E-1	683.54 \pm 12.93	1.72E-1 \pm 4.18E-2	219.69 \pm 0.82	4.44E1 \pm 1.92
PG0050+124	410.84 \pm 3.06	1.64E1 \pm 4.40E-1	68.29 \pm 0.06	2.65E4 \pm 1.32E3	545.32 \pm 1.11	1.42E1 \pm 5.17E-1	143.54 \pm 0.16	1.17E4 \pm 8.64E2
PG0052+251	171.76 \pm 2.23	2.40E1 \pm 5.78	173.53 \pm 2.55	5.15E2 \pm 3.78E1	565.33 \pm 10.01	5.44E0 \pm 5.27	208.04 \pm 1.59	9.25E2 \pm 1.14E2
PG0804+761	407.53 \pm 1.43	1.86E1 \pm 1.98E-1	40.00 \pm 0.00	1.70E4 \pm 4.92E1	819.90 \pm 2.87	3.72E0 \pm 3.97E-2	164.88 \pm 0.12	3.41E3 \pm 9.86
PG0844+349	338.14 \pm 2.85	5.86 \pm 1.66E-1	113.33 \pm 0.60	6.03E2 \pm 2.17E1	699.13 \pm 5.87	1.17E0 \pm 3.32E-2	161.88 \pm 0.41	5.42E2 \pm 3.11E1
PG0921+525	182.74 \pm 0.28	3.14E-1 \pm 7.68E-3	182.81 \pm 0.23	3.74E1 \pm 2.66E-1	1131.80 \pm 11.20	6.28E-2 \pm 1.58E-3	210.67 \pm 0.19	6.16E1 \pm 7.91E-1
PG0923+201	380.40 \pm 8.37	2.74E1 \pm 2.12	40.00 \pm 0.00	2.13E4 \pm 3.82E2	797.53 \pm 6.90	5.93E0 \pm 6.41E-1	154.97 \pm 0.45	4.37E3 \pm 1.20E2
PG0947+396	266.70 \pm 3.48	5.09E1 \pm 2.32	63.40 \pm 1.72	2.57E4 \pm 4.82E2	657.53 \pm 4.39	1.02E1 \pm 5.84E-1	155.23 \pm 0.45	5.14E3 \pm 1.47E2
PG0953+414	340.04 \pm 5.05	3.66E1 \pm 1.42	40.00 \pm 0.00	1.93E4 \pm 8.95E2	842.36 \pm 10.77	7.33E0 \pm 2.83E-1	168.92 \pm 0.79	4.10E3 \pm 2.31E2
PG1001+054	290.92 \pm 9.86	1.82E1 \pm 2.80	71.50 \pm 3.89	9.85E3 \pm 6.15E2	735.20 \pm 24.25	3.63E0 \pm 5.61E-1	160.26 \pm 1.94	1.97E3 \pm 1.23E2
PG1004+130	468.54 \pm 3.29	4.54E1 \pm 9.22E-1	40.00 \pm 0.00	3.86E4 \pm 4.71E2	698.83 \pm 3.42	9.09E0 \pm 1.84E-1	146.45 \pm 0.21	1.51E4 \pm 2.87E2
PG1011-040	308.07 \pm 1.50	5.34 \pm 1.00E-1	71.55 \pm 0.64	3.08E3 \pm 3.22E1	611.19 \pm 3.07	1.07E0 \pm 2.01E-2	161.83 \pm 0.32	6.17E2 \pm 6.45
PG1012+008	373.64 \pm 13.91	1.22E1 \pm 1.74	70.35 \pm 0.88	2.29E4 \pm 1.69E3	608.69 \pm 4.53	1.06E1 \pm 2.04	157.00 \pm 0.51	4.58E3 \pm 6.27E2
PG1048-090	361.13 \pm 62.98	1.80E1 \pm 6.59	176.05 \pm 6.21	1.34E3 \pm 1.32E2	893.65 \pm 63.66	3.59E0 \pm 1.32	184.11 \pm 2.88	2.68E3 \pm 3.31E2
PG1049-005	288.49 \pm 5.18	2.57E2 \pm 2.02E1	72.93 \pm 0.99	2.33E5 \pm 5.33E3	633.50 \pm 1.73	5.93E1 \pm 6.37	148.37 \pm 0.49	4.66E4 \pm 1.07E3
PG1048+342	150.00 \pm 29.39	1.15E1 \pm 4.29	143.79 \pm 50.92	3.80E2 \pm 2.04E2	716.78 \pm 11.33	2.31E0 \pm 8.24	185.77 \pm 4.41	7.60E2 \pm 4.25E2
PG1100+772	349.45 \pm 4.07	6.98E1 \pm 2.22	40.00 \pm 12.94	6.06E3 \pm 3.06E2	754.47 \pm 7.05	1.40E1 \pm 4.43E-1	163.32 \pm 1.24	9.94E3 \pm 8.30E2
PG1103-006	387.23 \pm 13.03	8.87E1 \pm 7.85	117.73 \pm 8.59	7.08E3 \pm 7.01E2	763.72 \pm 17.04	1.77E1 \pm 1.57	163.36 \pm 1.82	1.42E4 \pm 1.40E3
PG1114+445	262.72 \pm 2.61	2.93E1 \pm 5.88E-1	143.85 \pm 1.88	1.57E3 \pm 8.30E1	667.64 \pm 3.48	5.87E0 \pm 1.18E-1	182.72 \pm 0.30	2.90E3 \pm 2.25E2
PG1116+215	366.03 \pm 6.11	3.29E1 \pm 1.52	40.00 \pm 0.00	2.80E4 \pm 9.90E3	902.47 \pm 15.08	6.59E0 \pm 3.04E-1	164.80 \pm 0.54	5.80E3 \pm 7.06E3
PG1121+422	280.10 \pm 5.52	1.86E1 \pm 7.36E-1	172.63 \pm 3.21	2.83E2 \pm 9.47	801.03 \pm 9.87	3.72E0 \pm 1.47E-1	181.64 \pm 1.68	5.65E2 \pm 1.89E1
PG1151+117	332.48 \pm 95.07	1.70E1 \pm 1.09E1	40.00 \pm 9.65	9.87E3 \pm 2.35E3	725.01 \pm 72.48	3.40E0 \pm 7.46	158.87 \pm 3.43	2.02E3 \pm 2.07E3
PG1202+281	320.80 \pm 1.82	2.91E1 \pm 5.72E-1	47.34 \pm 2.63	3.09E4 \pm 1.51E2	644.61 \pm 3.43	5.83E0 \pm 1.14E-1	151.39 \pm 0.17	6.18E3 \pm 3.02E1
PG1211+143	267.00 \pm 4.38	3.99E1 \pm 2.28	118.08 \pm 0.68	1.28E3 \pm 4.38E1	632.66 \pm 10.45	7.99E0 \pm 4.56E-1	167.74 \pm 0.36	2.45E3 \pm 1.17E2
PG1216+069	315.83 \pm 67.65	2.68E1 \pm 2.13	148.30 \pm 27.37	1.38E3 \pm 6.14E2	814.50 \pm 15.37	5.38E0 \pm 4.51E-1	204.81 \pm 5.60	2.19E3 \pm 1.07E3
PG1229+204	276.58 \pm 5.27	3.94 \pm 2.56E-1	115.50 \pm 0.41	5.63E2 \pm 2.02	696.31 \pm 10.99	7.89E-1 \pm 5.13E-2	161.76 \pm 0.11	1.13E3 \pm 4.03
PG1259+593	431.78 \pm 4.93	3.94E1 \pm 1.63	117.00 \pm 4.31	9.87E3 \pm 1.87E3	1014.46 \pm 7.85	7.88E0 \pm 4.16E-1	226.28 \pm 1.54	2.36E3 \pm 6.97E2
PG1302-102	324.63 \pm 2.81	1.23E2 \pm 3.97	55.72 \pm 1.44	1.11E5 \pm 6.85E2	653.52 \pm 2.95	2.46E1 \pm 1.08	155.28 \pm 0.20	2.22E4 \pm 1.37E2
PG1307+085	161.35 \pm 3.15	1.87E1 \pm 5.40	161.47 \pm 3.09	8.20E2 \pm 9.29E1	708.55 \pm 27.93	3.73E0 \pm 8.96	185.39 \pm 1.91	1.43E3 \pm 2.59E2
PG1309+355	441.88 \pm 118.63	1.50E1 \pm 5.49E1	105.79 \pm 1.67	9.14E3 \pm 3.75E3	658.17 \pm 68.58	1.18E1 \pm 4.37E1	167.12 \pm 8.80	5.37E3 \pm 5.52E3
PG1310-108	160.55 \pm 0.49	1.00 \pm 2.31E-2	160.64 \pm 0.32	6.96E1 \pm 8.27E-1	679.46 \pm 4.40	2.00E-1 \pm 4.62E-3	199.48 \pm 0.19	1.03E2 \pm 2.03
PG1322+659	266.61 \pm 1.67	2.94E1 \pm 4.52E-1	51.66 \pm 1.37	1.85E4 \pm 1.11E2	676.31 \pm 3.00	5.89E0 \pm 9.04E-2	151.36 \pm 0.20	3.70E3 \pm 2.21E1
PG1341+258	284.24 \pm 2.73	5.82 \pm 1.70E-1	58.28 \pm 0.85	4.45E3 \pm 3.63E1	658.15 \pm 5.67	1.16E0 \pm 3.40E-2	152.81 \pm 0.27	8.90E2 \pm 7.25
PG1351+640	351.66 \pm 0.60	4.59E1 \pm 2.74E-1	84.16 \pm 0.38	7.07E3 \pm 2.18E1	540.18 \pm 1.75	9.88E0 \pm 1.30E-1	133.05 \pm 0.07	1.41E4 \pm 4.37E1
PG1352+183	248.21 \pm 25.87	5.38E1 \pm 3.09E1	40.00 \pm 1.97	6.43E3 \pm 1.36E3	335.40 \pm 86.50	1.08E1 \pm 6.19	161.73 \pm 5.22	1.29E3 \pm 5.77E2
PG1402+261	403.94 \pm 8.90	1.98E1 \pm 1.58	69.50 \pm 0.24	5.03E4 \pm 5.33E2	661.52 \pm 5.08	1.38E1 \pm 1.57	142.40 \pm 0.36	1.01E4 \pm 1.07E2
PG1404+226	315.15 \pm 5.32	3.37 \pm 2.28E-1	64.89 \pm 0.50	2.53E3 \pm 2.80E1	600.81 \pm 4.64	1.69E0 \pm 1.59E-1	161.12 \pm 0.43	5.07E2 \pm 5.60
PG1411+442	265.36 \pm 17.48	2.35E1 \pm 8.18	59.66 \pm 2.18	7.16E3 \pm 1.37E2	721.91 \pm 49.45	4.70E0 \pm 1.65	171.08 \pm 1.53	1.43E3 \pm 2.75E1
PG1416-129	183.99 \pm 19.61	3.69E-1 \pm 1.47	172.33 \pm 1.38	1.54E2 \pm 2.75	924.34 \pm 29.30	7.38E-1 \pm 2.95	202.23 \pm 0.96	3.08E2 \pm 5.49
PG1426+015	330.84 \pm 2.55	9.90 \pm 2.96E-1	61.10 \pm 0.13	1.33E4 \pm 3.35E1	640.93 \pm 2.12	5.92E0 \pm 2.41E-1	163.35 \pm 0.11	2.66E3 \pm 6.71
PG1435-067	319.81 \pm 3.71	9.28 \pm 5.78E-1	40.00 \pm 30.10	7.73E2 \pm 1.09E2	729.28 \pm 14.00	1.86E0 \pm 1.16E-1	182.86 \pm 4.48	7.92E2 \pm 1.23E2
PG1444+407	434.56 \pm 6.63	2.75E1 \pm 1.57	65.56 \pm 0.92	4.88E4 \pm 5.13E2	662.35 \pm 2.16	1.68E1 \pm 1.30	161.15 \pm 0.36	9.77E3 \pm 1.03E2
PG1512+370	367.38 \pm 4.50	4.52E1 \pm 1.80	90.10 \pm 0.84	2.75E4 \pm 6.92E2	818.86 \pm 5.81	9.26E0 \pm 5.43E-1	184.86 \pm 0.85	5.50E3 \pm 1.38E2
PG1534+580	240.61 \pm 31.24	1.59 \pm 8.29	128.85 \pm 43.61	1.07E2 \pm 1.60E2	694.01 \pm 85.59	3.18E-1 \pm 1.66	170.48 \pm 6.01	2.14E2 \pm 3.22E2
PG1535+547	239.98 \pm 0.79	2.23 \pm 1.89E-2	49.95 \pm 0.54	6.48E2 \pm 7.14E1	776.61 \pm 2.20	4.46E-1 \pm 3.78E-3	183.34 \pm 0.15	1.30E2 \pm 4.26E1

Table 1—Continued

Source	T_w^S (K)	M_w^S (M_\odot)	T_c^S (K)	M_c^S (M_\odot)	T_w^G (K)	M_w^G (M_\odot)	T_c^G (K)	M_c^G (M_\odot)
(1)	(2)	(3)	(4)	(5)	(6)	(7)	(8)	(9)
PG1545+210	173.68 \pm 38.91	2.39E1 \pm 1.04E1	172.48 \pm 3.50	7.86E2 \pm 2.87E1	857.38 \pm 19.41	4.84E0 \pm 1.92E1	199.93 \pm 1.23	1.57E3 \pm 7.94E1
PG1552+085	401.77 \pm 61.66	1.67 \pm 6.81	72.47 \pm 1.39	2.93E3 \pm 9.96E1	602.90 \pm 16.89	3.34E0 \pm 1.37E1	173.79 \pm 0.89	5.87E2 \pm 1.99E1
PG1617+175	339.70 \pm 26.44	1.25E1 \pm 6.77	53.90 \pm 2.02	5.92E3 \pm 2.25E2	757.72 \pm 55.33	2.50E0 \pm 1.36	163.43 \pm 2.53	1.18E3 \pm 4.50E1
PG1626+554	314.90 \pm 20.66	3.68 \pm 1.27	225.05 \pm 5.27	6.18E1 \pm 5.03	834.28 \pm 77.72	7.35E-1 \pm 1.01	214.70 \pm 2.58	1.24E2 \pm 1.37E1
PG1700+518	365.49 \pm 8.00	1.43E2 \pm 9.85	76.48 \pm 0.34	2.07E5 \pm 2.29E3	640.92 \pm 7.26	7.55E1 \pm 7.23	153.06 \pm 0.34	4.14E4 \pm 4.58E2
PG1704+608	395.20 \pm 2.70	1.16E2 \pm 2.15	40.00 \pm 0.00	1.93E5 \pm 6.08E3	837.88 \pm 4.76	2.31E1 \pm 4.31E-1	138.84 \pm 0.19	8.70E4 \pm 3.76E3
PG2112+059	352.84 \pm 2.46	2.15E2 \pm 8.04	100.75 \pm 2.60	8.25E4 \pm 8.20E3	819.08 \pm 3.03	4.71E1 \pm 2.20	190.72 \pm 2.63	1.65E4 \pm 1.64E3
PG2209+184	288.22 \pm 2.85	3.16 \pm 9.52E-2	60.48 \pm 1.03	8.10E2 \pm 1.07E1	716.31 \pm 6.56	6.32E-1 \pm 1.90E-2	176.17 \pm 0.62	1.62E2 \pm 2.14
PG2214+139	314.14 \pm 1.03	7.78 \pm 8.73E-2	51.91 \pm 1.17	6.18E2 \pm 9.14E1	827.31 \pm 3.17	1.56E0 \pm 1.75E-2	182.26 \pm 0.18	5.02E2 \pm 1.05E2
PG2233+134	253.00 \pm 26.06	1.55E2 \pm 2.18E1	143.65 \pm 4.18	5.98E3 \pm 2.95E2	592.41 \pm 15.16	3.11E1 \pm 4.93	155.43 \pm 1.25	1.20E4 \pm 5.89E2
PG2251+113	334.92 \pm 34.85	5.47E1 \pm 8.93E1	40.00 \pm 26.51	3.00E3 \pm 2.09E2	735.66 \pm 100.48	1.09E1 \pm 1.79E1	183.65 \pm 7.21	6.01E3 \pm 4.17E2
PG2304+042	150.00 \pm 17.07	5.04E-2 \pm 3.08E-1	194.77 \pm 1.46	1.22E1 \pm 6.53E-1	1500.00 \pm 356.30	1.20E-2 \pm 8.08E-2	217.36 \pm 4.98	2.44E1 \pm 1.31
PG2308+098	197.34 \pm 12.19	4.42 \pm 1.14E1	197.39 \pm 0.72	1.67E3 \pm 3.68E1	871.36 \pm 12.40	8.84E0 \pm 2.29E1	192.43 \pm 1.63	3.34E3 \pm 7.36E1
2MASSJ081652.2+425829	319.66 \pm 19.84	1.48E1 \pm 5.86	40.00 \pm 35.45	3.71E3 \pm 1.42E3	719.47 \pm 65.88	2.96E0 \pm 1.17	176.42 \pm 18.26	7.64E2 \pm 7.09E2
2MASSJ095504.5+170556	178.45 \pm 40.51	7.34 \pm 3.20	172.85 \pm 5.58	1.64E2 \pm 8.58	731.20 \pm 19.56	1.47E0 \pm 6.04	181.01 \pm 1.92	3.27E2 \pm 2.05E1
2MASSJ130005.3+163214	150.00 \pm 0.00	1.74E1 \pm 3.99	137.78 \pm 2.74	5.40E2 \pm 4.89E1	715.68 \pm 14.96	3.48E0 \pm 7.52	189.57 \pm 0.51	9.41E2 \pm 1.26E2
2MASSJ132917.5+121340	255.49 \pm 82.96	2.08E1 \pm 9.70	81.99 \pm 9.98	3.25E3 \pm 8.51E2	562.71 \pm 37.76	5.22E0 \pm 9.53	179.31 \pm 8.73	6.49E2 \pm 1.70E2
2MASSJ1402511+263117	191.28 \pm 27.29	2.33 \pm 8.62	156.37 \pm 9.90	3.51E2 \pm 3.52E1	729.98 \pm 14.12	4.65E0 \pm 1.73E1	197.07 \pm 2.02	7.01E2 \pm 7.56E1
2MASSJ145608.6+275008	330.00 \pm 63.97	2.58E1 \pm 5.95E1	84.98 \pm 15.50	1.72E4 \pm 1.34E4	698.81 \pm 95.40	8.58E0 \pm 2.04E1	164.89 \pm 13.87	3.44E3 \pm 2.67E3
2MASSJ151653.2+190048	323.31 \pm 12.31	1.03E2 \pm 1.58E1	40.00 \pm 0.00	4.75E4 \pm 6.65E2	683.70 \pm 6.98	2.86E1 \pm 6.09	156.70 \pm 0.76	1.02E4 \pm 1.49E2
2MASSJ151901.5+183804	350.92 \pm 23.98	4.37 \pm 9.66E-1	83.62 \pm 3.96	3.59E3 \pm 4.69E2	821.46 \pm 59.21	8.74E-1 \pm 2.51E-1	158.54 \pm 3.72	7.18E2 \pm 9.39E1
2MASSJ154307.7+193751	246.49 \pm 36.20	1.63E2 \pm 3.89E1	40.00 \pm 0.00	5.70E4 \pm 7.63E3	597.44 \pm 20.57	3.25E1 \pm 3.81E1	152.52 \pm 1.94	1.14E4 \pm 3.35E3
2MASSJ222221.1+195947	312.89 \pm 6.62	3.64E1 \pm 2.55	40.00 \pm 0.00	2.03E4 \pm 2.51E2	719.87 \pm 13.54	7.29E0 \pm 5.11E-1	166.80 \pm 0.58	4.07E3 \pm 5.03E1
2MASSJ223742.6+145614	262.58 \pm 11.27	6.18E1 \pm 7.75	71.60 \pm 24.54	2.63E4 \pm 8.85E3	586.67 \pm 18.74	1.24E1 \pm 1.55	144.68 \pm 9.83	5.25E3 \pm 1.77E3
2MASSJ234259.3+134750	338.21 \pm 50.33	3.61E1 \pm 1.94E1	96.94 \pm 5.53	1.95E4 \pm 3.72E3	606.38 \pm 67.85	7.22E0 \pm 3.88	146.57 \pm 6.14	3.90E3 \pm 1.17E3
2MASSJ234449.5+122143	296.00 \pm 40.78	3.96E1 \pm 1.77E1	71.45 \pm 2.01	4.13E4 \pm 2.45E3	625.95 \pm 31.90	9.22E0 \pm 4.26	144.47 \pm 1.91	8.25E3 \pm 4.89E2
2MASXJ09210862+4538575	219.07 \pm 49.13	6.97 \pm 8.66	163.39 \pm 9.07	1.55E2 \pm 1.96E1	666.39 \pm 131.72	1.39E0 \pm 4.00	200.06 \pm 7.72	3.10E2 \pm 4.21E1
2MASXJ00370409-0109081	295.44 \pm 32.02	1.20 \pm 3.08E-1	127.84 \pm 37.46	1.89E1 \pm 7.88	637.13 \pm 52.61	2.39E-1 \pm 8.98E-2	178.78 \pm 3.99	3.78E1 \pm 1.61E1
2MASXJ02335161+0108136	634.16 \pm 198.50	1.18E-2 \pm 4.37E-3	64.09 \pm 0.66	1.10E2 \pm 7.82	1288.37 \pm 140.98	2.35E-3 \pm 1.08E-3	132.70 \pm 2.15	2.21E1 \pm 1.56
2MASXJ07582810+3747121	345.77 \pm 106.23	8.08E-2 \pm 1.84E-1	58.13 \pm 23.66	5.79E1 \pm 4.24E1	931.25 \pm 185.08	2.20E-2 \pm 5.18E-2	152.34 \pm 11.18	2.93E1 \pm 4.80E1
2MASXJ0208238-002000	236.18 \pm 8.17	5.12 \pm 6.54E-1	126.35 \pm 8.32	9.27E1 \pm 2.88E1	492.74 \pm 17.14	1.02E0 \pm 1.31E-1	168.73 \pm 2.05	1.85E2 \pm 6.52E1
2MASXJ02061600-0017292	296.29 \pm 3.04	3.39 \pm 1.13E-1	58.80 \pm 4.61	5.57E2 \pm 1.95E2	746.93 \pm 7.76	6.79E-1 \pm 2.25E-2	175.24 \pm 0.81	1.87E2 \pm 8.45E1
2MASXJ10493088+2257523	150.00 \pm 10.34	1.22E-1 \pm 3.72E-1	139.69 \pm 9.98	1.04E2 \pm 4.15	712.89 \pm 8.52	2.45E-1 \pm 7.50E-1	173.89 \pm 0.57	2.08E2 \pm 8.30
2MASXJ12485992-0109353	301.01 \pm 5.02	2.33E1 \pm 1.59	42.06 \pm 1.43	3.54E4 \pm 2.62E2	490.22 \pm 6.89	4.66E0 \pm 3.18E-1	136.12 \pm 0.29	7.07E3 \pm 5.26E1
2MASXJ14070036+2827141	334.20 \pm 2.02	4.63E1 \pm 9.03E-1	62.77 \pm 0.08	5.47E4 \pm 2.11E2	581.09 \pm 2.49	9.27E0 \pm 1.81E-1	134.13 \pm 0.14	1.09E4 \pm 4.23E1
2MASXJ02143357-0046002	267.91 \pm 3.67	2.45 \pm 1.31E-1	56.11 \pm 0.49	2.10E3 \pm 1.18E1	539.30 \pm 6.50	4.89E-1 \pm 2.62E-2	153.40 \pm 0.25	4.20E2 \pm 2.36
2MASXJ09234300+2254324	237.82 \pm 4.77	6.93 \pm 8.41E-1	112.27 \pm 3.56	1.38E2 \pm 3.10E1	575.01 \pm 13.89	1.39E0 \pm 1.68E-1	171.89 \pm 0.95	2.77E2 \pm 6.95E1
2MASXJ12170991+0711299	302.86 \pm 26.60	5.82E-2 \pm 2.24E-1	57.72 \pm 3.07	6.02E1 \pm 1.30E1	566.17 \pm 47.07	3.81E-2 \pm 1.47E-1	143.98 \pm 13.98	1.20E1 \pm 1.37E1
2MASXJ12232410+0240449	270.26 \pm 29.61	4.20E-1 \pm 7.78E-2	170.29 \pm 9.67	5.35 \pm 9.59E-1	710.58 \pm 31.95	8.39E-2 \pm 1.56E-2	190.11 \pm 1.87	1.07E1 \pm 2.27
2MASXJ13381586+0432330	370.52 \pm 4.78	5.01E-1 \pm 2.07E-2	63.94 \pm 0.22	3.38E2 \pm 9.51	985.22 \pm 15.52	1.00E-1 \pm 4.15E-3	159.66 \pm 0.33	1.22E2 \pm 4.98
2MASXJ13495283+0204456	207.83 \pm 4.27	2.52 \pm 1.09E-1	129.11 \pm 1.38	4.83E1 \pm 7.08E-1	534.18 \pm 5.39	5.04E-1 \pm 2.18E-2	168.67 \pm 0.53	9.65E1 \pm 1.42
2MASXJ23044349-0841084	295.60 \pm 1.63	5.41 \pm 9.96E-2	62.65 \pm 0.12	6.90E3 \pm 2.83E1	721.66 \pm 4.11	1.08E0 \pm 1.99E-2	150.29 \pm 0.16	1.38E3 \pm 5.65
SDSSJ115138.24+004946.4	334.95 \pm 148.97	3.62 \pm 4.29	155.57 \pm 7.42	1.77E2 \pm 1.85E1	696.58 \pm 154.45	7.23E-1 \pm 1.58	193.56 \pm 6.91	3.54E2 \pm 3.71E1
SDSSJ170246.09+602818.8	325.32 \pm 165.85	3.21E-1 \pm 4.02E-1	51.97 \pm 22.73	1.62E2 \pm 6.62E1	512.92 \pm 77.13	8.84E-2 \pm 2.60E-1	137.93 \pm 7.20	3.85E1 \pm 7.19E1

Table 2. Model Parameters for 30 AGNs Which Show No Silicate Emission but a Featureless Thermal Continuum

Source (1)	T_w^S (K) (2)	M_w^S (M_\odot) (3)	T_c^S (K) (4)	M_c^S (M_\odot) (5)	T_w^G (K) (6)	M_w^G (M_\odot) (7)	T_c^G (K) (8)	M_c^G (M_\odot) (9)
PG0838+770	383.27 \pm 23.92	4.53 \pm 8.96E-1	65.69 \pm 0.16	6.98E3 \pm 3.89E2	552.66 \pm 9.14	5.89 \pm 1.19	150.94 \pm 0.18	3.83E3 \pm 3.02E2
PG1226+023	245.43 \pm 0.53	3.09E2 \pm 1.01	40.00 \pm 0.00	1.34E5 \pm 2.51E3	686.41 \pm 0.65	6.18E1 \pm 2.01E-1	152.17 \pm 0.06	3.90E4 \pm 1.13E3
PG1354+213	521.75 \pm 22.11	3.69 \pm 5.67E-1	52.09 \pm 4.04	4.14E4 \pm 9.19E2	713.85 \pm 5.54	7.39 \pm 1.32	155.59 \pm 0.39	8.28E3 \pm 2.66E2
PG1427+480	150.00 \pm 75.01	1.44E1 \pm 1.48E1	72.71 \pm 3.53	3.66E4 \pm 3.27E3	624.51 \pm 26.38	7.88 \pm 8.23	149.61 \pm 2.12	7.33E3 \pm 6.55E2
PG1448+273	239.30 \pm 1.20	5.19 \pm 6.88E-2	40.00 \pm 0.00	3.74E3 \pm 9.85	607.59 \pm 2.16	1.04 \pm 1.38E-2	171.10 \pm 0.10	7.50E2 \pm 2.12
PG1501+106	178.91 \pm 1.10	4.25 \pm 5.59E-2	48.99 \pm 0.27	5.04E3 \pm 6.90	606.14 \pm 2.14	8.51E-1 \pm 1.12E-2	166.72 \pm 0.06	1.01E3 \pm 1.38
PG1543+489	291.97 \pm 2.11	1.18E2 \pm 2.60	85.60 \pm 0.15	1.98E5 \pm 1.30E3	570.60 \pm 1.07	9.47E1 \pm 2.86	163.69 \pm 0.21	3.96E4 \pm 2.60E2
2MASSJ010835.1+214818	184.20 \pm 10.74	1.68E2 \pm 7.13	73.28 \pm 1.07	7.98E4 \pm 1.53E3	599.78 \pm 6.37	3.35E1 \pm 1.43	158.67 \pm 0.71	1.60E4 \pm 6.32E2
2MASSJ024807.3+145957	150.00 \pm 32.16	1.71E1 \pm 3.71	70.70 \pm 1.11	6.23E3 \pm 4.01E2	485.88 \pm 23.01	4.75 \pm 1.89	146.55 \pm 2.27	1.25E3 \pm 8.02E1
2MASSJ082311.3+435318	150.00 \pm 13.68	6.49E1 \pm 1.09E1	74.37 \pm 2.94	2.76E4 \pm 1.70E3	566.30 \pm 24.85	1.30E1 \pm 2.20	158.99 \pm 2.54	5.75E3 \pm 5.99E2
2MASSJ145410.1+195648	150.00 \pm 0.52	8.04E1 \pm 2.71E1	98.49 \pm 25.43	2.98E3 \pm 4.03E3	620.35 \pm 21.97	1.61E1 \pm 4.76E1	162.54 \pm 3.15	3.54E3 \pm 4.90E3
2MASXJ17223993+3052521	150.00 \pm 0.05	1.62 \pm 2.77	64.56 \pm 3.48	2.82E3 \pm 1.94E2	476.09 \pm 15.79	1.53 \pm 2.65	143.04 \pm 2.05	5.63E2 \pm 3.88E1
2MASXJ13130577+0127561	150.00 \pm 37.35	2.55E-2 \pm 5.32E-2	154.25 \pm 30.08	3.13 \pm 7.66E-1	813.23 \pm 193.63	5.19E-3 \pm 2.33E-2	170.28 \pm 4.49	6.26 \pm 1.58
SDSSJ090738.71+564358.2	150.00 \pm 0.00	1.41 \pm 7.77E-1	68.76 \pm 1.55	1.80E3 \pm 2.63E2	433.34 \pm 65.60	1.24 \pm 9.42E-1	138.17 \pm 5.04	3.60E2 \pm 5.27E1
2MASXJ13130565-0210390	239.94 \pm 21.18	1.79 \pm 9.33E-1	59.06 \pm 1.65	1.00E3 \pm 5.75E2	605.56 \pm 13.36	8.50E-1 \pm 5.75E-1	158.14 \pm 0.96	4.29E2 \pm 3.53E2
SDSSJ124035.81-002919.4	234.95 \pm 15.11	6.42 \pm 3.82	47.57 \pm 4.20	4.77E3 \pm 1.24E2	523.27 \pm 27.32	1.28 \pm 7.67E-1	144.28 \pm 1.16	9.55E2 \pm 2.50E1
2MASXJ15055659+0342267	260.53 \pm 2.21	3.37 \pm 9.97E-2	60.44 \pm 0.18	3.39E3 \pm 1.32E1	588.28 \pm 4.49	6.75E-1 \pm 1.99E-2	151.76 \pm 0.17	6.77E2 \pm 2.63
2MASXJ09191322+5527552	237.54 \pm 41.58	3.25 \pm 7.86E-1	58.53 \pm 0.72	2.48E3 \pm 1.98E1	565.31 \pm 11.69	7.43E-1 \pm 1.09	152.32 \pm 0.48	4.96E2 \pm 3.96
SDSSJ101536.21+005459.3	150.00 \pm 0.00	1.92E1 \pm 7.46E-1	137.51 \pm 1.52	4.15E2 \pm 2.02E1	489.77 \pm 5.63	3.84 \pm 1.49E-1	163.49 \pm 0.46	8.29E2 \pm 5.15E1
SDSSJ164840.15+425547.6	150.00 \pm 63.25	1.78 \pm 5.35	62.28 \pm 5.46	3.68E3 \pm 5.79E2	473.91 \pm 36.12	1.58 \pm 4.83	139.21 \pm 4.10	7.36E2 \pm 1.16E2
SDSSJ091414.34+023801.7	186.93 \pm 39.59	1.37 \pm 2.68	63.66 \pm 7.25	1.43E3 \pm 2.01E2	461.95 \pm 51.19	4.55E-1 \pm 9.29E-1	138.76 \pm 4.10	2.87E2 \pm 4.02E1
2MASXJ12384342+0927362	150.00 \pm 0.00	2.27E1 \pm 2.26	106.73 \pm 1.92	1.25E3 \pm 6.21E1	472.61 \pm 3.80	4.53 \pm 4.10	151.59 \pm 0.32	2.50E3 \pm 1.58E2
2MASXJ16164729+3716209	172.57 \pm 7.27	7.62E1 \pm 5.10	40.00 \pm 25.60	5.73E3 \pm 3.38E2	458.47 \pm 4.28	1.54E1 \pm 1.39	140.99 \pm 1.24	1.15E4 \pm 6.76E2
2MASXJ11230133+4703088	265.83 \pm 24.90	7.07E-2 \pm 1.59E-2	59.62 \pm 1.05	1.23E2 \pm 3.12	781.16 \pm 65.83	1.41E-2 \pm 3.18E-3	161.03 \pm 1.10	2.46E1 \pm 6.23E-1
2MASXJ11110693+0228477	150.00 \pm 25.49	2.65 \pm 4.10E-1	67.55 \pm 0.52	5.76E2 \pm 1.15E1	467.19 \pm 7.51	7.11E-1 \pm 2.17E-1	165.19 \pm 1.31	1.15E2 \pm 2.30
2MASSJ1448250+355946	280.42 \pm 3.96	1.70E1 \pm 1.25	68.10 \pm 0.23	9.34E3 \pm 2.77E3	499.67 \pm 5.73	6.40 \pm 7.16E-1	133.97 \pm 0.62	6.25E3 \pm 2.33E3
SDSSJ164019.66+403744.4	150.00 \pm 2.41	6.47 \pm 2.37E1	137.20 \pm 5.40	4.33E2 \pm 1.12E2	474.61 \pm 78.43	1.29 \pm 5.42	151.75 \pm 8.34	4.30E2 \pm 1.70E2
SDSSJ104058.79+581703.3	229.68 \pm 96.48	1.45 \pm 9.23E-1	40.00 \pm 3.30	8.74E2 \pm 8.44E1	514.64 \pm 44.30	2.91E-1 \pm 9.53E-1	147.45 \pm 3.01	1.75E2 \pm 1.98E1
UGC05984	235.37 \pm 22.94	3.49E-1 \pm 1.55	59.41 \pm 1.00	9.82E2 \pm 5.76E1	535.89 \pm 79.68	6.98E-2 \pm 3.11E-1	138.12 \pm 2.54	1.96E2 \pm 1.15E1
UGC06527	218.61 \pm 1.50	3.05 \pm 4.19E-2	60.02 \pm 0.23	1.51E3 \pm 5.12	567.10 \pm 2.08	6.10E-1 \pm 8.38E-3	159.92 \pm 0.14	3.01E2 \pm 1.02

Table 3. Model Parameters for 24 AGNs Which Show a Thermal Continuum Superimposed with PAH Features

Source (1)	T_w^S (K) (2)	M_w^S (M_\odot) (3)	T_c^S (K) (4)	M_c^S (M_\odot) (5)	T_w^G (K) (6)	M_w^G (M_\odot) (7)	T_c^G (K) (8)	M_c^G (M_\odot) (9)
PG0007+106	264.22 \pm 3.52	1.34E1 \pm 7.21E-1	59.13 \pm 0.23	1.71E4 \pm 5.29E1	624.16 \pm 3.28	4.60 \pm 3.29E-1	146.49 \pm 0.12	3.42E3 \pm 1.06E1
PG0157+001	342.59 \pm 0.69	1.07E2 \pm 7.54E-1	63.67 \pm 0.14	9.94E5 \pm 4.06E3	558.03 \pm 0.90	2.14E1 \pm 1.51E-1	116.62 \pm 0.07	1.99E5 \pm 8.12E2
PG0923+129	184.57 \pm 0.82	4.91 \pm 3.59E-2	57.39 \pm 0.14	2.33E3 \pm 4.81	549.11 \pm 1.06	9.81E-1 \pm 7.19E-3	156.94 \pm 0.09	4.66E2 \pm 9.62E-1
PG0934+013	207.87 \pm 2.91	6.91 \pm 1.95E-1	65.89 \pm 0.09	3.55E3 \pm 1.54E1	505.09 \pm 3.45	1.38 \pm 3.89E-2	142.56 \pm 0.15	7.10E2 \pm 3.08
PG1022+519	199.99 \pm 2.04	2.46 \pm 2.52E-1	64.38 \pm 0.14	1.75E3 \pm 1.52E1	509.99 \pm 1.94	1.05 \pm 1.46E-1	138.17 \pm 0.34	3.49E2 \pm 3.03
PG1115+407	150.00 \pm 7.09	1.36E1 \pm 8.85	73.56 \pm 6.62	1.22E4 \pm 2.04E3	617.87 \pm 17.67	6.25 \pm 4.18	158.95 \pm 3.95	2.44E3 \pm 4.08E2
PG1119+120	239.27 \pm 3.08	7.45 \pm 5.97E-1	65.26 \pm 0.18	7.74E3 \pm 3.41E1	478.03 \pm 1.95	4.98 \pm 5.27E-1	147.76 \pm 0.18	1.55E3 \pm 6.82
PG1126-041	150.00 \pm 0.00	2.88 \pm 2.01E-1	67.04 \pm 0.06	1.16E4 \pm 2.23E1	770.16 \pm 3.85	1.94 \pm 1.99E-1	155.06 \pm 0.07	2.32E3 \pm 4.45
PG1149-110	210.57 \pm 2.44	3.45 \pm 6.47E-2	49.91 \pm 0.39	3.89E3 \pm 1.08E1	605.99 \pm 3.26	6.91E-1 \pm 1.29E-2	151.38 \pm 0.10	7.78E2 \pm 2.15
PG1244+026	267.05 \pm 2.18	2.61 \pm 9.20E-2	68.36 \pm 0.15	1.79E3 \pm 1.12E2	482.88 \pm 2.54	1.75 \pm 8.76E-2	143.43 \pm 0.26	7.83E2 \pm 7.03E1
PG1415+451	215.73 \pm 2.14	2.16E1 \pm 1.49	66.63 \pm 0.37	9.46E3 \pm 4.82E1	573.56 \pm 1.88	5.25 \pm 5.13E-1	154.77 \pm 0.19	1.89E3 \pm 9.64
PG1425+267	288.67 \pm 9.53	1.31E2 \pm 1.62E1	73.65 \pm 1.09	8.95E4 \pm 2.30E3	655.00 \pm 3.73	2.74E1 \pm 5.37	156.77 \pm 0.56	1.79E4 \pm 4.90E2
PG1519+226	247.49 \pm 2.56	1.57E1 \pm 7.42E-1	70.14 \pm 0.47	1.11E4 \pm 8.56E1	637.60 \pm 1.84	6.68 \pm 4.77E-1	163.31 \pm 0.28	2.21E3 \pm 1.71E1
PG1612+261	223.24 \pm 1.19	3.15E1 \pm 2.78E-1	40.00 \pm 0.00	2.51E4 \pm 7.41E1	610.56 \pm 1.51	6.30 \pm 5.56E-2	150.61 \pm 0.10	5.01E3 \pm 1.50E1
PG1613+658	150.00 \pm 0.00	1.26E2 \pm 8.70	68.19 \pm 0.07	5.41E4 \pm 1.36E2	571.74 \pm 1.05	2.94E1 \pm 3.54	155.68 \pm 0.08	1.08E4 \pm 2.72E1
PG2130+099	150.00 \pm 0.00	1.06E1 \pm 1.70E-1	66.86 \pm 0.19	1.21E4 \pm 3.47E1	609.57 \pm 1.15	5.88 \pm 1.34E-1	159.42 \pm 0.10	2.42E3 \pm 6.95
2MASSJ165939.7+183436	150.00 \pm 2.60	5.45E1 \pm 9.40E1	76.87 \pm 8.09	5.25E4 \pm 1.25E4	492.49 \pm 21.82	3.57E1 \pm 6.19E1	153.14 \pm 5.03	1.05E4 \pm 2.49E3
2MASXJ08381094+2453427	250.83 \pm 3.62	1.04 \pm 4.96E-2	62.80 \pm 0.20	1.15E3 \pm 7.04	595.64 \pm 7.61	2.07E-1 \pm 9.93E-3	152.54 \pm 0.25	2.30E2 \pm 1.41
2MASXJ22533142+0048252	191.06 \pm 6.43	8.76 \pm 8.54E-1	89.88 \pm 31.24	2.15E2 \pm 2.44E1	457.59 \pm 9.73	1.75 \pm 2.23E-1	154.25 \pm 2.55	4.30E2 \pm 4.89E1
2MASXJ15085397-0011486	244.12 \pm 4.23	2.24 \pm 7.37E-2	45.04 \pm 0.75	3.80E3 \pm 1.75E1	707.77 \pm 7.34	4.47E-1 \pm 1.47E-2	154.11 \pm 0.17	7.59E2 \pm 3.50
2MASXJ14175951+2508124	216.15 \pm 1.76	4.55 \pm 1.21E-1	63.11 \pm 0.06	2.34E3 \pm 6.80	477.36 \pm 3.04	9.10E-1 \pm 2.41E-2	140.46 \pm 0.12	4.67E2 \pm 1.36
2MASXJ12042964+2018581	281.38 \pm 15.51	1.12 \pm 1.34E-1	65.10 \pm 0.14	1.55E3 \pm 1.16E1	538.85 \pm 7.81	5.90E-1 \pm 1.15E-1	145.77 \pm 0.35	3.10E2 \pm 2.32
2MASXJ10032788+5541535	218.90 \pm 15.85	4.83 \pm 1.15	58.48 \pm 3.03	2.01E3 \pm 8.48E1	502.65 \pm 26.73	9.65E-1 \pm 2.85E-1	158.26 \pm 1.69	4.02E2 \pm 1.76E1
2MASSJ16593976+1834367	237.46 \pm 29.89	6.83E1 \pm 1.40E2	73.17 \pm 7.24	7.24E4 \pm 1.06E4	507.00 \pm 24.51	4.55E1 \pm 9.60E1	150.69 \pm 3.81	1.45E4 \pm 2.12E3

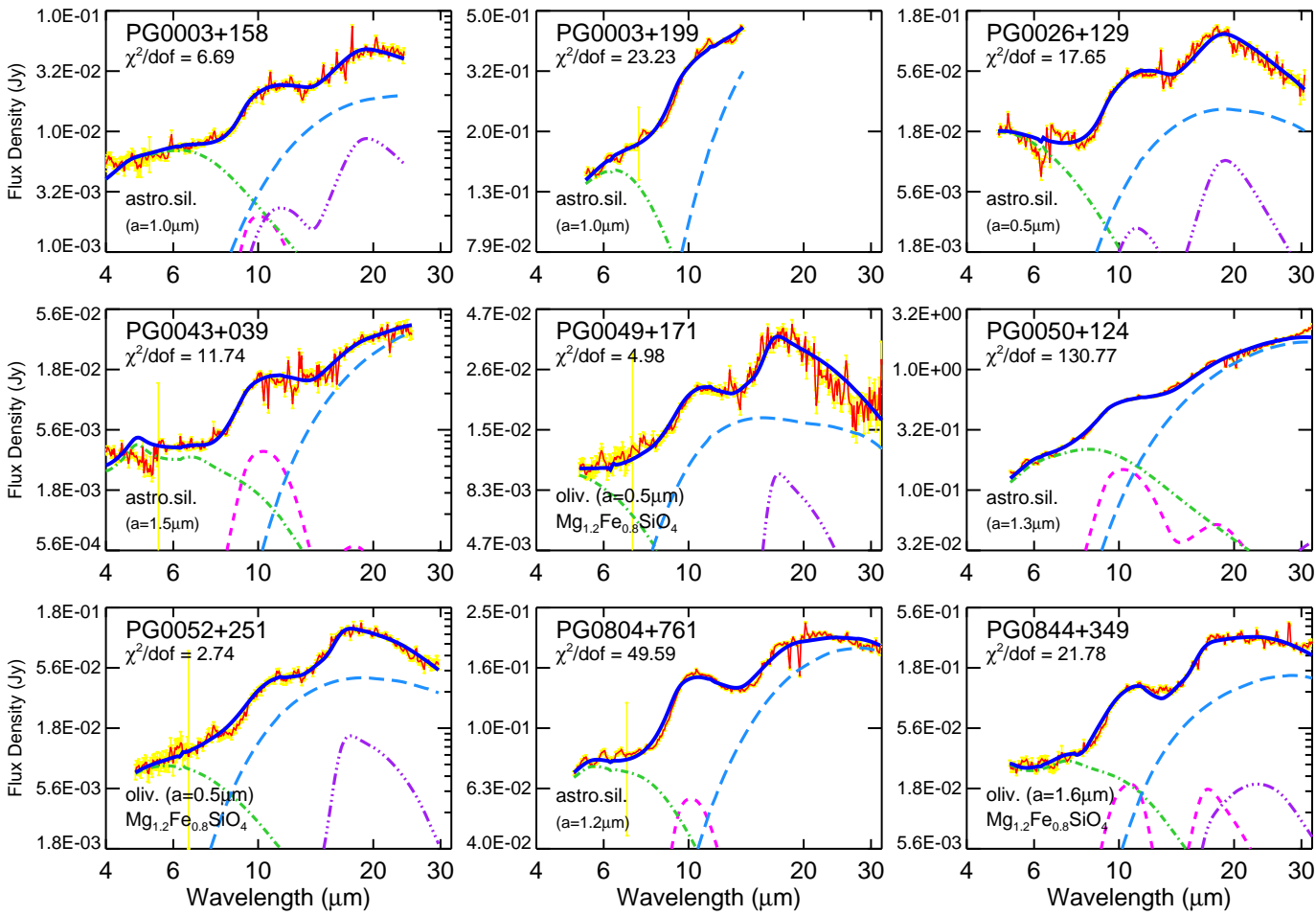


Fig. 1.— Comparison of the *Spitzer*/IRS spectra (red solid lines) of the PG quasars PG0003+158, PG0003+199, PG0026+129, PG0043+039, PG0049+171, PG0050+124, PG0052+251, PG0804+761, PG0844+349 which show silicate emission around 9.7 and 18 μm with the model spectra (blue solid lines) which are the sum of warm silicate (magenta short dashed lines), cold silicate (purple dash-dot-dotted lines), warm graphite (green dash-dotted lines), and cold graphite (light blue long dashed lines). Also shown are the observed 1 σ errors (yellow vertical lines).

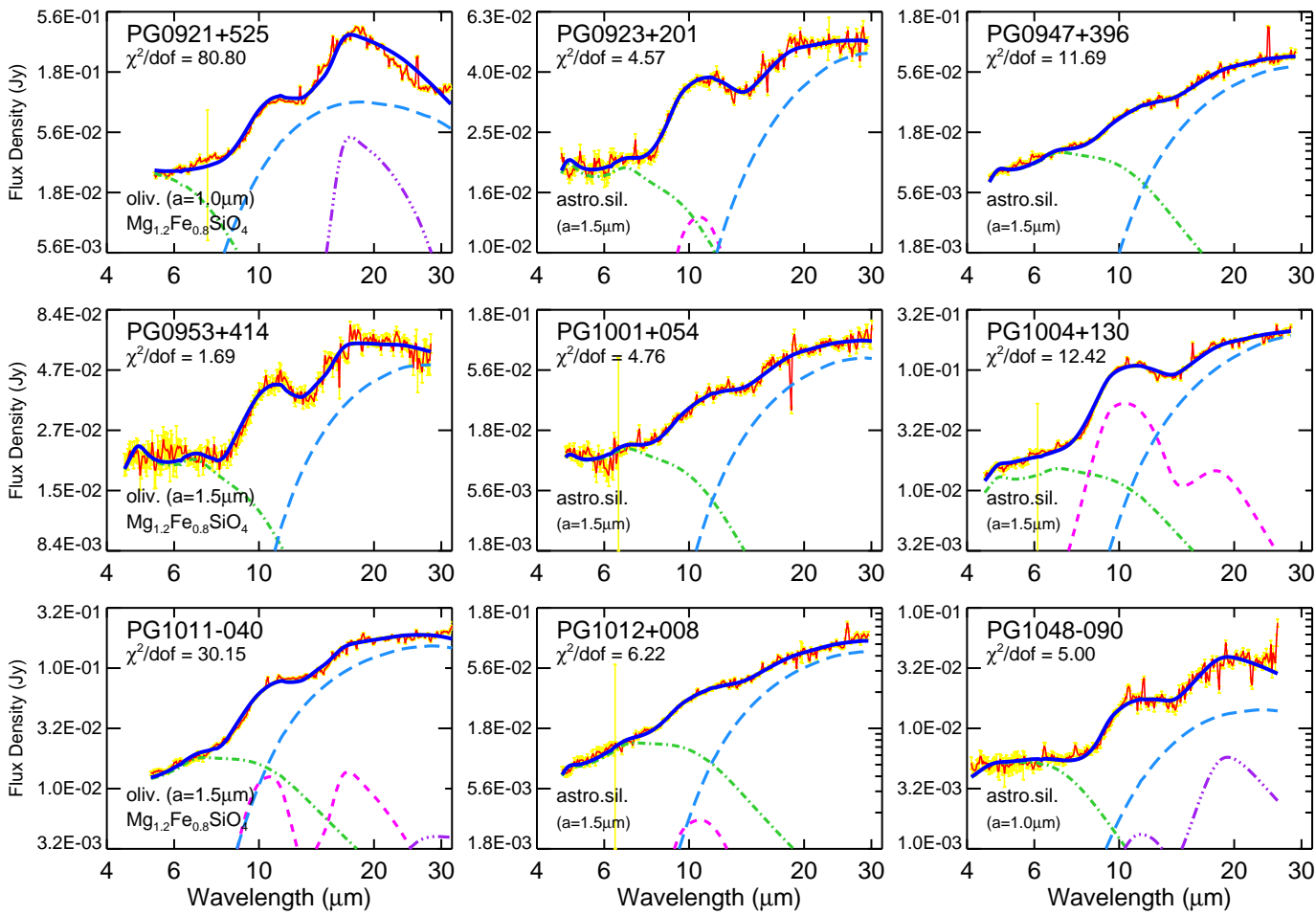


Fig. 1.— Continued, but for the PG quasars PG0921+525, PG0923+201, PG0947+396, PG0953+414, PG1001+054, PG1004+130, PG1011-040, PG1012+008, and PG1048-090.

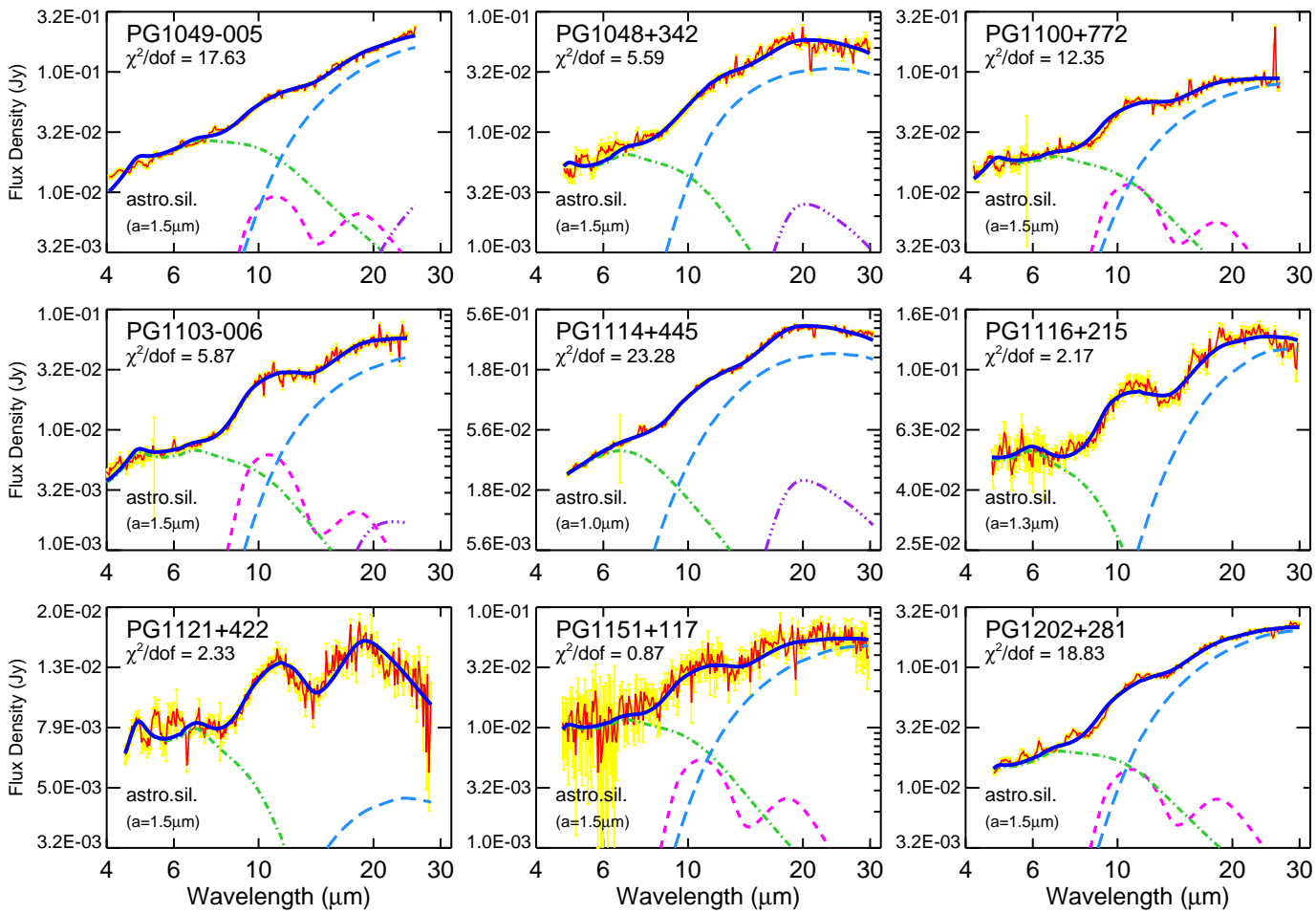


Fig. 1. — Continued, but for the PG quasars PG1049-005, PG1048+342, PG1100+772, PG1103-006, PG1114+445, PG1116+215, PG1121+422, PG1151+117, and PG1202+281.

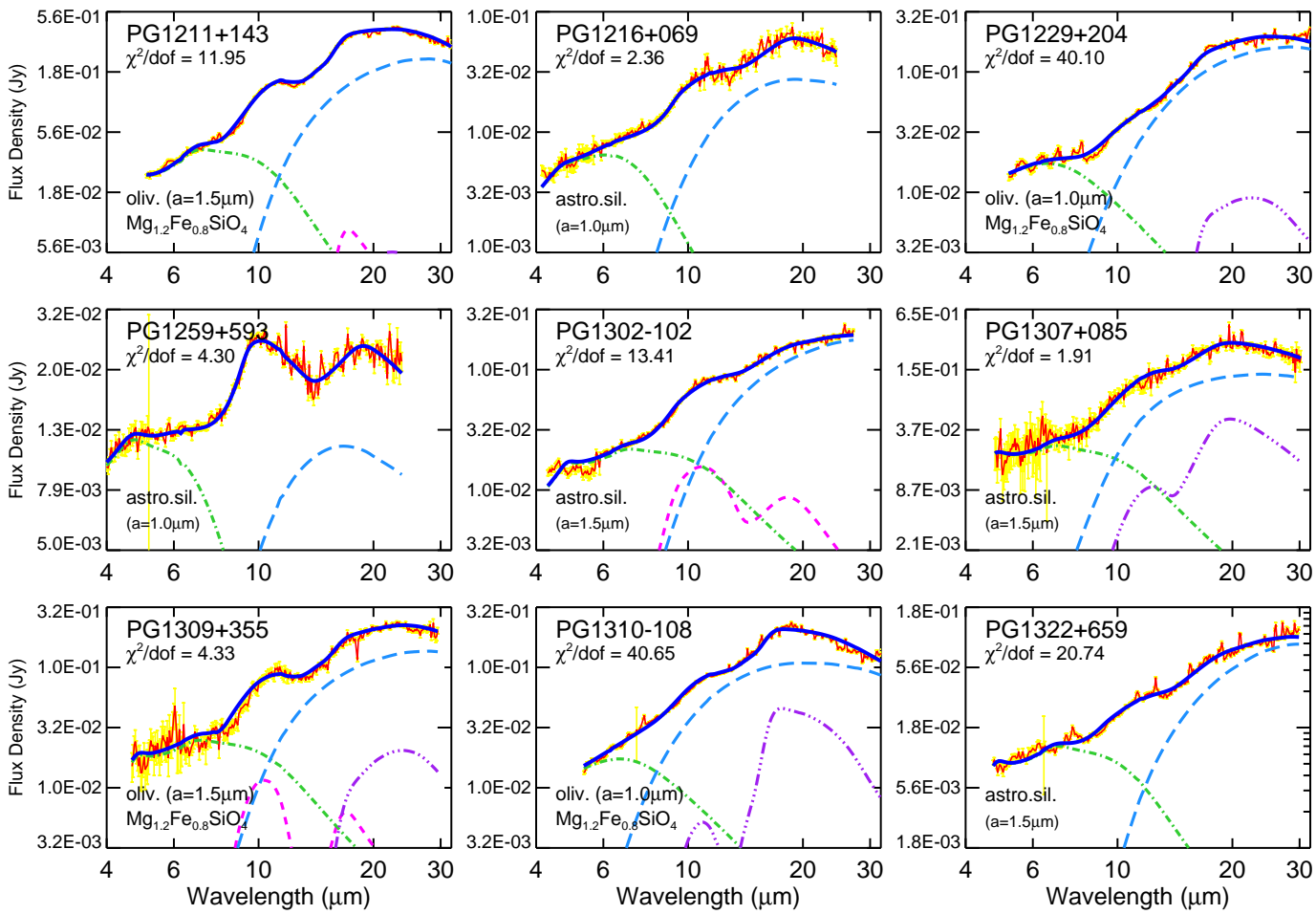


Fig. 1.— Continued, but for the PG quasars PG1211+143, PG1216+069, PG1229+204, PG1259+593, PG1302-102, PG1307+085, PG1309+355, PG1310-108, and PG1322+659.

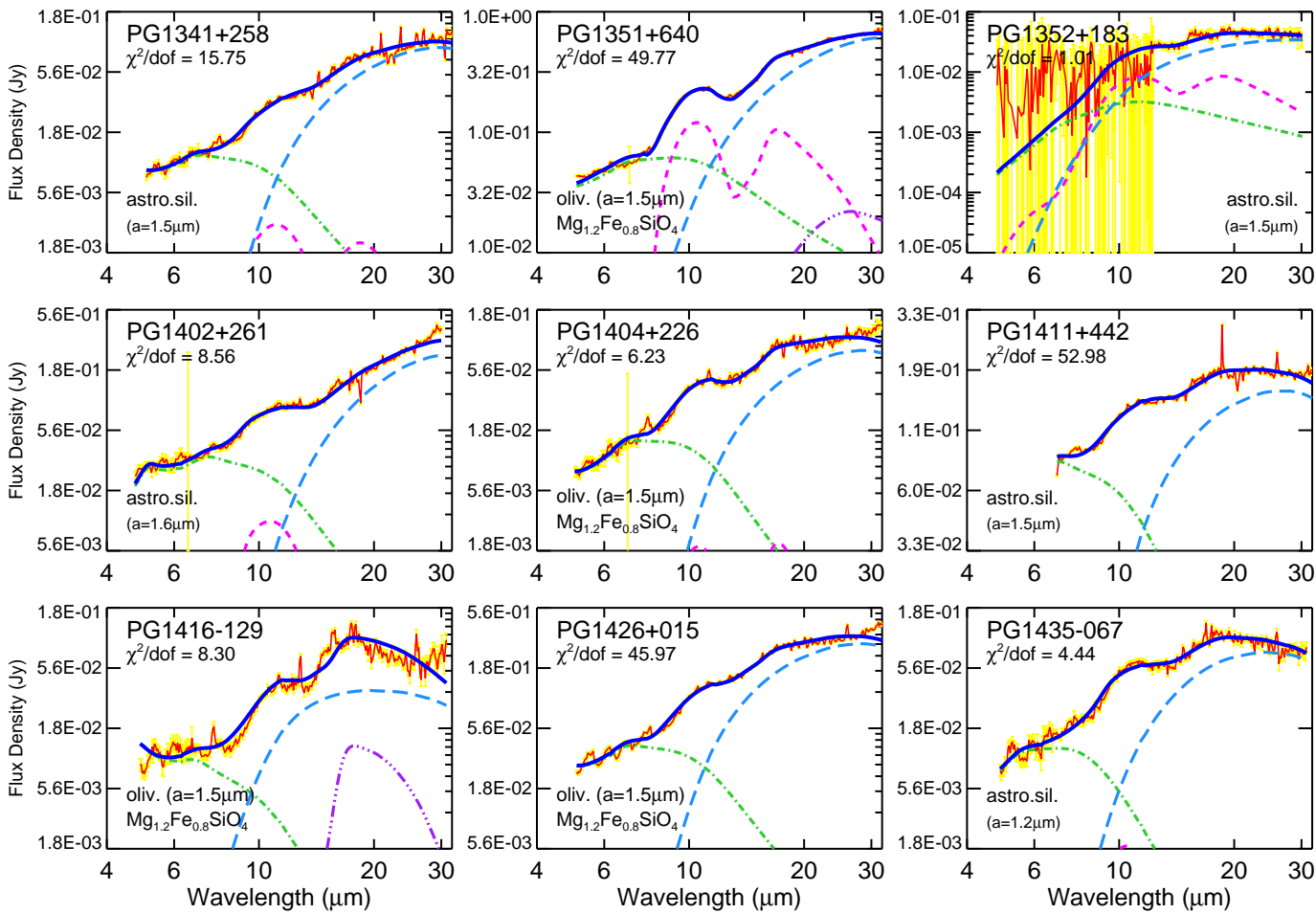


Fig. 1.— Continued, but for the PG quasars PG1341+258, PG1351+640, PG1402+261, PG1404+226, PG1411+442, PG1416-129, PG1426+015, and PG1435-067.

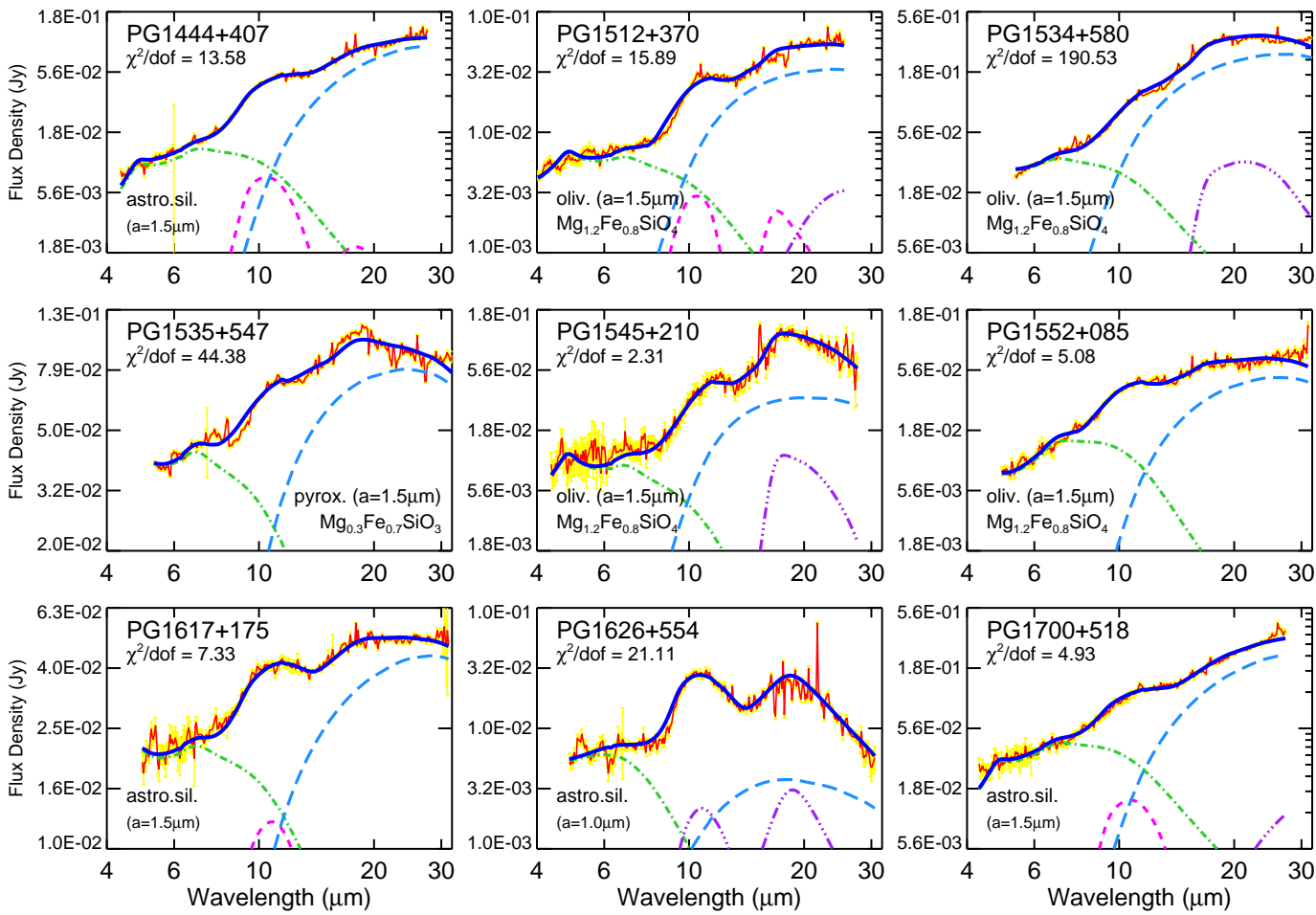


Fig. 1.— Continued, but for the PG quasars PG1444+407, PG1512+370, PG1534+580, PG1535+547, PG1545+210, PG1552+085, PG1617+175, PG1626+554, and PG1700+518.

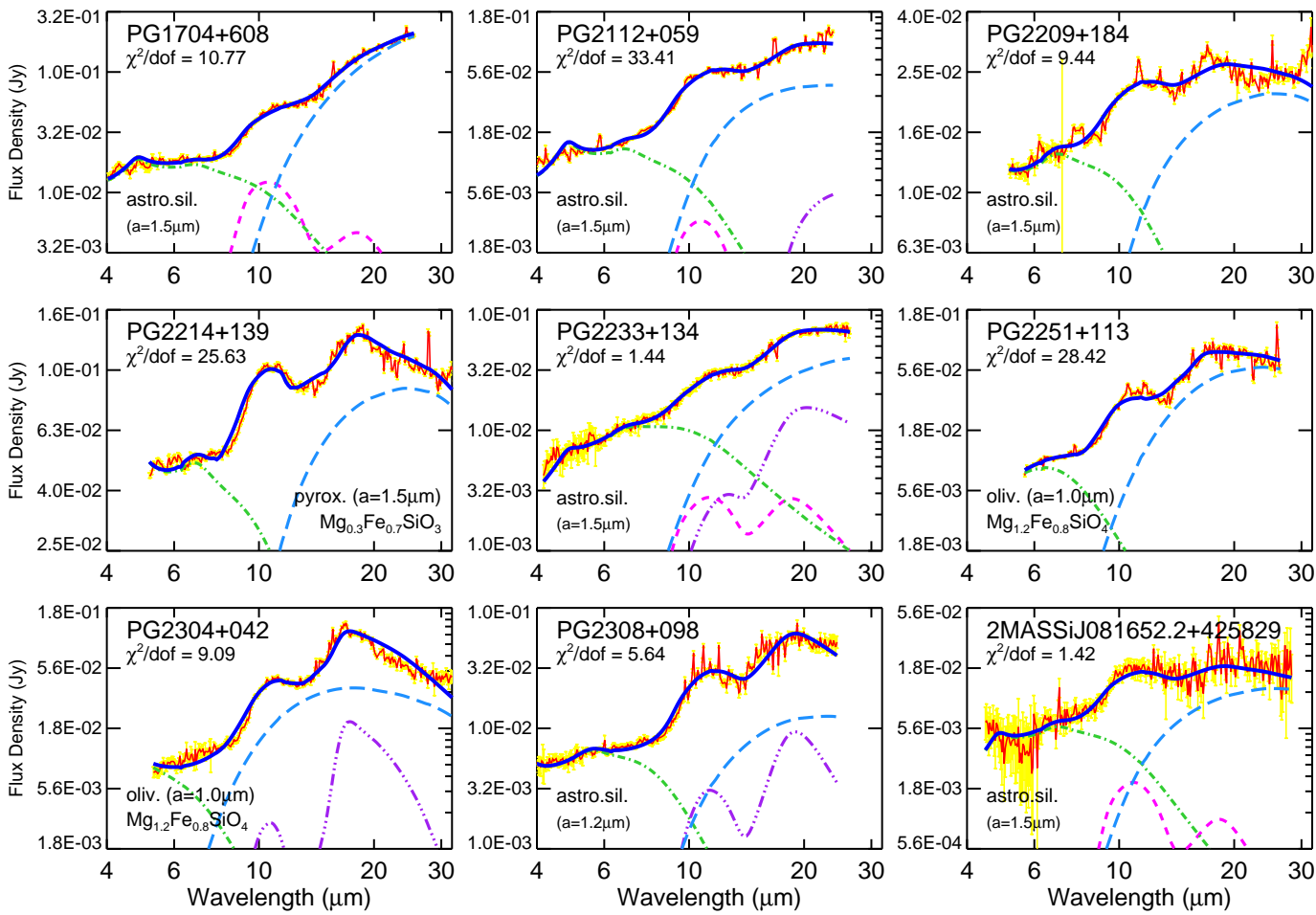


Fig. 1.— Continued, but for the PG quasars PG1704+608, PG2112+059, PG2209+184, PG2214+139, PG2233+134, PG2251+113, PG2304+042, PG2308+098 and the 2MASS quasar 2MASSJ081652.2+425829.

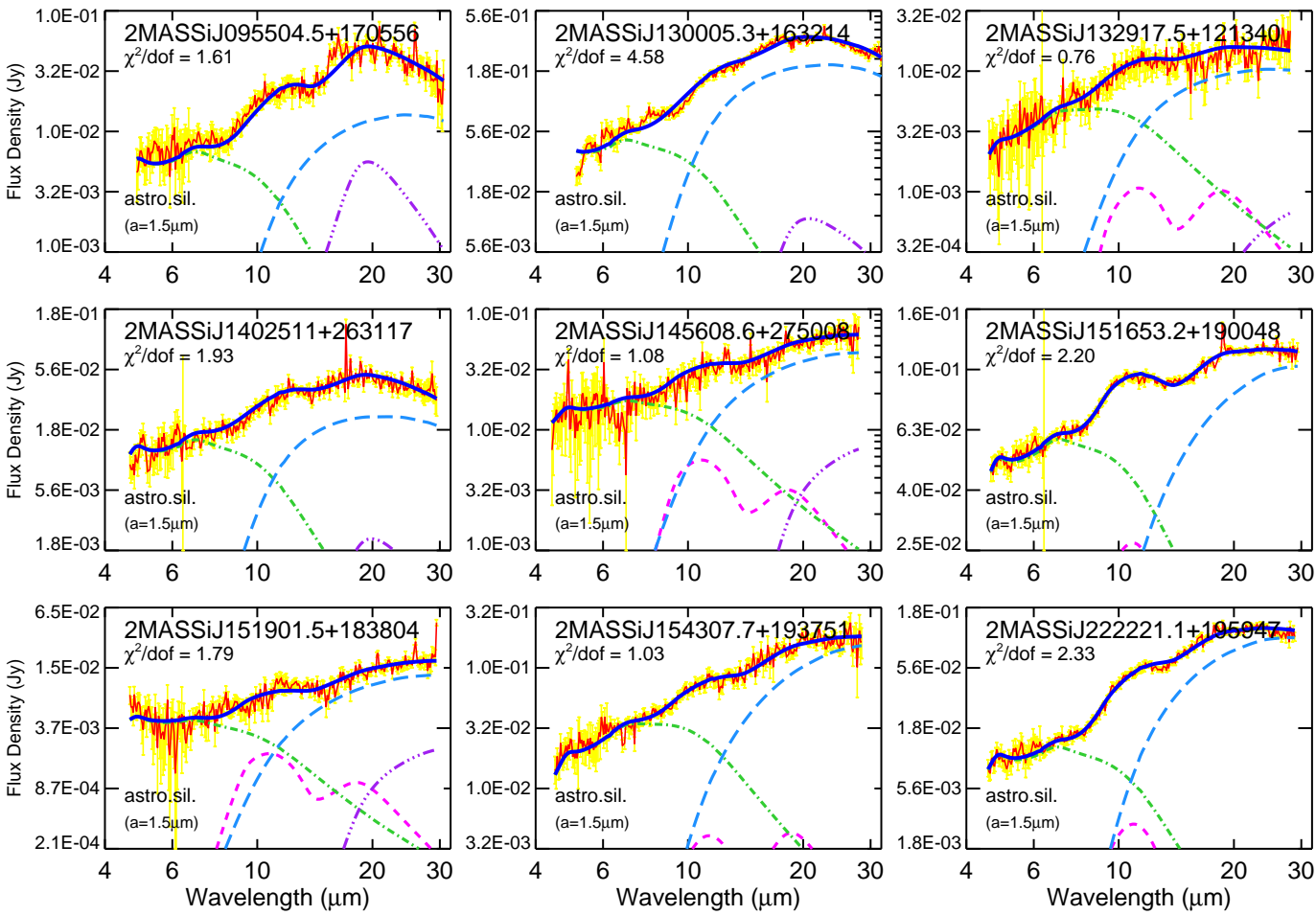


Fig. 1.— Continued, but for the 2MASS quasars 2MASSJ095504.5+170556, 2MASSJ130005.3+163214, 2MASSJ132917.5+121340, 2MASSJ140251.1+263117, 2MASSJ145608.6+275008, 2MASSJ151653.2+190048, 2MASSJ151901.5+183804, 2MASSJ154307.7+193751, and 2MASSJ222221.1+195947.

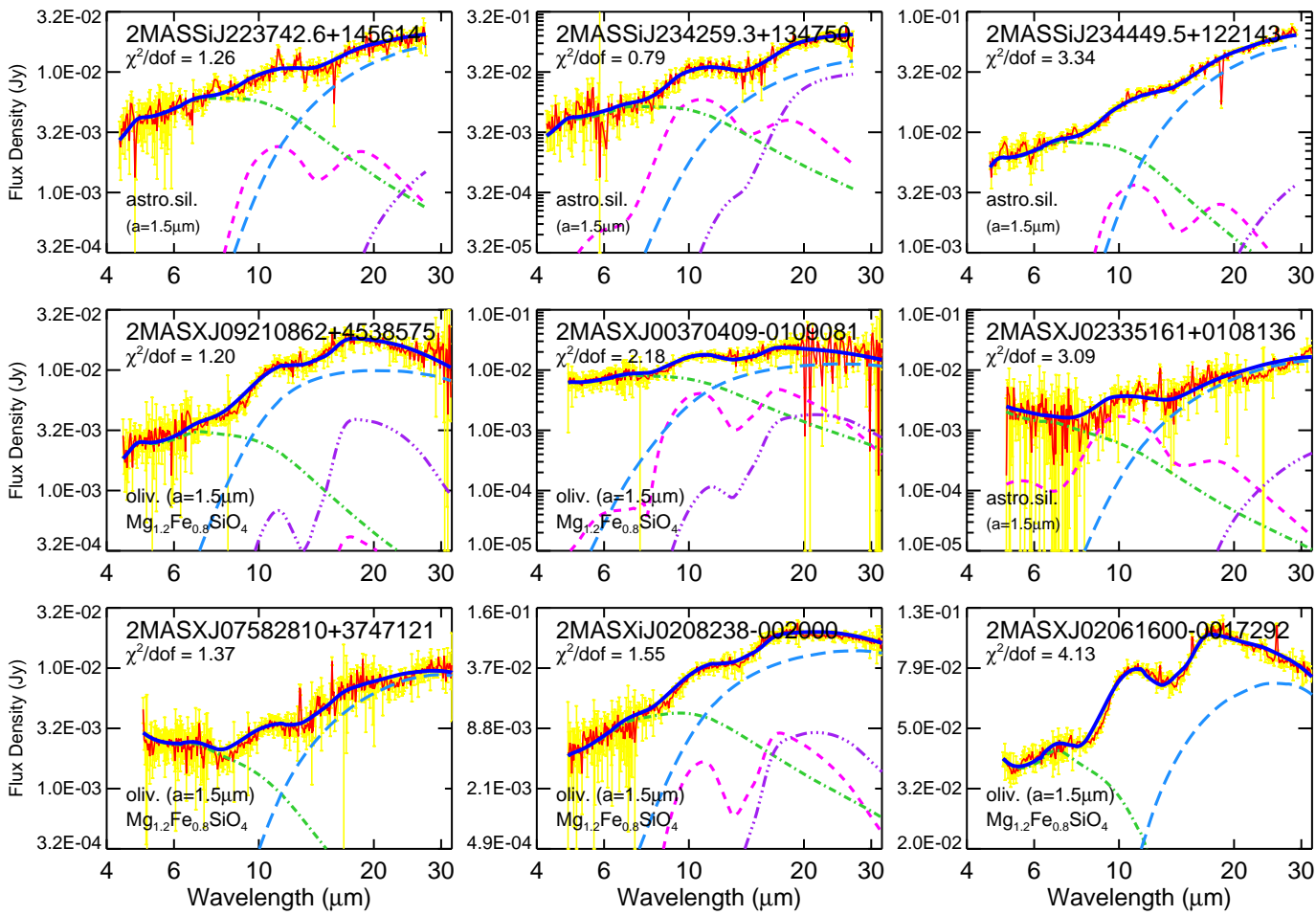


Fig. 1. — Continued, but for the 2MASS quasars 2MASSJ223742.6+145614, 2MASSJ234259.3+134750, 2MASSJ234449.5+122143 and the S³GA AGNs 2MASXJ09210862+4538575, 2MASXJ00370409-0109081, 2MASXJ02335161+0108136, 2MASXJ07582810+3747121, 2MASXiJ0208238-002000, and 2MASXJ02061600-0017292.

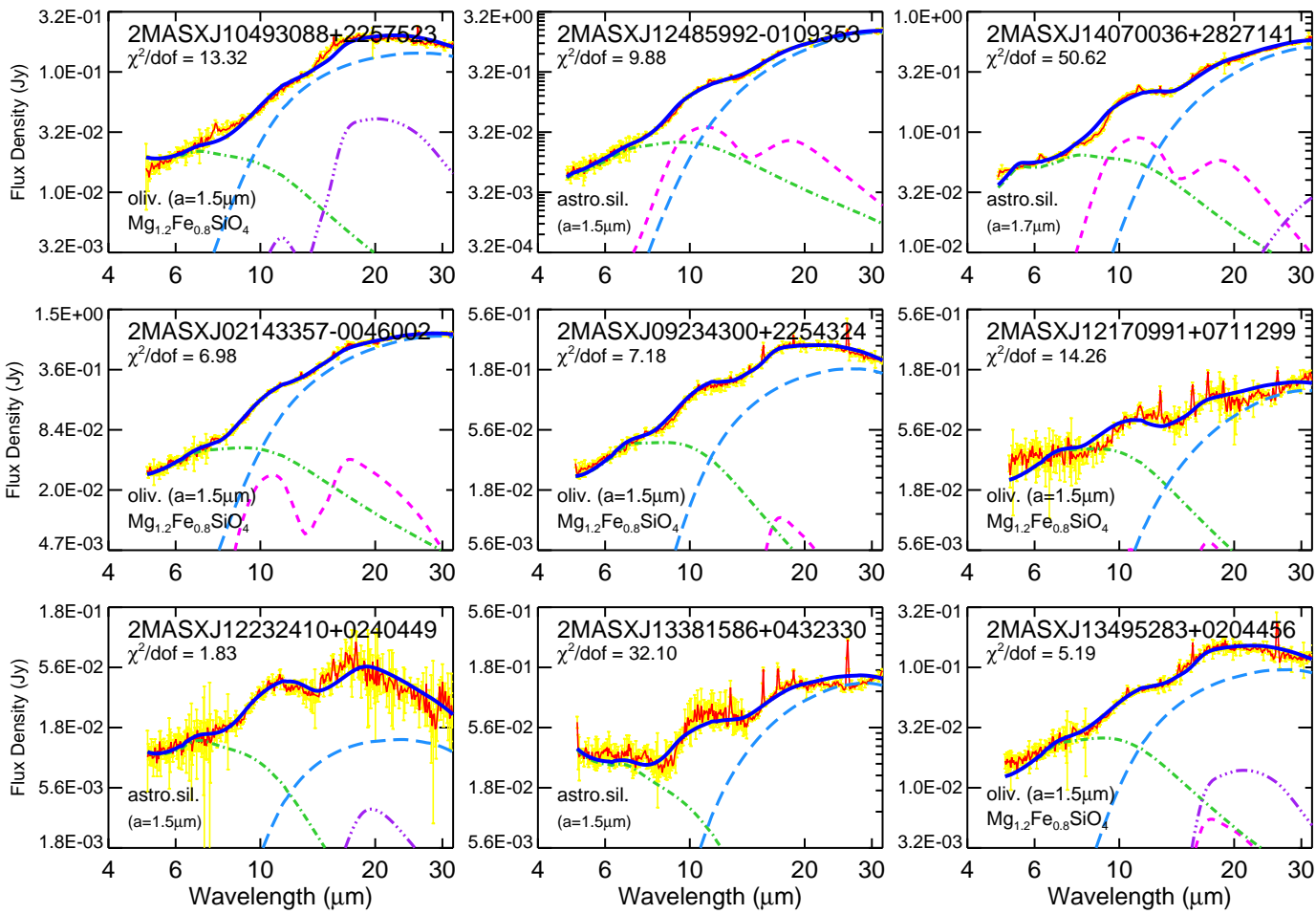


Fig. 1.— Continued, but for the S³AGN AGNs 2MASXJ10493088+2257523, 2MASXJ12485992-0109353, 2MASXJ14070036+2827141, 2MASXJ02143357-0046002, 2MASXJ09234300+2254324, 2MASXJ12170991+0711299, 2MASXJ12232410+0240449, 2MASXJ13381586+0432330, and 2MASXJ13495283+0204456.

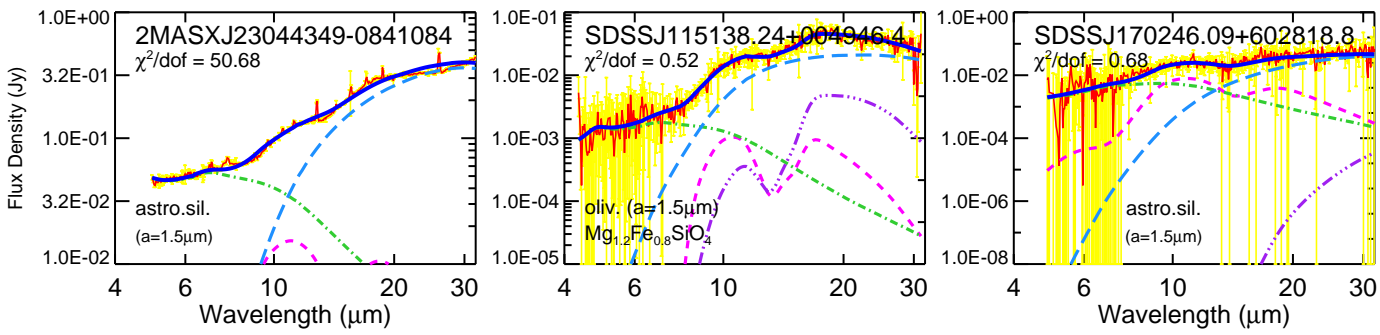


Fig. 1.— Continued, but for the S³AGN AGNs 2MASXJ23044349-0841084, SDSSJ115138.24+004946.4, and SDSSJ170246.09+602818.8.

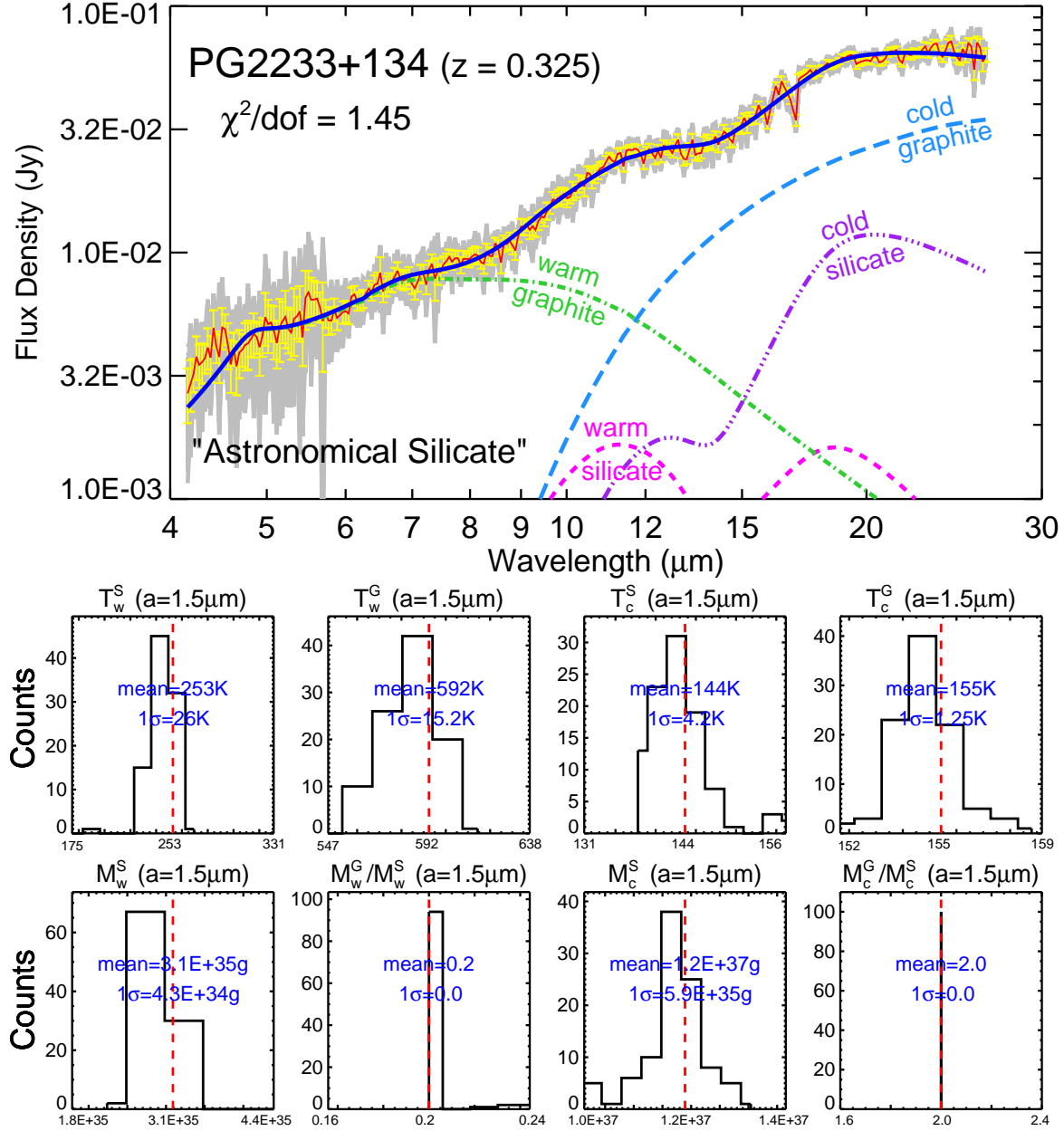


Fig. 2.— Estimating the uncertainties of the model parameters from Monte-Carlo simulation, with PG 2233+134 as an example. The top panel compares the *Spitzer*/IRS spectrum (red solid line) of PG 2233+134, as well as the observed 1σ error (yellow vertical lines) and the random spectrum generated from Monte-Carlo simulation (gray lines), with the model spectrum (blue solid line) which is the sum of warm silicate (magenta short dashed lines), cold silicate (purple dash-dot-dotted lines), warm graphite (green dash-dotted lines), and cold graphite (light blue long dashed lines). The middle panels show the distributions of the dust temperatures derived from 100 Monte-Carlo simulations for warm silicate, warm graphite, cold silicate and cold graphite. The bottom panels show the mass and mass-ratio distributions derived from 100 Monte-Carlo simulations for warm silicate or graphite, and cold silicate or graphite.

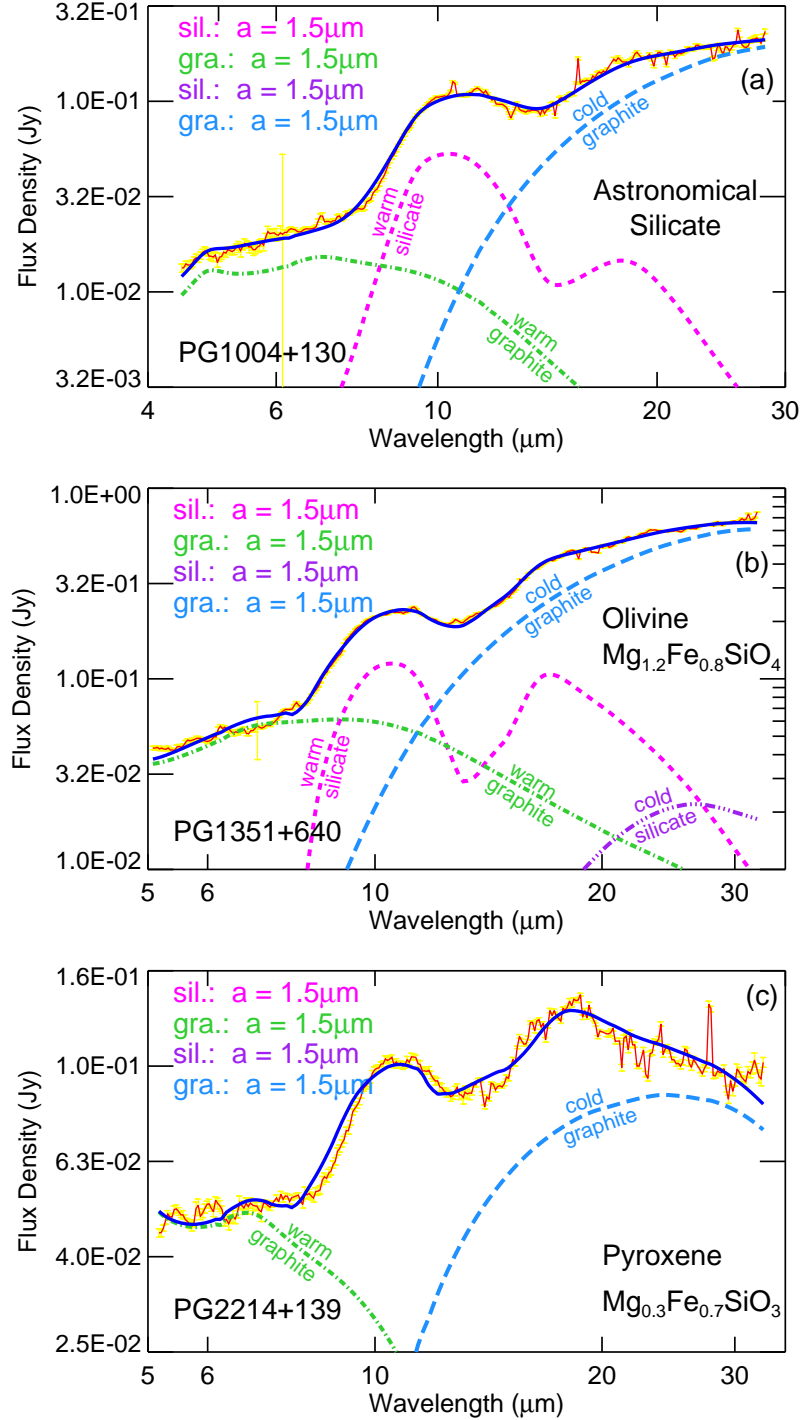


Fig. 3.— Illustrating the model fits to the *Spitzer*/IRS spectra of three PG quasars which require different silicate compositions: “astronomical silicate” for PG 1004+130 (a), olivine $\text{Mg}_{1.2}\text{Fe}_{0.8}\text{SiO}_4$ for PG 1351+640 (b), and pyroxene $\text{Mg}_{0.3}\text{Fe}_{0.7}\text{SiO}_3$ for PG 2214+139 (c). In each sub-figure, we plot the *Spitzer*/IRS spectrum (solid red line), the observed 1σ error (yellow vertical lines), the model spectrum (blue solid line) and the four fitting components: warm silicate (magenta short dashed line), cold silicate (purple dash-dot-dotted line), warm graphite (green dash-dotted line), and cold graphite (light blue long dashed line).

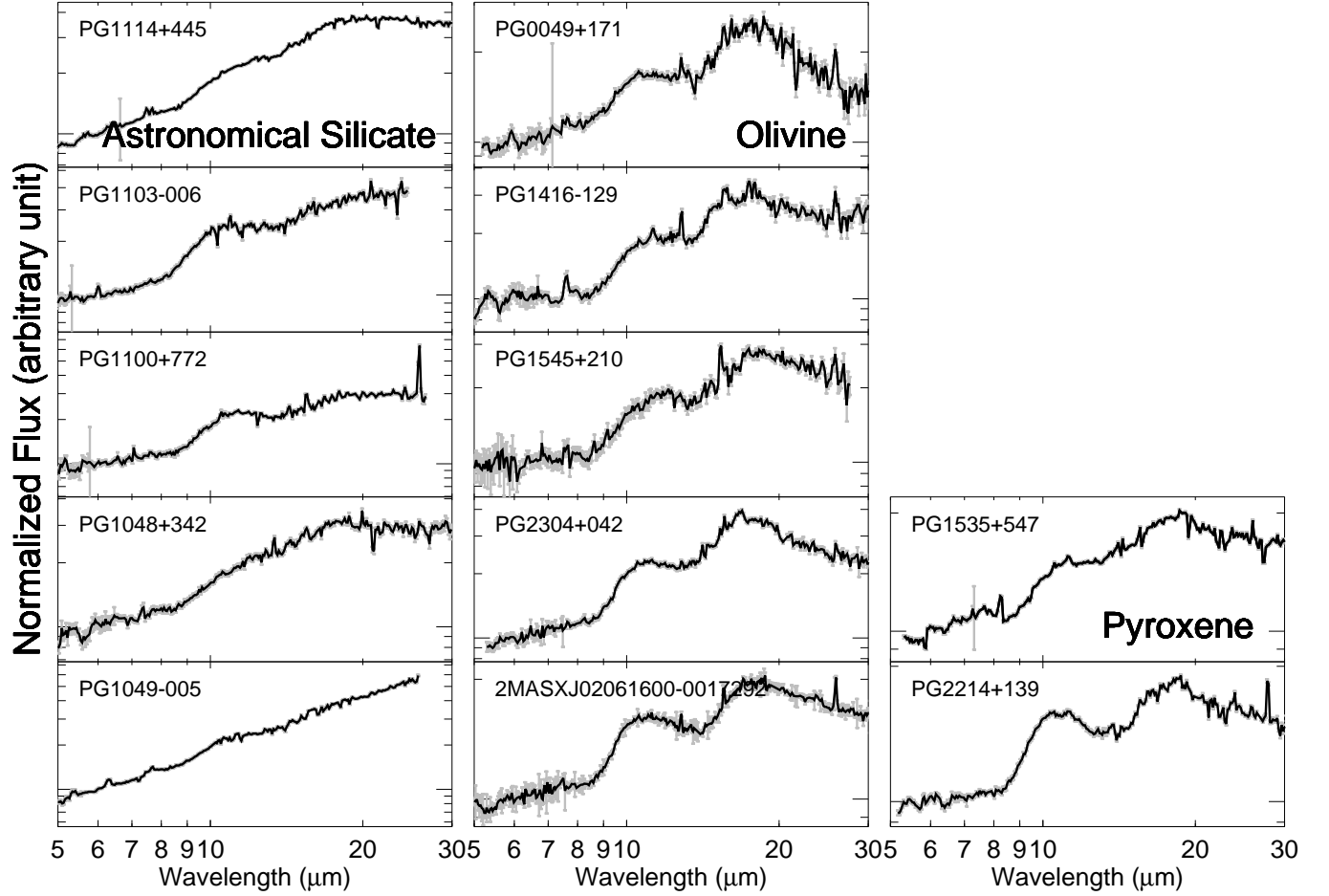
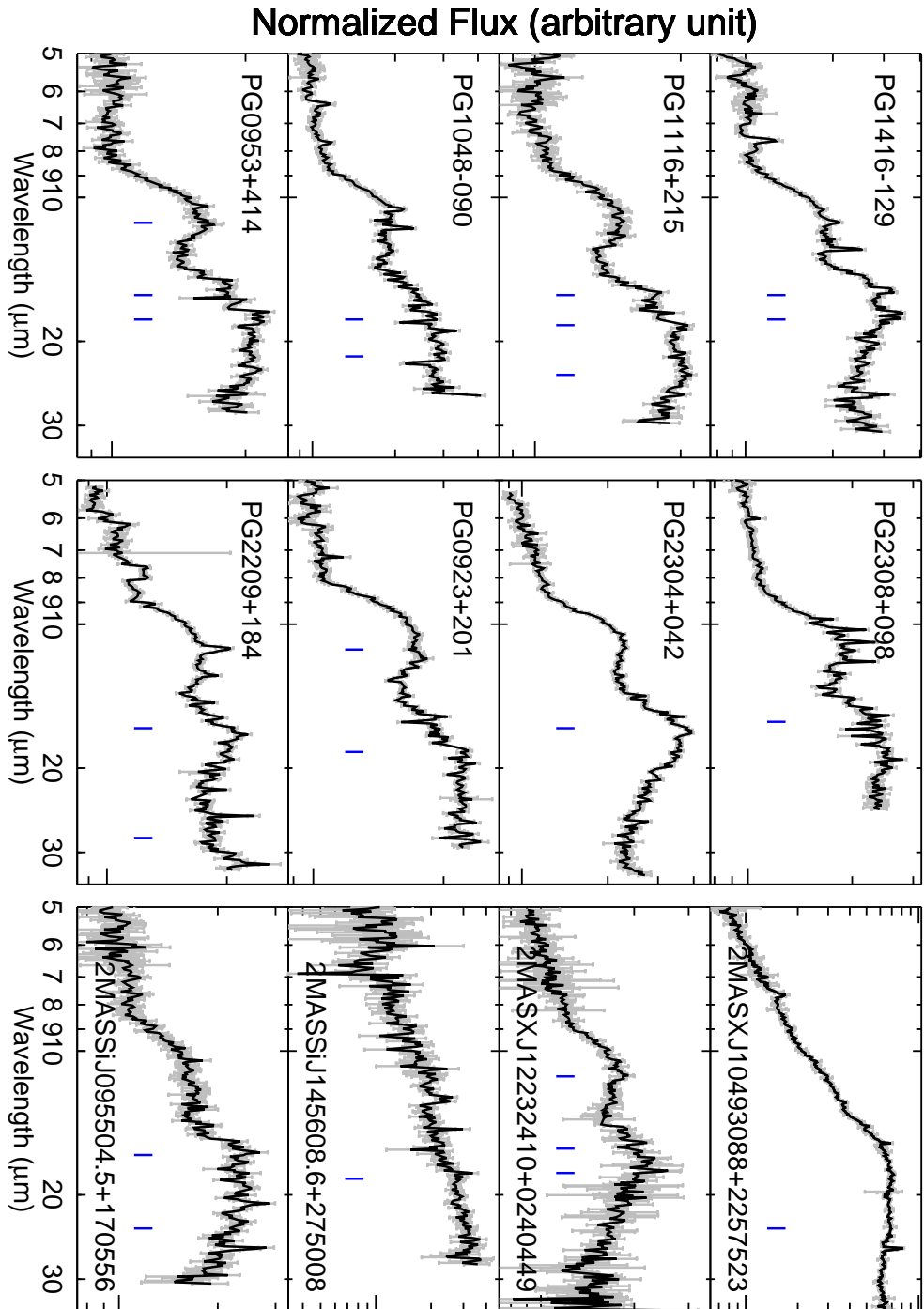


Fig. 4.— Illustrations of the *Spitzer*/IRS spectra of those AGNs for which the best fits favor “astronomical silicate” (left), amorphous olivine (middle), and amorphous pyroxene (right).

Fig. 5. — *Spitzer*/IRS spectra of those sources which exhibit crystalline silicate emission features.



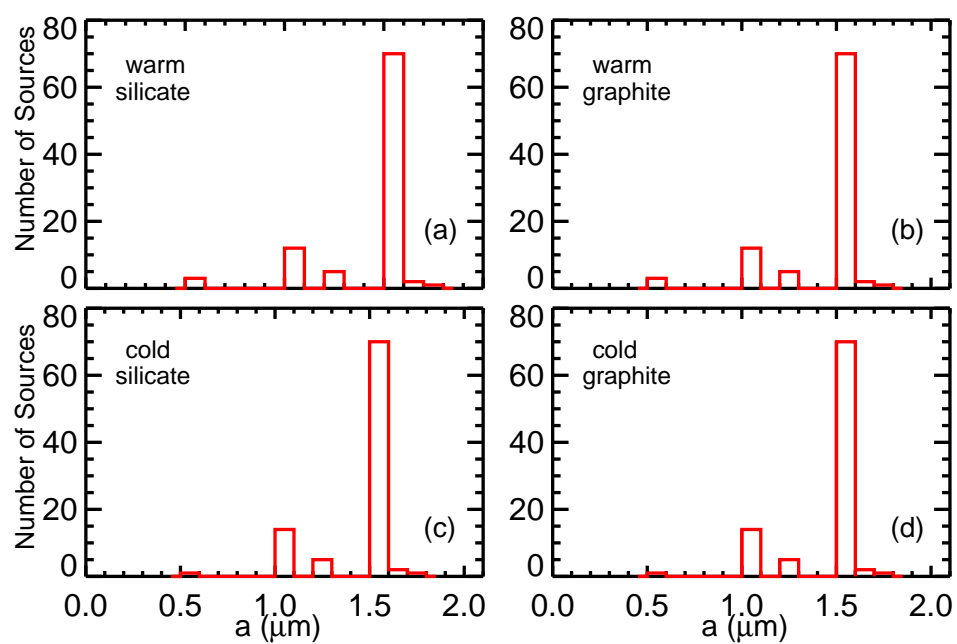


Fig. 6.— Histogram of the sizes of (a) the warm silicate component, (b) the warm graphite component, (c) the cold silicate component, and (d) the cold graphite component derived for 93 sources which exhibit the 9.7 and 18 μm silicate emission features.

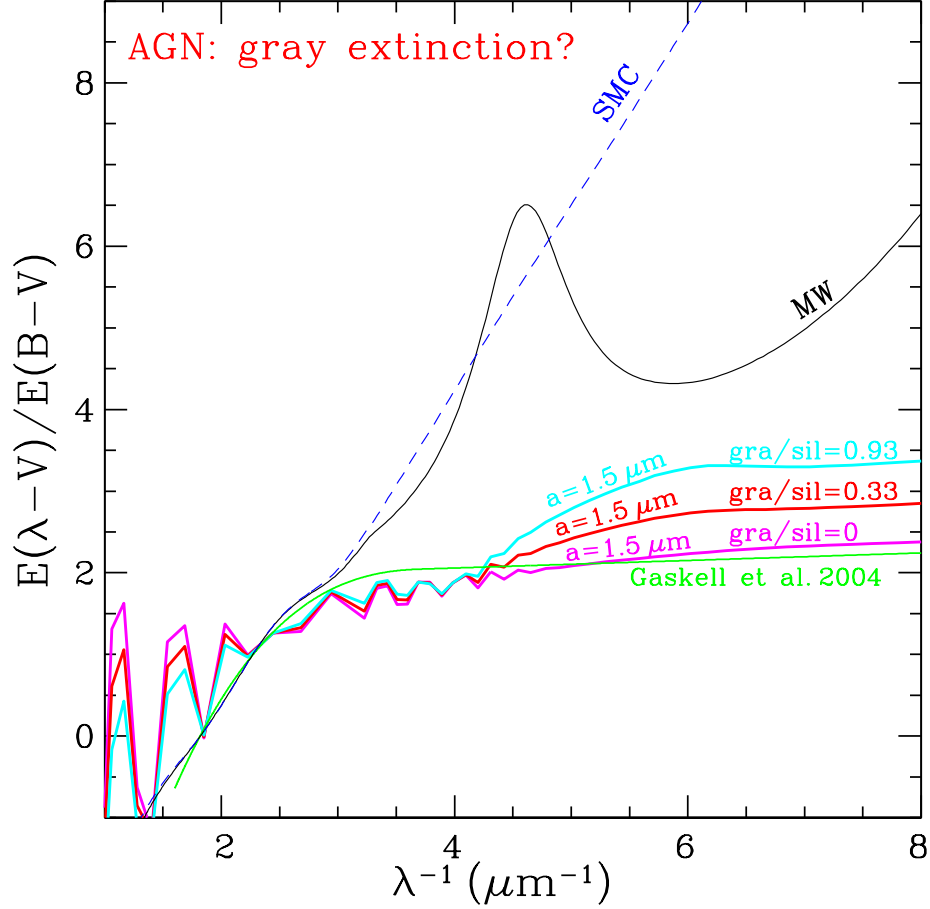


Fig. 7.— Comparison of the extinction curves of the Milky Way (black solid line) and the SMC (blue dashed line) with that of Gaskell et al. (2004) derived from composite quasar spectra (green solid line) and that calculated from spherical silicate and graphite grains of radii $a = 1.5 \mu\text{m}$ with a mass mixing ratio of $M_{\text{carb}}/M_{\text{sil}} = 0$ (magenta solid line), $M_{\text{carb}}/M_{\text{sil}} = 0.33$ (red solid line), and $M_{\text{carb}}/M_{\text{sil}} = 0.93$ (cyan solid line). The sawtooth-like structures seen in the calculated extinction curves at $\lambda^{-1} < 2.5 \mu\text{m}^{-1}$ will be smoothed out if a distribution of grain sizes is considered. Note that at $\lambda^{-1} > 2.5 \mu\text{m}^{-1}$ the extinction curve of spherical silicate dust of radii $a = 1.5 \mu\text{m}$ (magenta solid line) closely agrees with the AGN extinction curve of Gaskell et al. (2004).

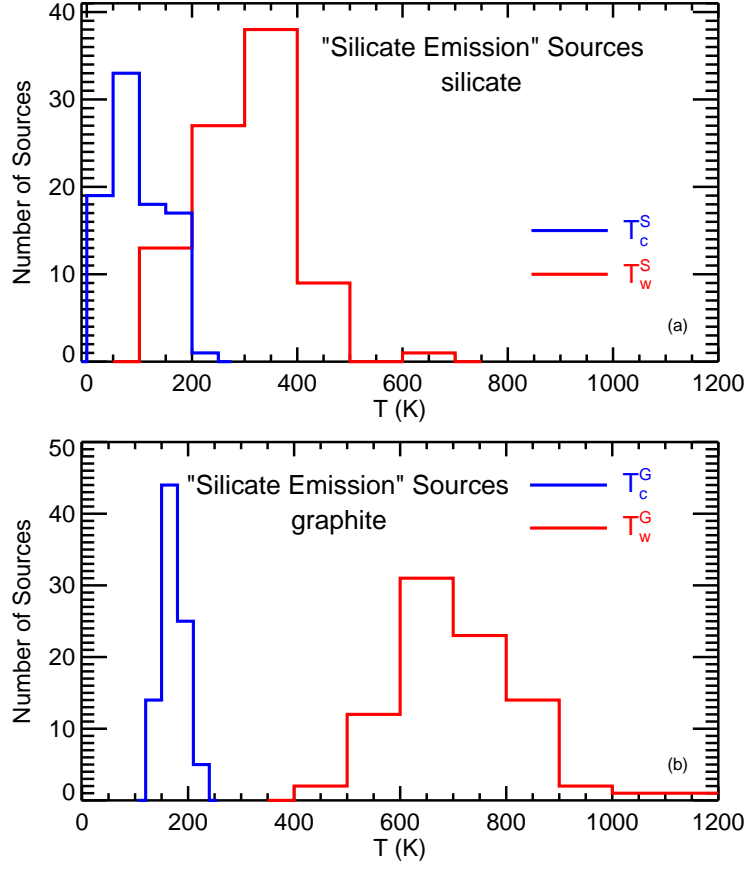


Fig. 8.— Histograms of dust temperatures of the warm silicate component (red line in upper panel), the cold silicate component (blue line in upper panel), the warm graphite component (red line in bottom panel), and the cold graphite component (blue line in bottom panel) derived for 93 sources which exhibit the 9.7 and $18\,\mu\text{m}$ silicate emission features.

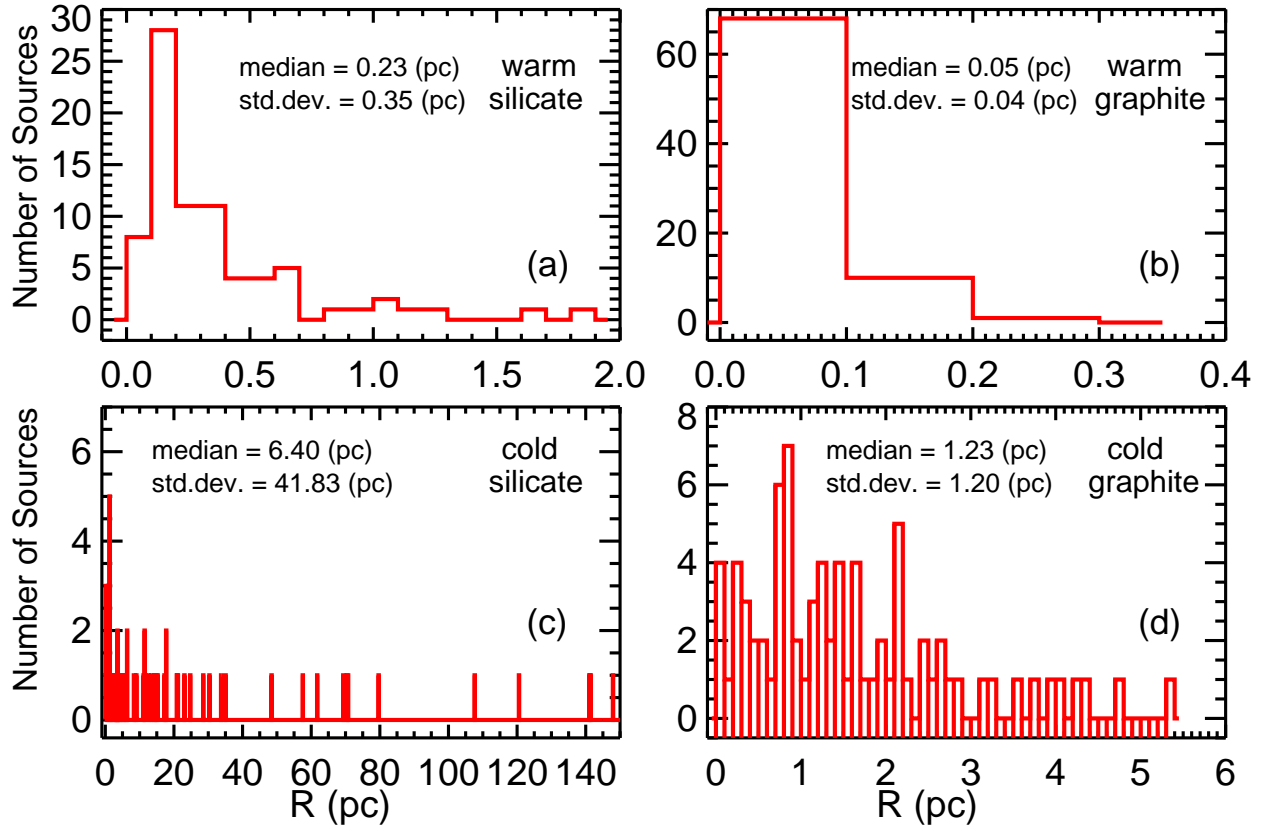


Fig. 9.— Histograms of the distances of the dust from the central engine for those 93 “silicate emission” sources: warm silicate (a), warm graphite (b), cold silicate (c), and cold graphite (d).

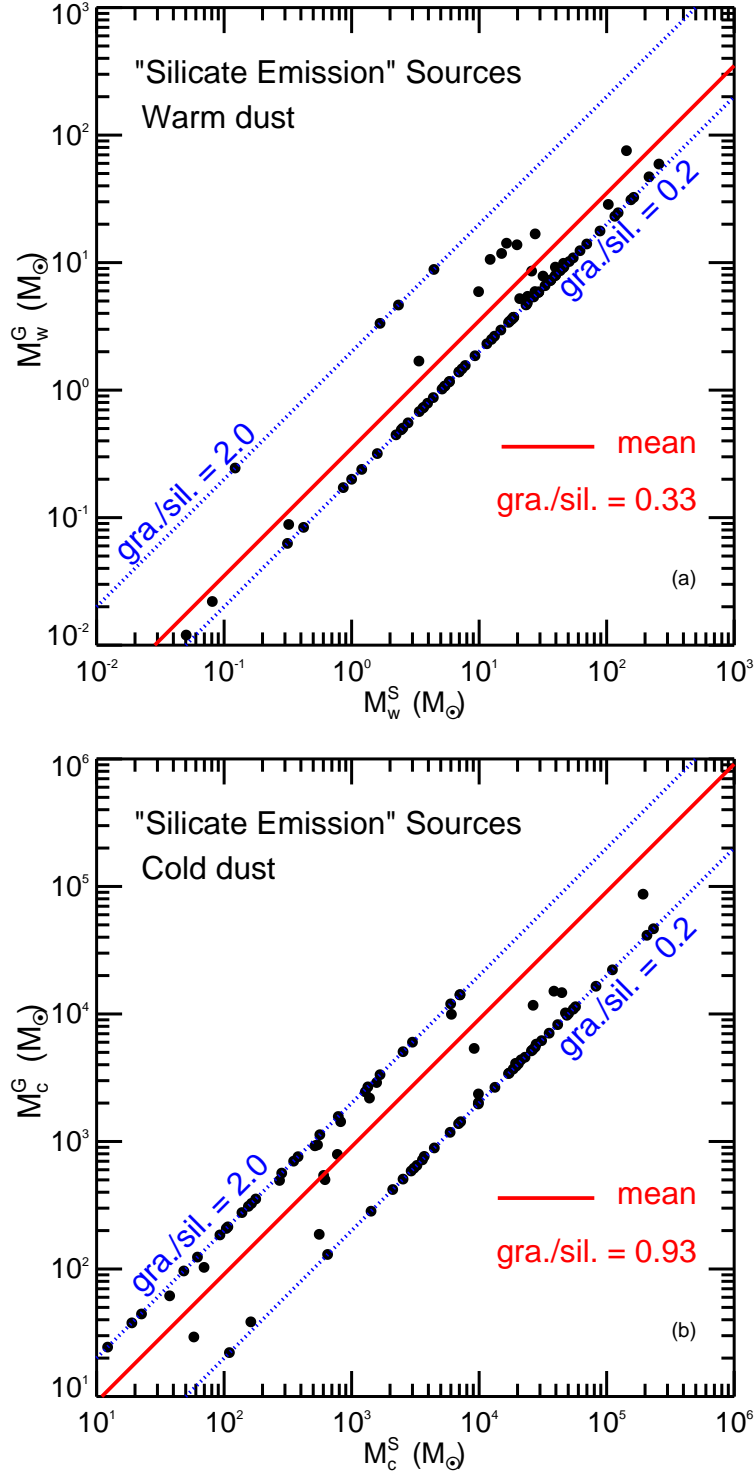


Fig. 10.— Dust mass ratios of warm graphite to warm silicate (M_w^G/M_w^S ; upper panel) and of cold graphite to cold silicate (M_c^G/M_c^S ; bottom panel) derived for those 93 “silicate emission” sources. The blue dotted lines show the upper ($M_c^G/M_c^S = 2.0$) and lower ($M_c^G/M_c^S = 0.2$) boundaries. The red solid lines show the mean mass ratios derived from our model.

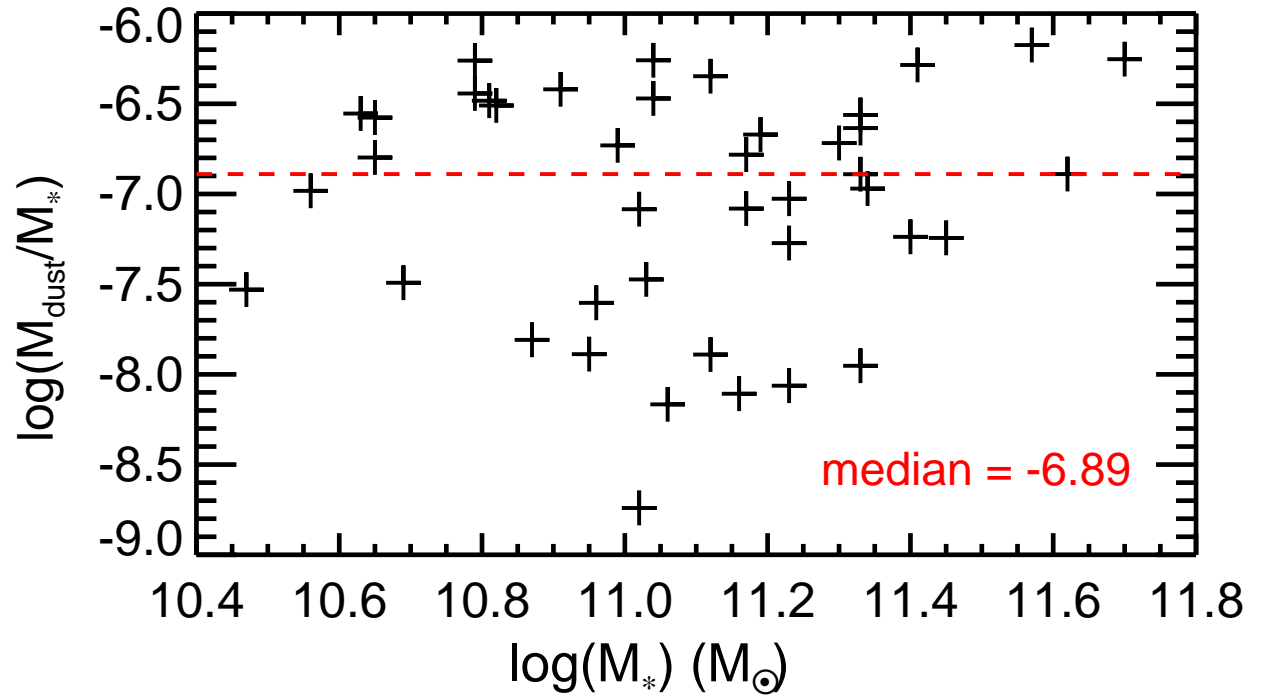


Fig. 11.— Comparison of the stellar mass (M_*) of the host galaxies of 39 PG quasars and two *2MASS* quasars with the total dust mass (M_{dust}) obtained by summing over all four dust components (i.e., $M_{\text{dust}} = M_{\text{w}}^{\text{S}} + M_{\text{c}}^{\text{S}} + M_{\text{w}}^{\text{G}} + M_{\text{c}}^{\text{G}}$). The horizontal dashed line plots the median ratio of $\langle M_{\text{dust}}/M_* \rangle \approx 1.3 \times 10^{-7}$.

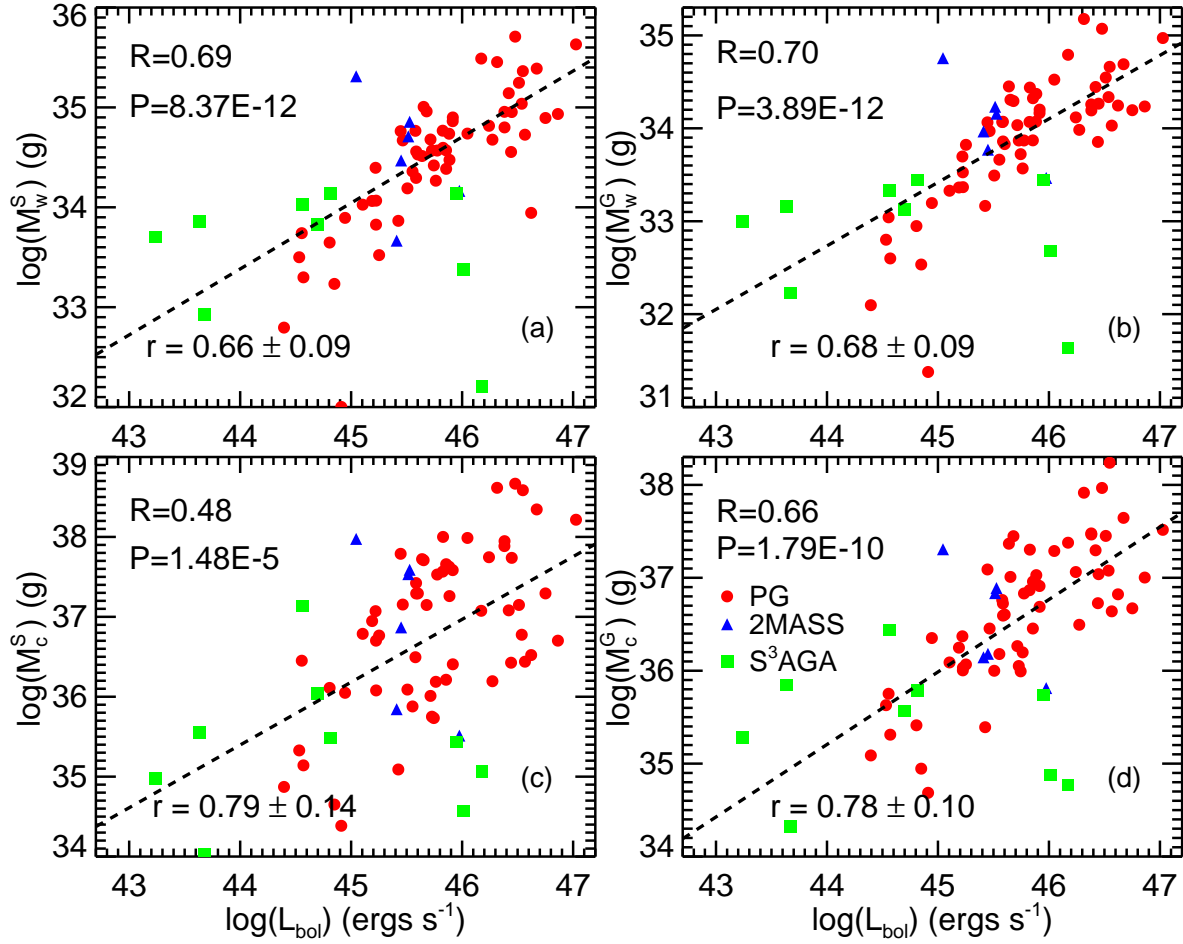


Fig. 12.— Correlation of the bolometric luminosity L_{bol} [approximated by $7 \times \lambda L_{\lambda}(5100 \text{ \AA})$] with the mass of the warm silicate component (M_w^S ; a), the warm graphite component (M_w^G ; b), the cold silicate component (M_c^S ; c), and the cold graphite component (M_c^G ; d). In each panel, the PG quasars are shown as red circles, the 2MASS quasars are shown as blue triangles, and the S³AGA AGNs are shown as green squares. Also labeled in each panel are the Pearson correlation coefficient (R) and the probability (P) of no correlation as well as the slope of the linear relation (dashed lines).

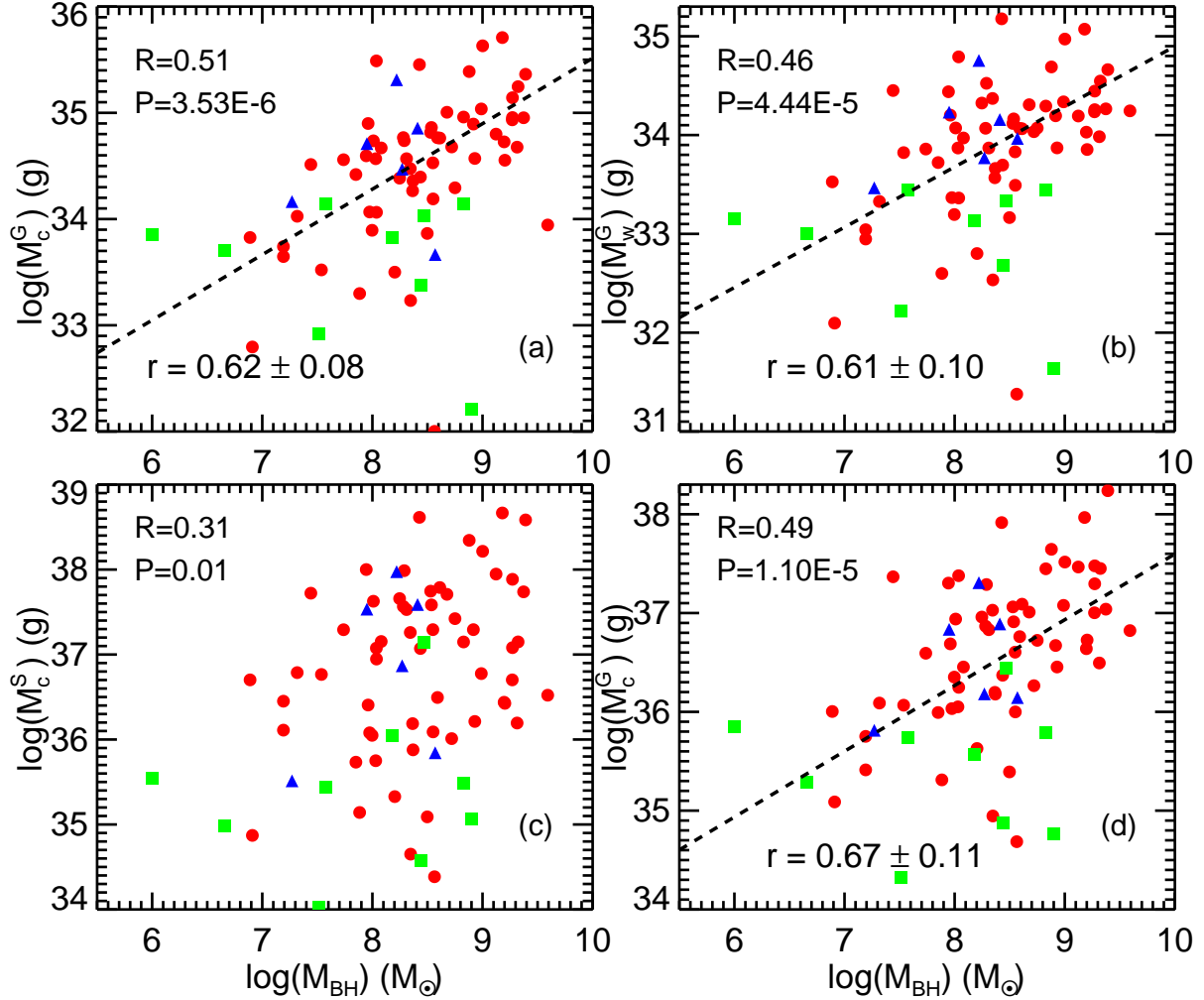


Fig. 13.— Correlation of the black hole mass (M_{BH}) with the mass of warm silicate (M_w^S ; a), warm graphite (M_w^G ; b), cold silicate (M_c^S ; c), and cold graphite (M_c^G ; d). In each panel, the PG quasars are shown as red circles, the 2MASS quasars are shown as blue triangles, and the S³AGN AGNs are shown as green squares. The Pearson correlation coefficient (R) and the probability (P) of no correlation as well as the slope of the linear relation are also labeled in each panel.

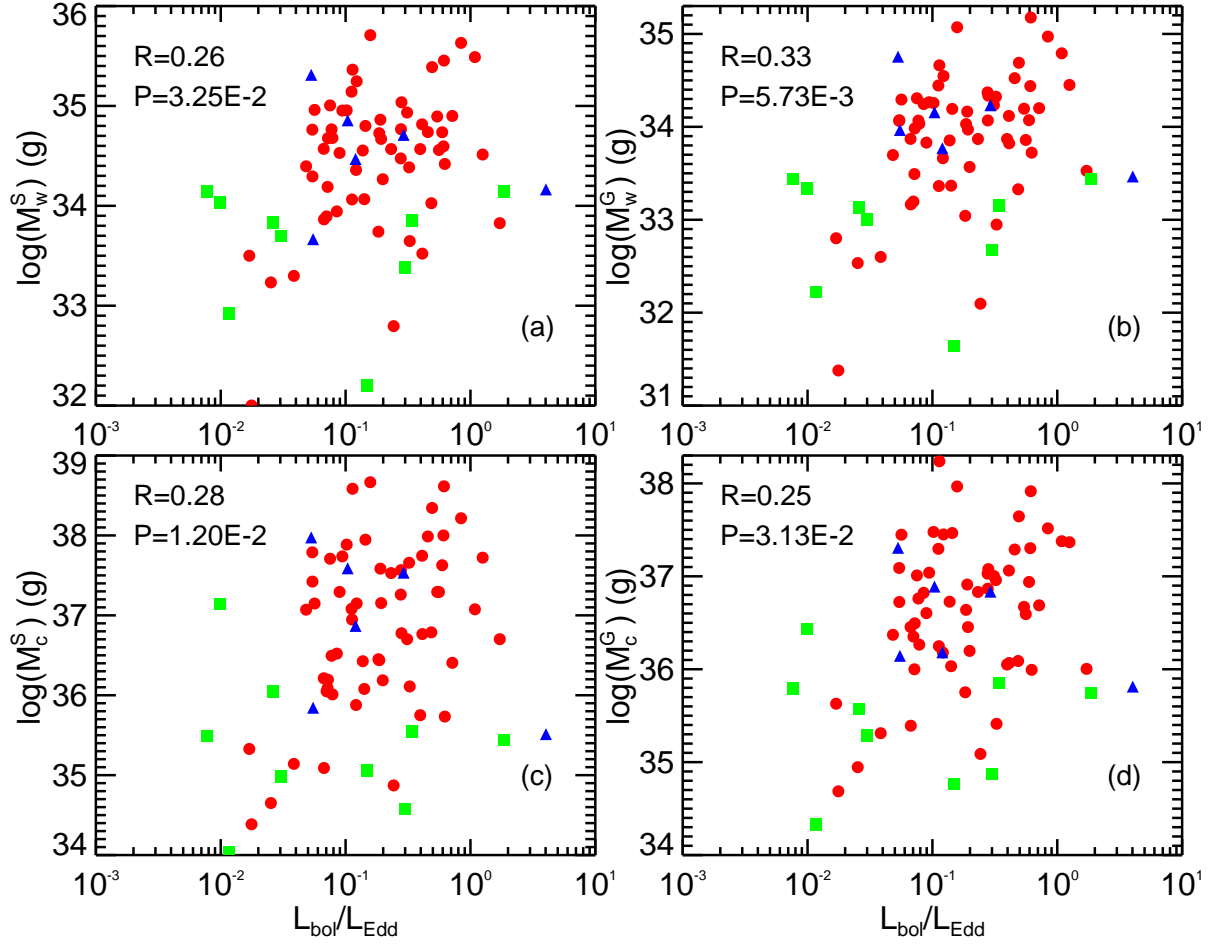


Fig. 14.— Correlation of the Eddington ratio (represented by $L_{\text{bol}}/L_{\text{Edd}}$) with the mass of warm silicate (M_w^S ; a), warm graphite (M_w^G ; b), cold silicate (M_c^S ; c), and cold graphite (M_c^G ; d). In each panel, the PG quasars are shown as red circles, the 2MASS quasars are shown as blue triangles, and the S³ AGNs are shown as green squares.

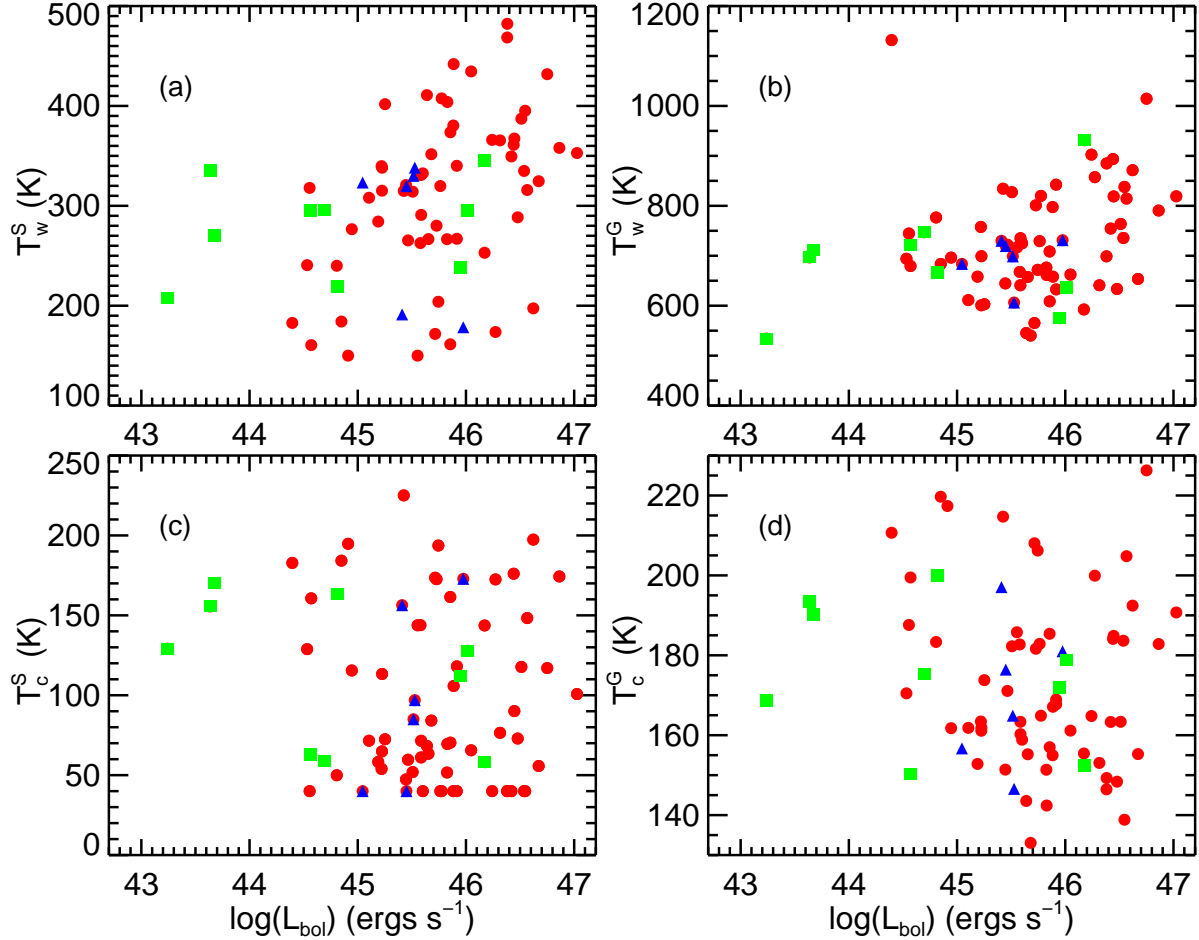


Fig. 15.— Correlation of the bolometric luminosity with the temperature of the warm silicate component (T_w^S ; a), the warm graphite component (T_w^G ; b), the cold silicate component (T_c^S ; c), and the cold graphite component (T_c^G ; d). In each panel, the PG quasars are shown as red circles, the *2MASS* quasars are shown as blue triangles, and the S³AGN AGNs are shown as green squares.

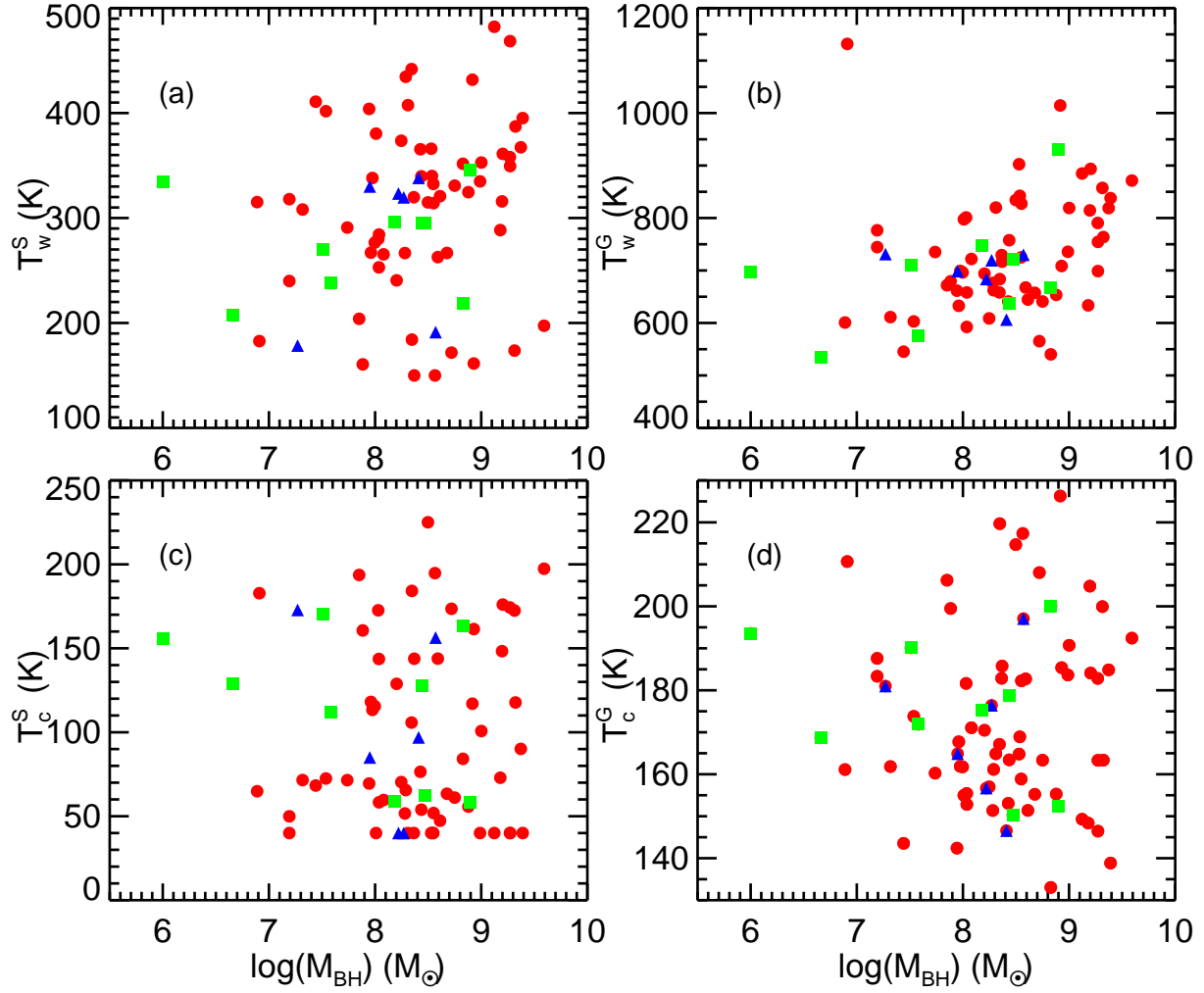


Fig. 16.— Correlation of the black hole mass (M_{BH}) with the temperature of warm silicate (T_{w}^{S} ; a), warm graphite (T_{w}^{G} ; b), cold silicate (T_{c}^{S} ; c), and cold graphite (T_{c}^{G} ; d). In each panel, the PG quasars are shown as red circles, the *2MASS* quasars are shown as blue triangles, and the *S*³AGN AGNs are shown as green squares.

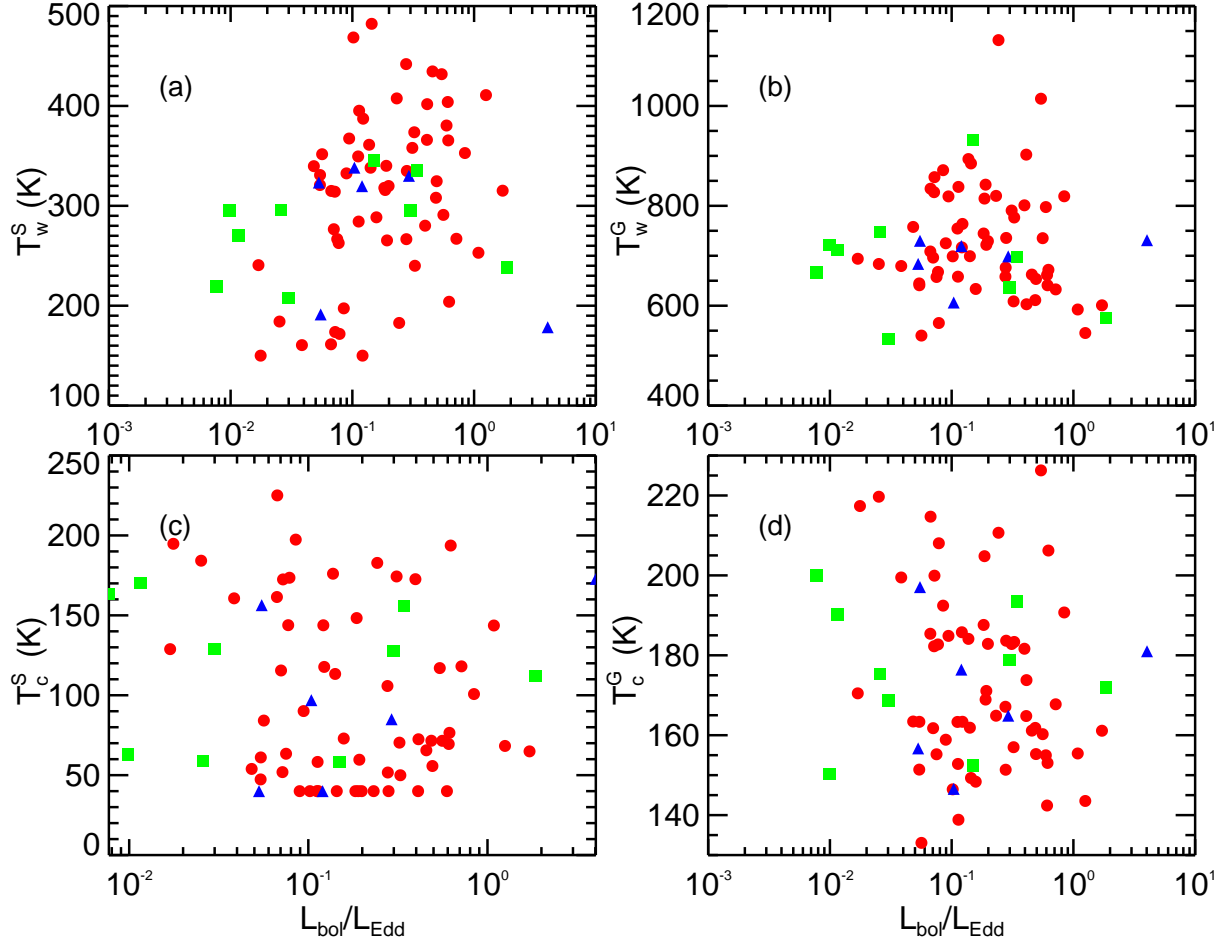


Fig. 17.— Correlation of the Eddington ratio $L_{\text{bol}}/L_{\text{Edd}}$ with the temperature of warm silicate (T_w^S ; a), warm graphite (T_w^G ; b), cold silicate (T_c^S ; c), and cold graphite (T_c^G ; d). In each panel, the PG quasars are shown as red circles, the 2MASS quasars are shown as blue triangles, and the S³AGN AGNs are shown as green squares.

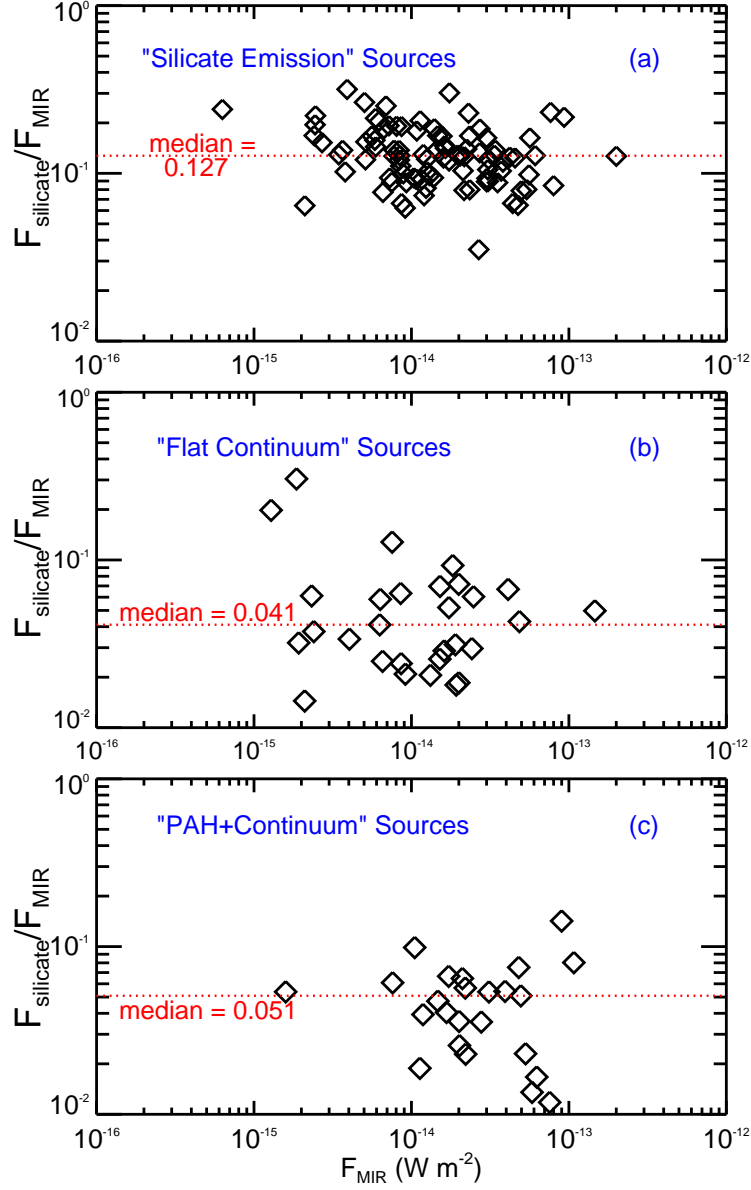


Fig. 18.— Fractional fluxes emitted in the 9.7 and $18\mu\text{m}$ silicate features (F_{silicate}) relative to the total mid-IR emission at $\sim 5\text{--}38\mu\text{m}$ (F_{MIR}) for the “silicate emission” sources (a), the “flat continuum” sources (b), and the “PAH + continuum” sources (c). For the latter two classes of sources, F_{silicate} is actually an upper limit. The dashed horizontal line shows the mean fraction $\langle F_{\text{silicate}}/F_{\text{MIR}} \rangle$.

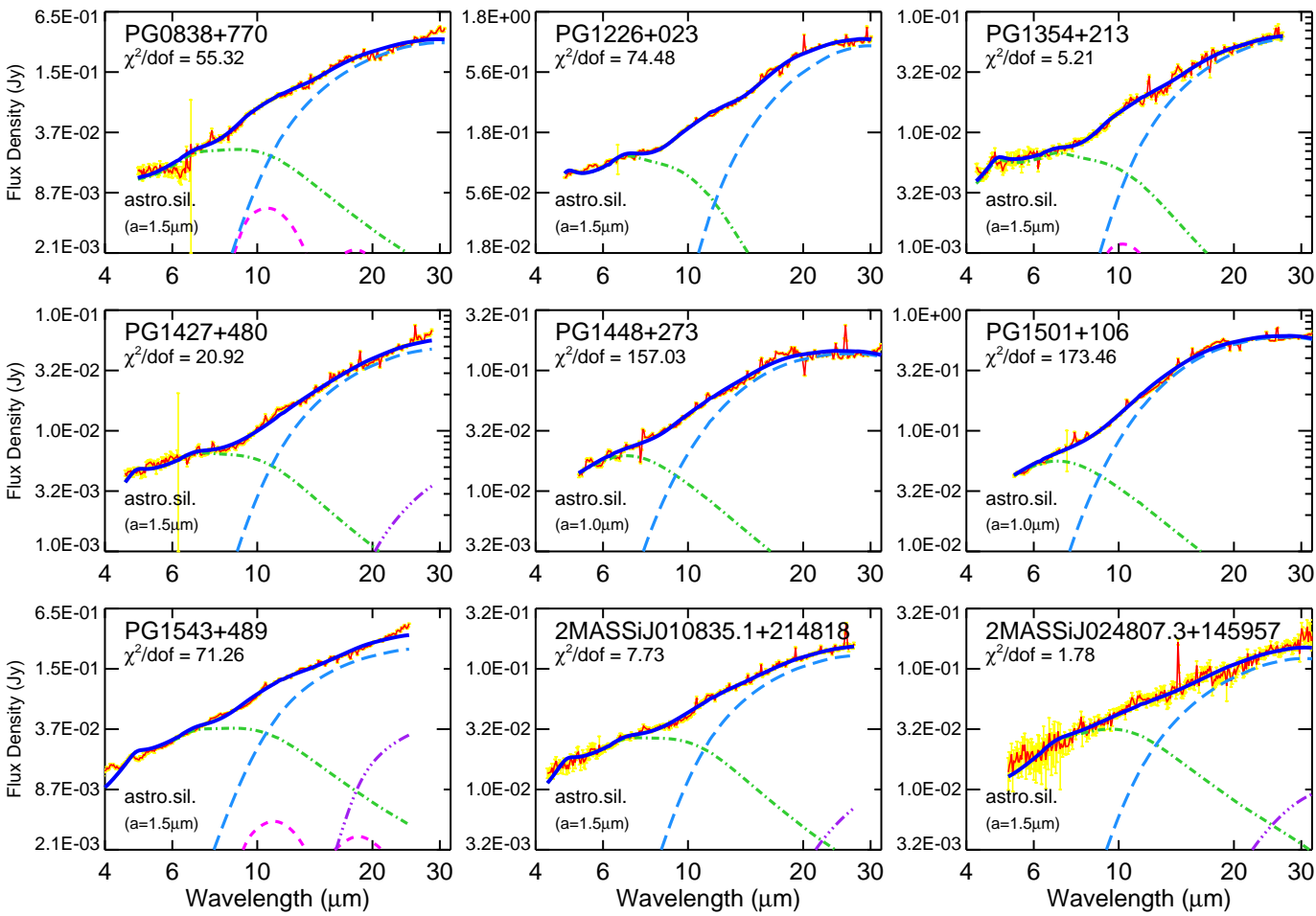


Fig. 19.— Comparison of the *Spitzer*/IRS spectra (red solid lines) of the PG quasars PG0838+770, PG1226+023, PG1354+213, PG1427+480, PG1448+273, PG1501+106, PG1543+489 and the 2MASS quasars 2MASSJ010835.1+214818 and 2MASSJ024807.3+145957 which show a featureless thermal continuum with the model spectra (blue solid lines) which are the sum of warm silicate (magenta short dashed lines), cold silicate (purple dash-dot-dotted lines), warm graphitic (green dash-dotted lines), and cold graphitic (light blue long dashed lines). Also shown are the observed 1σ errors (yellow vertical lines).

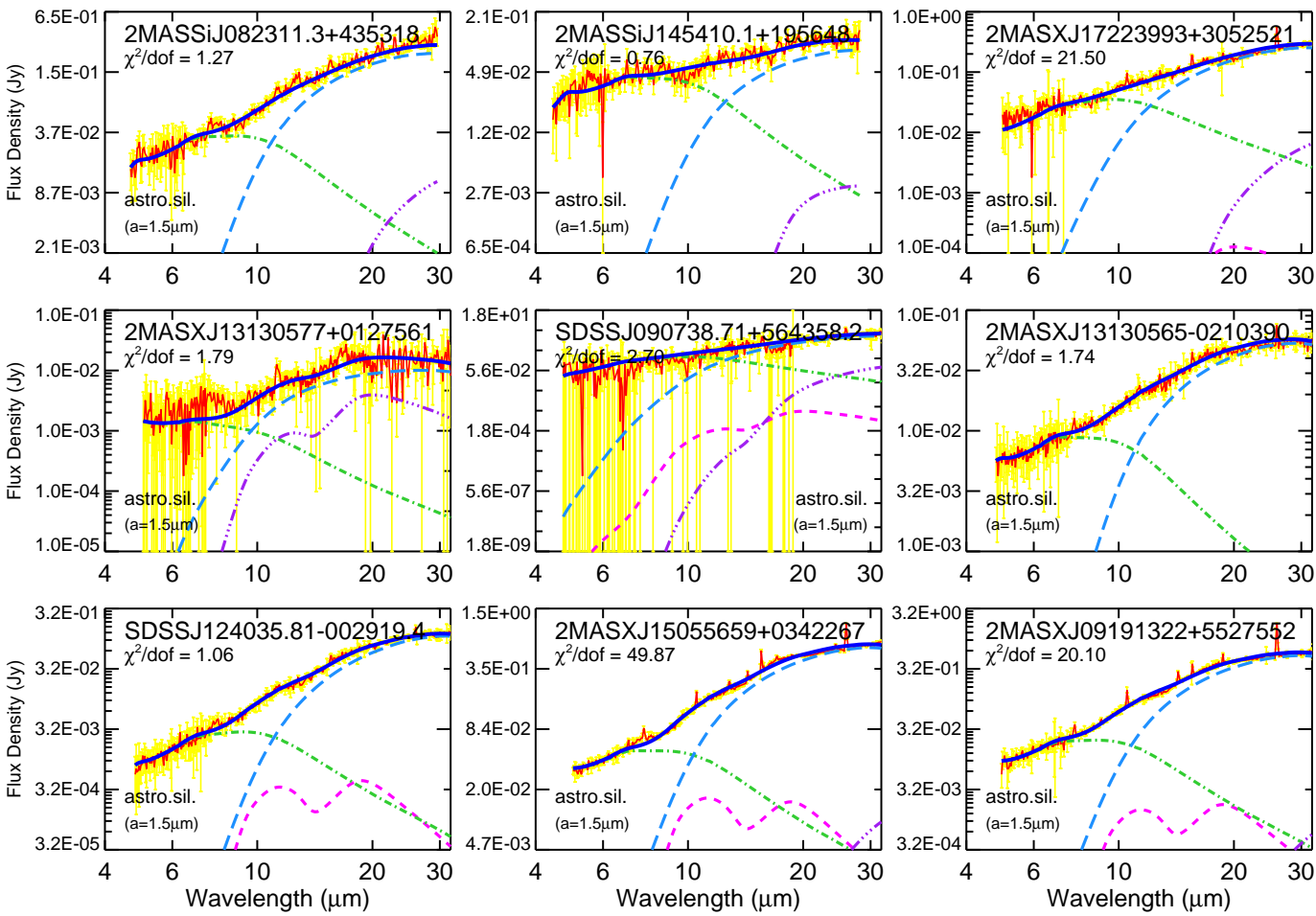


Fig. 19.— Continued, but for the 2MASS quasars 2MASSJ082311.3+435318, and 2MASSJ145410.1+195648 and the S³AGN AGNs 2MASXJ17223993+3052521, 2MASXJ13130577+0127561, SDSSJ090738.71+564358.2, 2MASXJ13130565-0210390, SDSSJ124035.81-002919.4, 2MASXJ15055659+0342267, and 2MASXJ09191322+5527552.

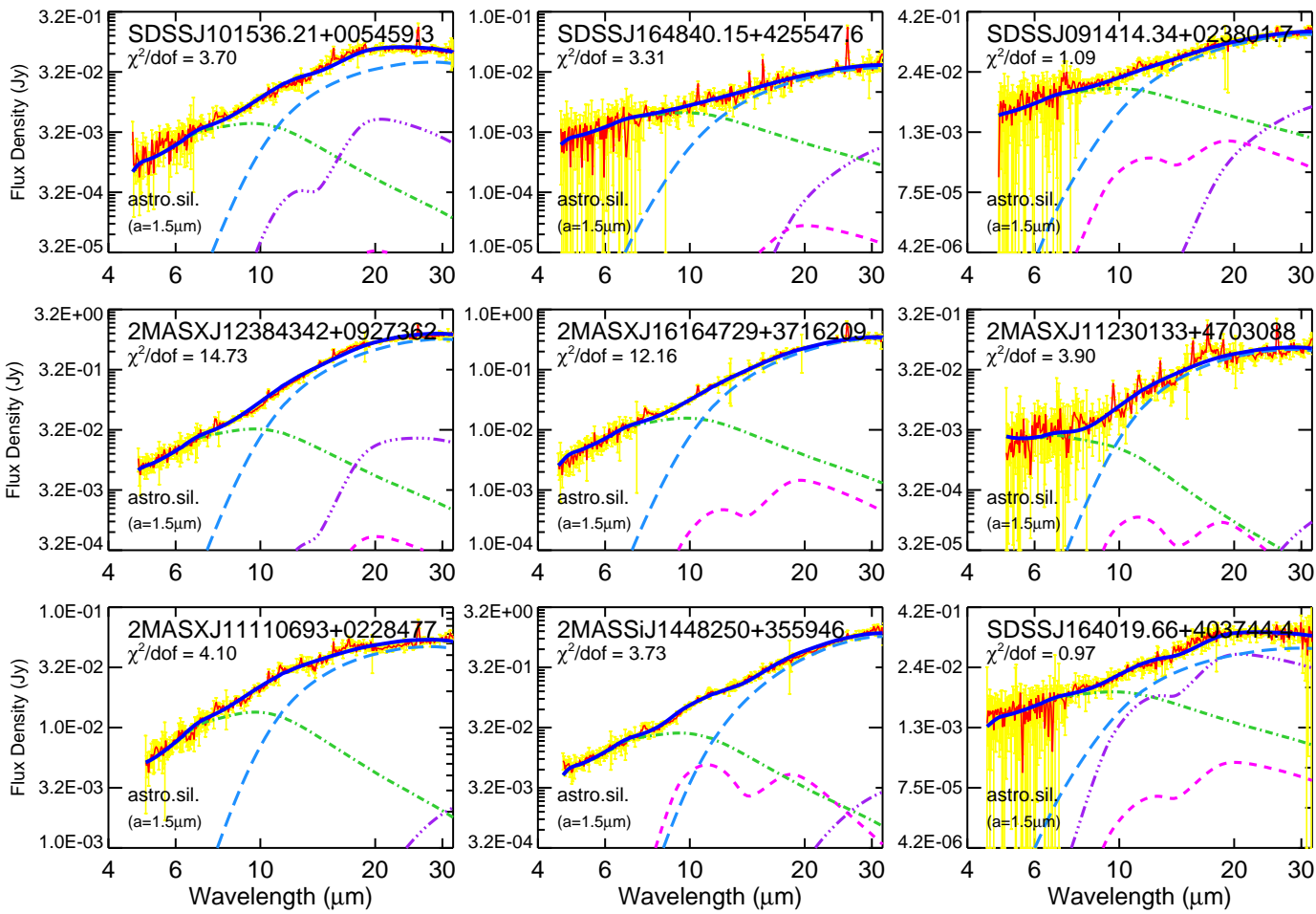


Fig. 19. — Continued, but for the S³ AGA AGNs, SDSSJ101536.21+005459.3, SDSSJ164840.15+425547.6, SDSSJ091414.34+023801.7, 2MASXJ12384342+0927362, 2MASXJ16164729+3716209, 2MASXJ11230133+4703088, 2MASXJ11110693+0228477, 2MASSJ1448250+355946, and SDSSJ164019.66+403744.4.

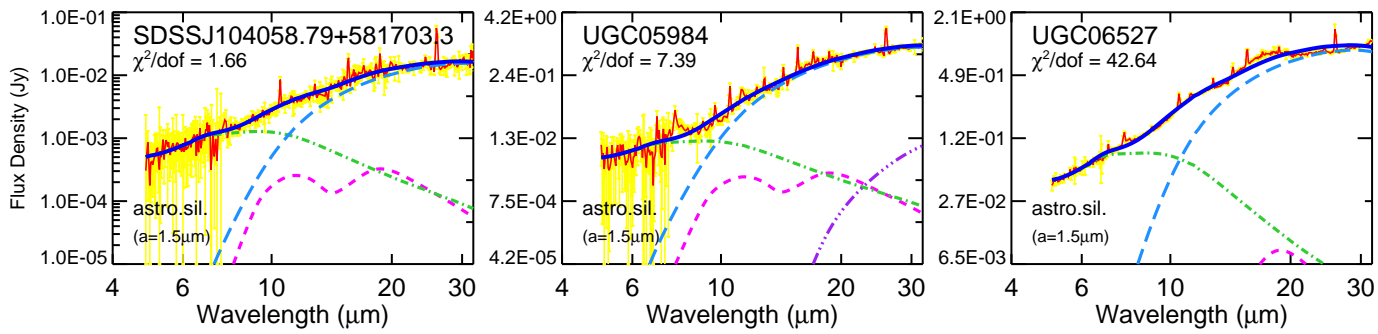


Fig. 19.— Continued, but for the S³ AGA AGNs SDSSJ104058.79+581703.3, UGC05984 and UGC06527.

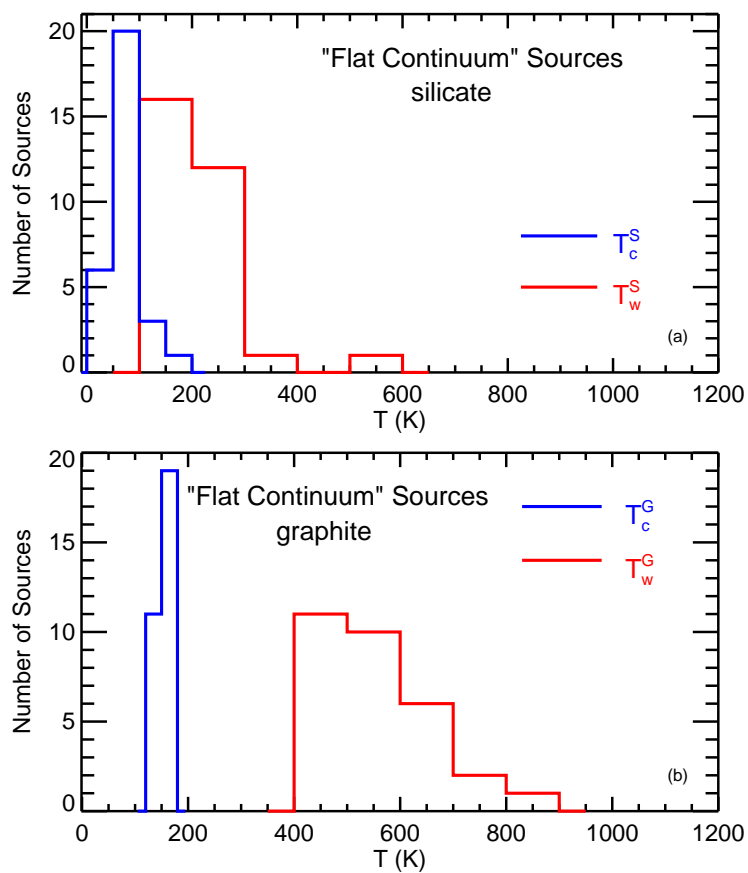


Fig. 20.— Same as Figure 8 but for those 30 “flat continuum” sources which show a featureless thermal continuum.

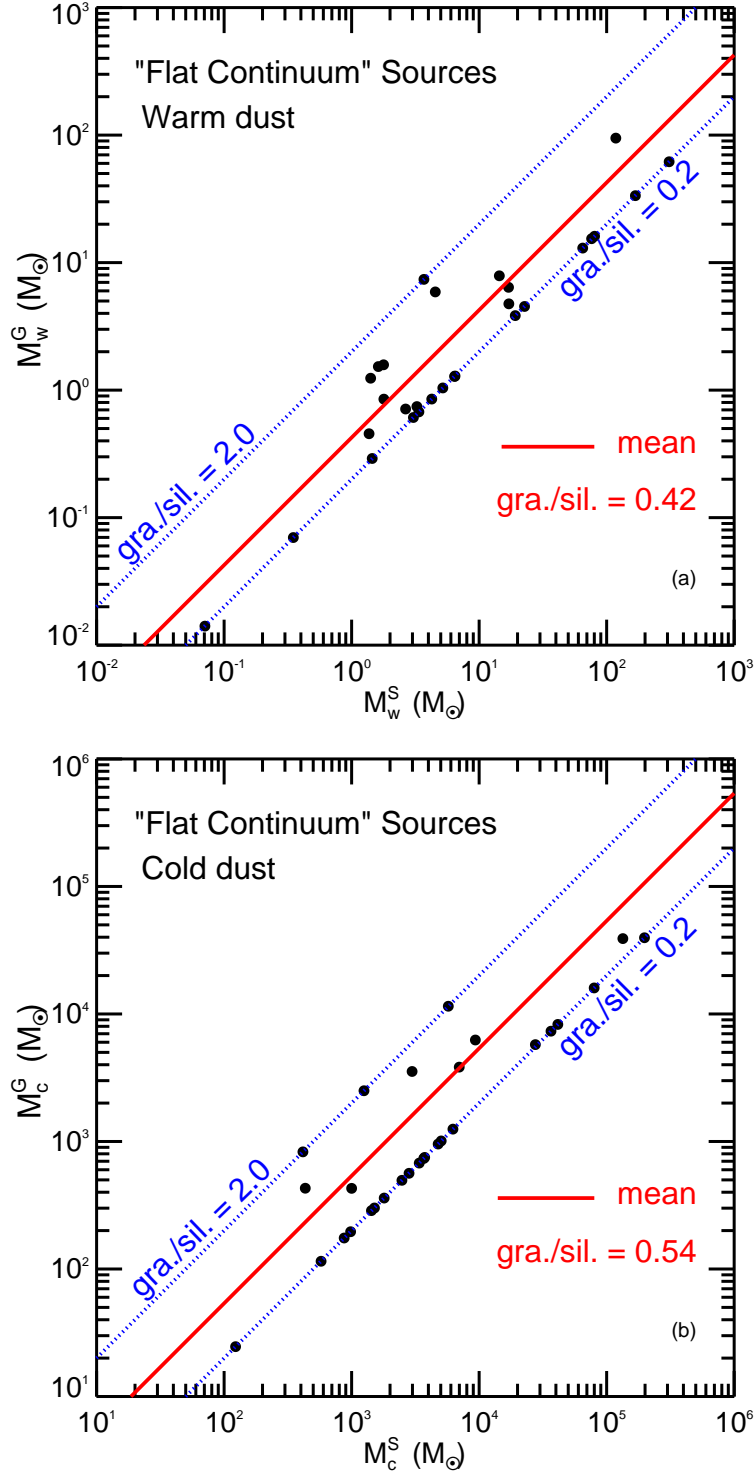


Fig. 21.— Same as Figure 10 but for the 30 "flat continuum" sources which show a featureless thermal continuum.

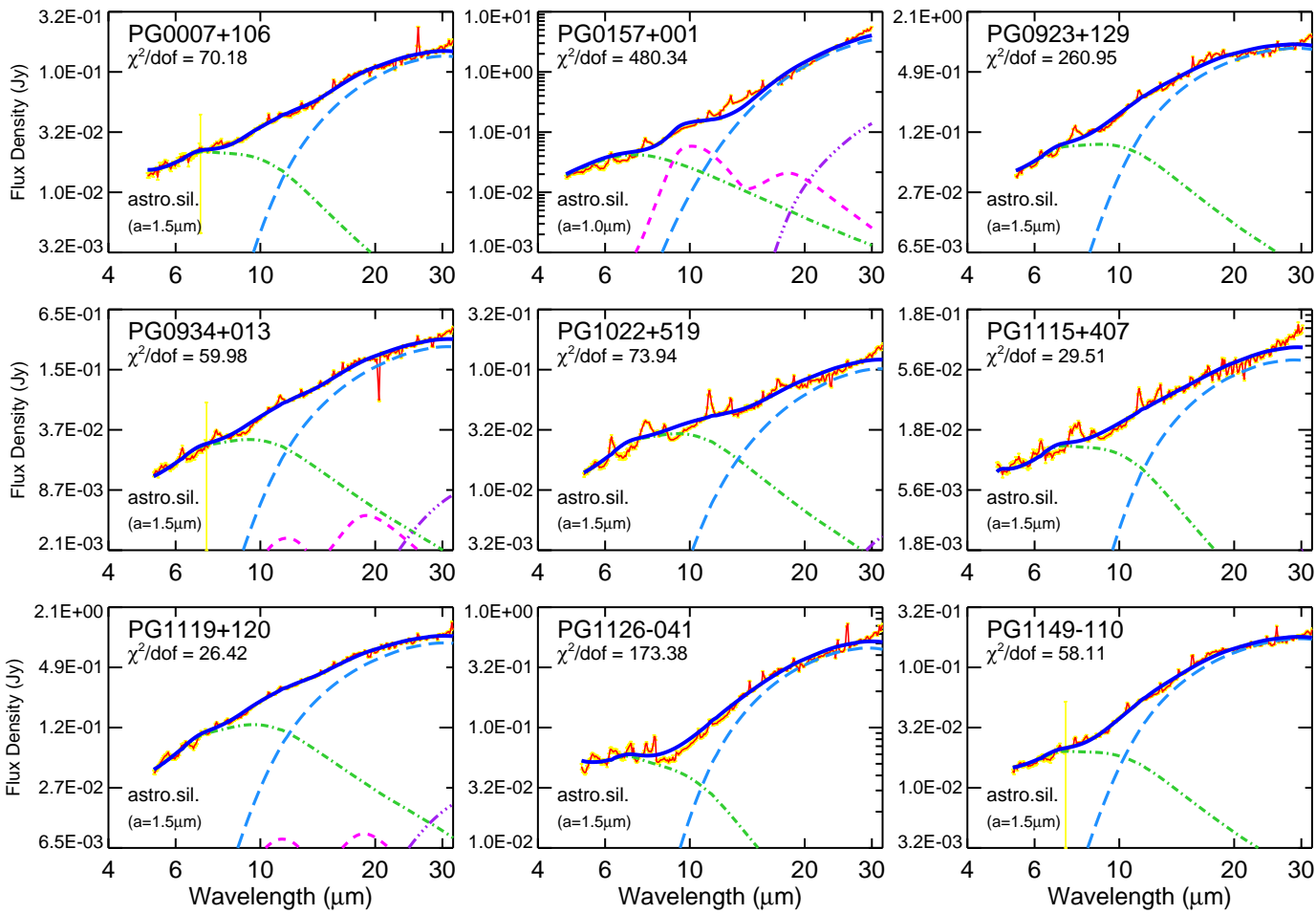


Fig. 22.— Comparison of the *Spitzer*/IRS spectra (red solid lines) of the PG quasars PG0007+106, PG0157+001, PG0923+129, PG0934+013, PG1022+519, PG1115+407, PG1119+120, PG1126-041, and PG1149-110 which show a thermal continuum superimposed by PAH features with the model spectra (blue solid lines) which are the sum of warm silicate (magenta short dashed lines), cold silicate (purple dash-dot-dotted lines), warm graphite (green dash-dotted lines), and cold graphite (light blue long dashed lines). Also shown are the observed 1σ errors (yellow vertical lines).

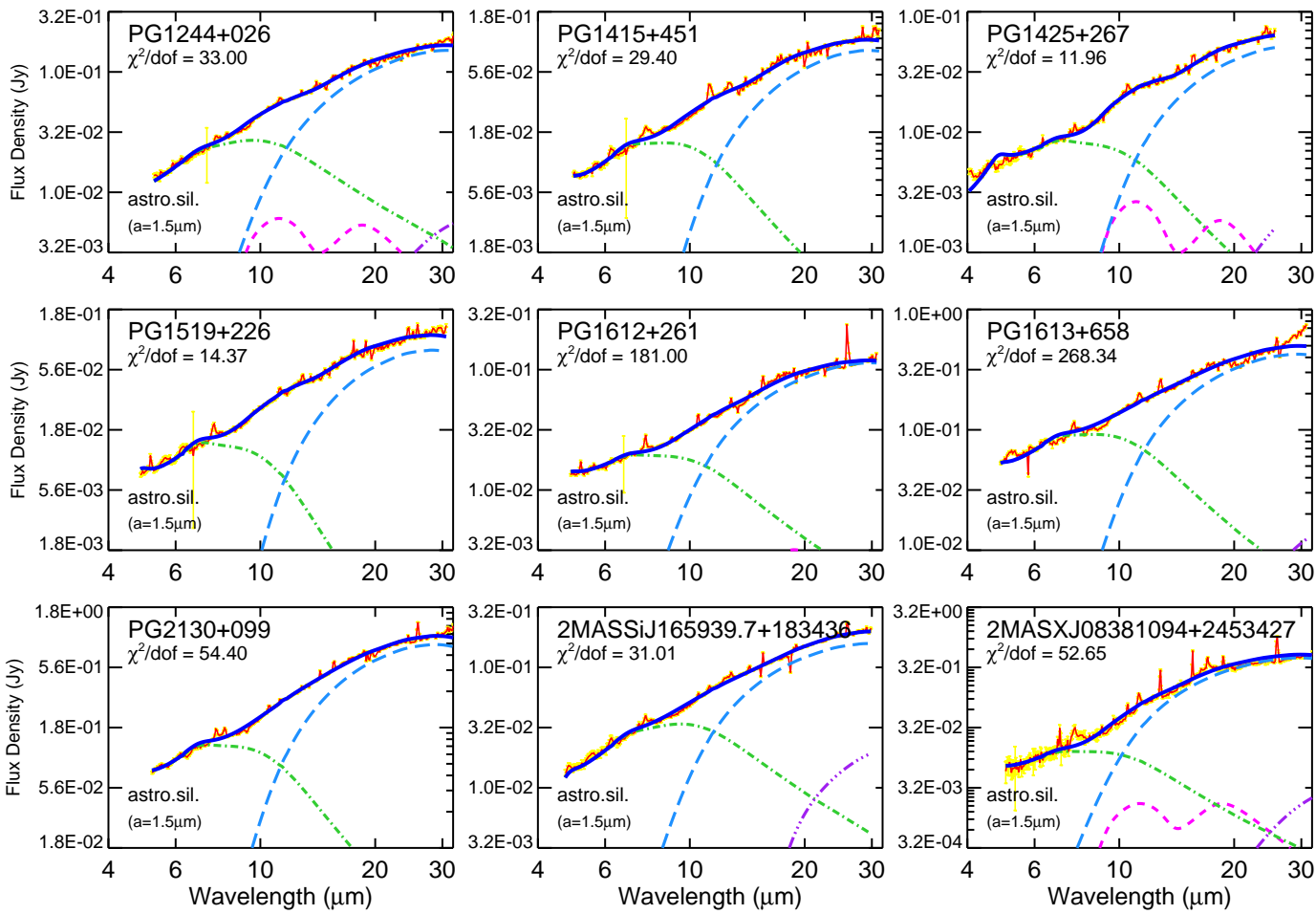


Fig. 22.— Continued, but for the PG quasars PG1244+026, PG1415+451, PG1425+267, PG1519+226, PG1612+261, PG1613+658, PG2130+099, the 2MAS quasars 2MASSJ165939.7+183436, and the S³AGN AGN 2MASXJ08381094+2453427.

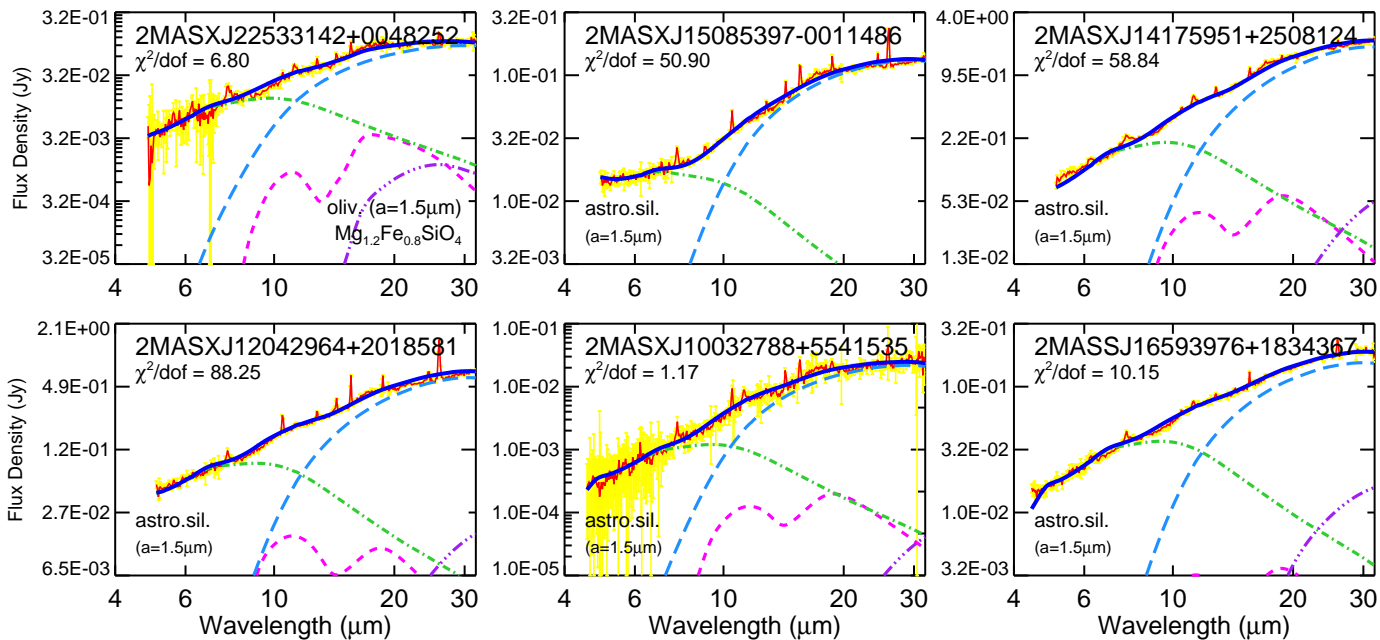


Fig. 22. — Continued, but for the S³AGN AGNs 2MASXJ22533142+0048252, 2MASXJ15085397-0011486, 2MASXJ14175951+2508124, 2MASXJ12042964+2018581, 2MASXJ10032788+5541535, and 2MASSJ16593976+1834367.

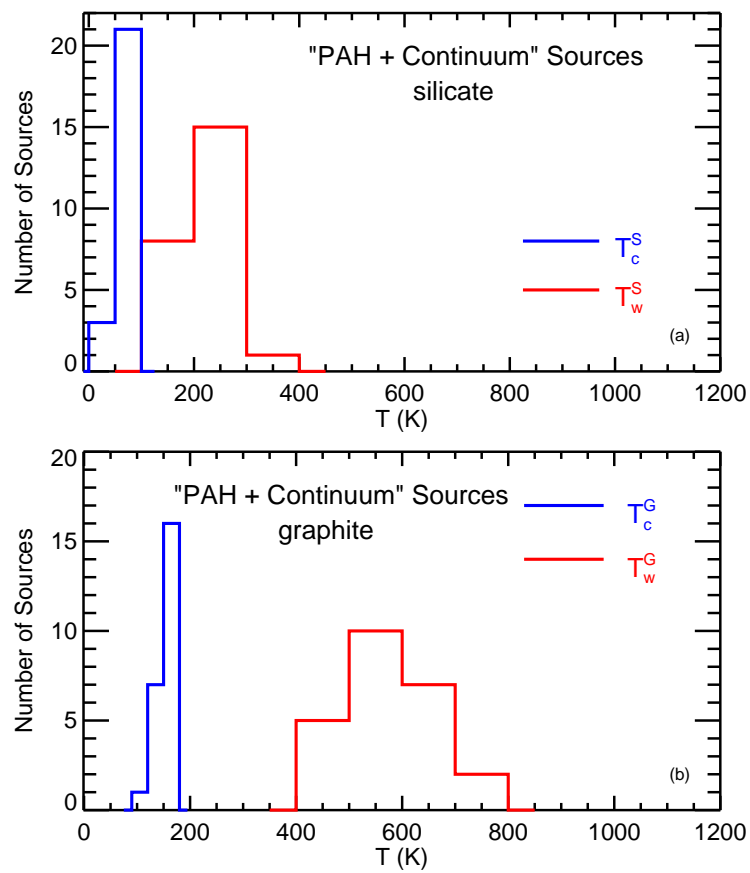


Fig. 23.— Same as Figure 8 but for those 24 sources which show a thermal continuum superimposed with PAH features.

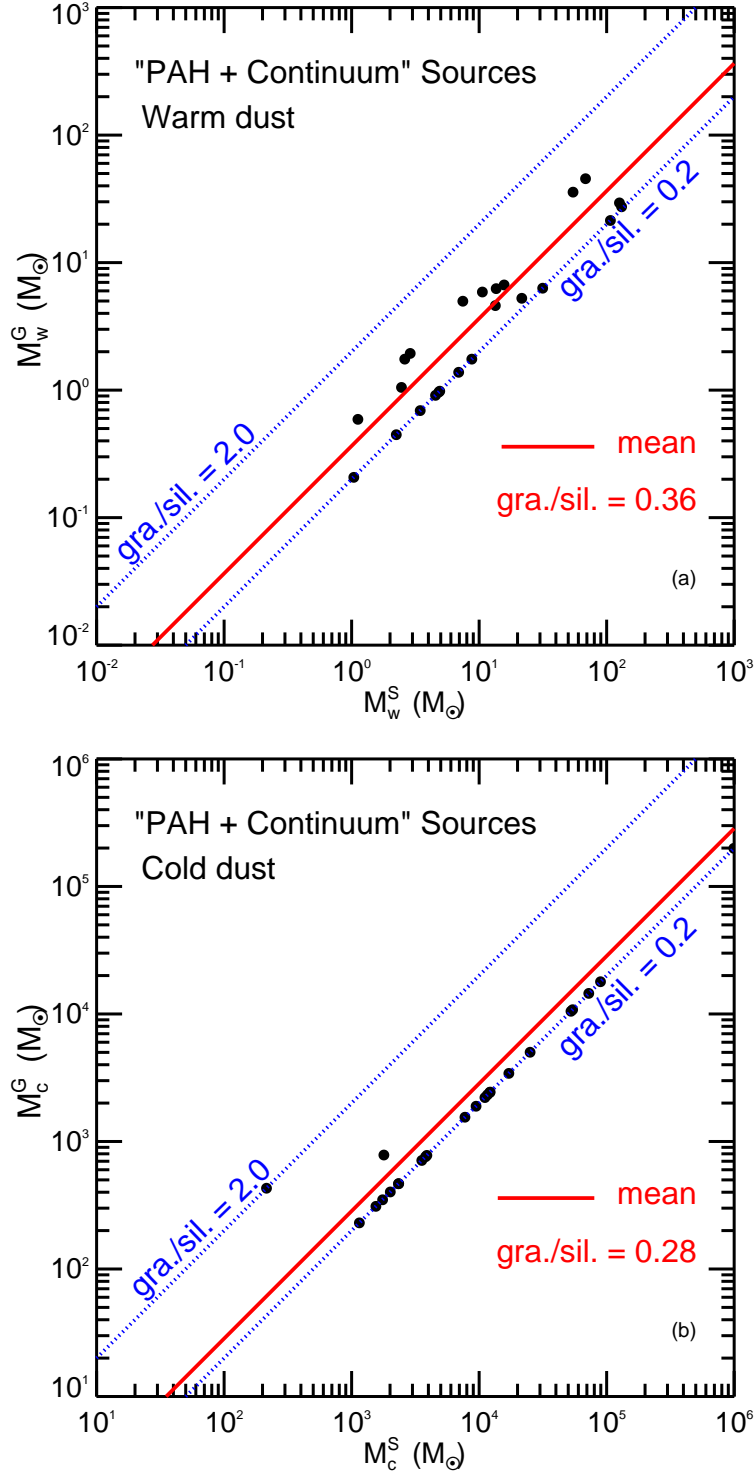


Fig. 24.— Same as Figure 10 but for the 24 sources which show a featureless thermal continuum superimposed with PAH features.

Table 4. Basic Parameters of All 93 Sources from Our PG Quasar Sample, *2MASS* Quasar Sample, and S³AGN AGN Sample. These Sources All Show Silicate Emission around 9.7 and 18 μ m.

Source	R.A.	Dec.	Redshift	Type	$\lambda L_{\lambda}(5100\text{\AA})$ (ergs s ⁻¹)	$\lg(M_{\text{BH}})$ (M _⊙)	Reference
(1)	(2)	(3)	(4)	(5)	(6)	(7)	(8)
PG0003+158	00h05m59.20s	+16d09m49.0s	0.450	1.0	46.018 ^{+0.033} _{-0.036}	9.270 ^{+0.088} _{-0.110}	Ves2006
PG0003+199	00h06m19.52s	+20d12m10.5s	0.025	1.0	43.710 ^{+0.011} _{-0.011}	7.192 ^{+0.081} _{-0.099}	Mar2003
PG0026+129	00h29m13.60s	+13d16m03.0s	0.142	1.0	44.900 ^{+0.070} _{-0.070}	7.850 ^{+0.120} _{-0.120}	N1987, Kaspi2000
PG0043+039	00h45m47.27s	+04d10m24.4s	0.384	1.0	45.537 ^{+0.030} _{-0.032}	9.123 ^{+0.085} _{-0.105}	Ves2006
PG0049+171	00h51m54.80s	+17d25m58.4s	0.064	1.0	44.004 ^{+0.011} _{-0.011}	8.347 ^{+0.079} _{-0.097}	Ves2006
PG0050+124	00h53m34.94s	+12d41m36.2s	0.061	1.0	44.794 ^{+0.097} _{-0.126}	7.441 ^{+0.093} _{-0.119}	Ves2006
PG0052+251	00h54m52.10s	+25d25m38.0s	0.155	1.0	44.870 ^{+0.070} _{-0.070}	8.720 ^{+0.100} _{-0.100}	N1987, Kaspi2000
PG0804+761	08h10m58.60s	+76d02m42.0s	0.100	1.0	44.930 ^{+0.070} _{-0.070}	8.310 ^{+0.010} _{-0.010}	N1987, Kaspi2000
PG0844+349	08h47m42.40s	+34d45m04.0s	0.064	1.0	44.380 ^{+0.010} _{-0.010}	7.975 ^{+0.082} _{-0.101}	Mar2003
PG0921+525	09h25m12.87s	+52d17m10.5s	0.035	1.0	43.550 ^{+0.120} _{-0.120}	6.910 ^{+0.120} _{-0.120}	SG1983, WPM1999
PG0923+201	09h25m54.72s	+19d54m05.1s	0.190	1.0	45.038 ^{+0.015} _{-0.019}	8.009 ^{+0.082} _{-0.101}	Ves2006
PG0947+396	09h50m48.39s	+39d26m50.5s	0.206	1.0	44.808 ^{+0.020} _{-0.021}	8.677 ^{+0.081} _{-0.099}	Ves2006
PG0953+414	09h56m52.39s	+41d15m22.3s	0.239	1.0	45.300 ^{+0.060} _{-0.060}	8.270 ^{+0.060} _{-0.090}	Ves2002
PG1001+054	10h04m20.14s	+05d13m00.5s	0.161	1.0	44.711 ^{+0.017} _{-0.017}	7.738 ^{+0.081} _{-0.099}	Ves2006
PG1004+130	10h07m26.10s	+12d48m56.2s	0.240	1.0	45.536 ^{+0.022} _{-0.023}	9.272 ^{+0.084} _{-0.104}	Ves2006
PG1011-040	10h14m20.69s	-04d18m40.5s	0.058	1.0	44.259 ^{+0.012} _{-0.012}	7.317 ^{+0.079} _{-0.097}	Ves2006
PG1012+008	10h14m54.90s	+00d33m37.4s	0.185	1.0	45.011 ^{+0.021} _{-0.022}	8.247 ^{+0.082} _{-0.101}	Ves2006
PG1048-090	10h51m29.90s	-09d18m10.0s	0.344	1.0	45.596 ^{+0.027} _{-0.029}	9.203 ^{+0.085} _{-0.105}	Ves2006
PG1049-005	10h51m51.44s	-00d51m17.7s	0.357	1.0	45.633 ^{+0.028} _{-0.030}	9.180 ^{+0.085} _{-0.106}	Ves2006
PG1048+342	10h51m43.90s	+33d59m26.7s	0.167	1.0	44.708 ^{+0.018} _{-0.019}	8.369 ^{+0.081} _{-0.099}	Ves2006
PG1100+772	11h04m13.69s	+76d58m58.0s	0.313	1.0	45.575 ^{+0.026} _{-0.027}	9.272 ^{+0.085} _{-0.105}	Ves2006
PG1103-006	11h06m31.77s	-00d52m52.5s	0.425	1.0	45.667 ^{+0.033} _{-0.036}	9.323 ^{+0.086} _{-0.107}	Ves2006
PG1114+445	11h17m06.40s	+44d13m33.3s	0.144	1.0	44.734 ^{+0.017} _{-0.017}	8.591 ^{+0.081} _{-0.099}	Ves2006
PG1116+215	11h19m08.68s	+21d19m18.0s	0.177	1.0	45.397 ^{+0.018} _{-0.019}	8.529 ^{+0.083} _{-0.103}	Ves2006
PG1121+422	11h24m39.18s	+42d01m45.0s	0.234	1.0	44.883 ^{+0.022} _{-0.023}	8.030 ^{+0.081} _{-0.100}	Ves2006
PG1151+117	11h53m49.27s	+11d28m30.4s	0.176	1.0	44.756 ^{+0.020} _{-0.021}	8.549 ^{+0.081} _{-0.099}	Ves2006
PG1202+281	12h04m42.11s	+27d54m11.8s	0.165	1.0	44.601 ^{+0.027} _{-0.029}	8.612 ^{+0.081} _{-0.099}	Ves2006
PG1211+143	12h14m17.70s	+14d03m12.6s	0.085	1.0	45.071 ^{+0.014} _{-0.014}	7.961 ^{+0.082} _{-0.101}	Ves2006
PG1216+069	12h19m20.93s	+06d38m38.5s	0.334	1.0	45.721 ^{+0.027} _{-0.028}	9.196 ^{+0.085} _{-0.106}	Ves2006
PG1229+204	12h32m03.60s	+20d09m29.2s	0.063	1.0	44.100 ^{+0.012} _{-0.012}	7.997 ^{+0.080} _{-0.098}	Mar2003
PG1259+593	13h01m12.93s	+59d02m06.7s	0.472	1.0	45.906 ^{+0.034} _{-0.037}	8.917 ^{+0.087} _{-0.109}	Ves2006
PG1302-102	13h05m33.01s	-10d33m19.4s	0.286	1.0	45.827 ^{+0.024} _{-0.026}	8.879 ^{+0.086} _{-0.107}	Ves2006
PG1307+085	13h09m47.00s	+08d19m48.2s	0.155	1.0	45.010 ^{+0.028} _{-0.028}	8.930 ^{+0.096} _{-0.123}	Mar2003
PG1309+355	13h12m17.80s	+35d15m21.0s	0.183	1.0	45.041 ^{+0.019} _{-0.020}	8.344 ^{+0.082} _{-0.100}	Ves2006
PG1310-108	13h13m05.78s	-11d07m42.4s	0.035	1.0	43.725 ^{+0.010} _{-0.011}	7.884 ^{+0.079} _{-0.097}	Ves2006
PG1322+659	13h23m49.52s	+65d41m48.2s	0.168	1.0	44.980 ^{+0.098} _{-0.126}	8.281 ^{+0.094} _{-0.120}	Ves2006
PG1341+258	13h43m56.75s	+25d38m47.7s	0.087	1.0	44.344 ^{+0.097} _{-0.126}	8.037 ^{+0.092} _{-0.117}	Ves2006
PG1351+640	13h53m15.83s	+63d45m45.7s	0.087	1.0	44.835 ^{+0.014} _{-0.015}	8.828 ^{+0.081} _{-0.099}	Ves2006
PG1352+183	13h54m35.69s	+18d05m17.5s	0.158	1.0	44.816 ^{+0.017} _{-0.017}	8.423 ^{+0.081} _{-0.099}	Ves2006
PG1402+261	14h05m16.21s	+25d55m34.1s	0.164	1.0	44.983 ^{+0.017} _{-0.018}	7.944 ^{+0.081} _{-0.100}	Ves2006
PG1404+226	14h06m21.89s	+22d23m46.6s	0.098	1.0	44.379 ^{+0.017} _{-0.018}	6.889 ^{+0.080} _{-0.098}	Ves2006
PG1411+442	14h13m48.33s	+44d00m14.0s	0.089	1.0	44.620 ^{+0.014} _{-0.014}	8.080 ^{+0.086} _{-0.107}	Mar2003
PG1416-129	14h19m03.80s	-13d10m44.0s	0.129	1.0	45.135 ^{+0.037} _{-0.041}	9.045 ^{+0.083} _{-0.103}	Ves2006
PG1426+015	14h29m06.59s	+01d17m06.5s	0.086	1.0	44.740 ^{+0.070} _{-0.070}	8.750 ^{+0.100} _{-0.100}	N1987, Kaspi2000
PG1435-067	14h38m16.16s	-06d58m21.3s	0.129	1.0	44.918 ^{+0.036} _{-0.040}	8.365 ^{+0.082} _{-0.102}	Ves2006
PG1444+407	14h46m45.94s	+40d35m05.8s	0.267	1.0	45.203 ^{+0.023} _{-0.023}	8.289 ^{+0.083} _{-0.102}	Ves2006
PG1512+370	15h14m43.04s	+36d50m50.4s	0.371	1.0	45.602 ^{+0.030} _{-0.032}	9.373 ^{+0.085} _{-0.106}	Ves2006
PG1534+580	15h35m52.36s	+57d54m09.2s	0.030	1.0	43.687 ^{+0.010} _{-0.010}	8.203 ^{+0.080} _{-0.097}	Ves2006
PG1535+547	15h36m38.36s	+54d33m33.2s	0.038	1.0	43.961 ^{+0.010} _{-0.011}	7.192 ^{+0.079} _{-0.097}	Ves2006

Table 4—Continued

Source	R.A.	Dec.	Redshift	Type	$\lambda L_{\lambda}(5100\text{\AA})$ (ergs s^{-1})	$\lg(M_{\text{BH}})$ (M_{\odot})	Reference
(1)	(2)	(3)	(4)	(5)	(6)	(7)	(8)
PG1545+210	15h47m43.54s	+20d52m16.6s	0.266	1.0	$45.428^{+0.023}_{-0.024}$	$9.314^{+0.084}_{-0.104}$	Ves2006
PG1552+085	15h54m44.58s	+08d22m21.5s	0.119	1.0	$44.407^{+0.015}_{-0.015}$	$7.537^{+0.080}_{-0.099}$	Ves2006
PG1617+175	16h20m11.29s	+17d24m27.7s	0.114	1.0	$44.375^{+0.069}_{-0.082}$	$8.436^{+0.115}_{-0.191}$	Kaspi2000
PG1626+554	16h27m56.12s	+55d22m31.5s	0.133	1.0	$44.580^{+0.026}_{-0.028}$	$8.498^{+0.081}_{-0.099}$	Ves2006
PG1700+518	17h01m24.80s	+51d49m20.0s	0.292	1.0	$45.470^{+0.010}_{-0.010}$	$8.427^{+0.109}_{-0.146}$	Mar2003
PG1704+608	17h04m41.38s	+60d44m30.5s	0.371	1.0	$45.702^{+0.030}_{-0.032}$	$9.391^{+0.086}_{-0.107}$	Ves2006
PG2112+059	21h14m52.57s	+06d07m42.5s	0.466	1.0	$46.181^{+0.034}_{-0.037}$	$9.001^{+0.089}_{-0.112}$	Ves2006
PG2209+184	22h11m53.89s	+18d41m49.9s	0.070	1.0	$44.469^{+0.012}_{-0.013}$	$8.766^{+0.080}_{-0.098}$	Ves2006
PG2214+139	22h17m12.26s	+14d14m20.9s	0.067	1.0	$44.662^{+0.097}_{-0.126}$	$8.551^{+0.093}_{-0.118}$	Ves2006
PG2233+134	22h36m07.68s	+13d43m55.3s	0.325	1.0	$45.327^{+0.027}_{-0.028}$	$8.036^{+0.083}_{-0.103}$	Ves2006
PG2251+113	22h54m10.40s	+11d36m38.3s	0.323	1.0	$45.692^{+0.026}_{-0.028}$	$8.989^{+0.085}_{-0.106}$	Ves2006
PG2304+042	23h07m02.91s	+04d32m57.2s	0.042	1.0	$44.066^{+0.097}_{-0.126}$	$8.564^{+0.092}_{-0.117}$	Ves2006
PG2308+098	23h11m17.76s	+10d08m15.5s	0.432	1.0	$45.777^{+0.101}_{-0.131}$	$9.592^{+0.098}_{-0.126}$	Ves2006
2MASSJ081652.2+425829	08h16m52.24s	+42d58m29.4s	0.235	1.0	$44.605^{+0.002}_{-0.002}$	$8.27^{+0.01}_{-0.01}$	Shen2011
2MASSJ095504.5+170556	09h55m04.55s	+17d05m56.4s	0.139	1.0	$45.130^{+0.000}_{-0.002}$	$7.27^{+0.38}_{-0.38}$	Shen2011
2MASSJ130005.3+163214	13h00m05.35s	+16d32m14.8s	0.080	1.0	—	—	—
2MASSJ132917.5+121340	13h29m17.52s	+12d13m40.2s	0.203	1.0	—	—	—
2MASSJ1402511+263117	14h02m51.20s	+26d31m17.6s	0.187	1.0	$44.565^{+0.039}_{-0.039}$	$8.57^{+0.03}_{-0.03}$	Shen2011
2MASSJ145608.6+275008	14h56m08.65s	+27d50m08.8s	0.250	1.0	$44.670^{+0.015}_{-0.015}$	$7.95^{+0.01}_{-0.01}$	Shen2011
2MASSJ151653.2+190048	15h16m53.23s	+19d00m48.3s	0.190	1.0	$44.200^{+0.000}_{-0.000}$	$8.22^{+0.00}_{-0.00}$	Shen2011
2MASSJ151901.5+183804	15h19m01.48s	+18d38m04.9s	0.187	1.0	—	—	—
2MASSJ154307.7+193751	15h43m07.78s	+19d37m51.8s	0.228	1.5	—	—	—
2MASSJ222221.1+195947	22h22m21.14s	+19d59m47.1s	0.211	1.0	—	—	—
2MASSJ223742.6+145614	22h37m42.60s	+14d56m14.0s	0.277	1.0	—	—	—
2MASSJ234259.3+134750	23h42m59.36s	+13d47m50.4s	0.299	1.5	$44.682^{+0.005}_{-0.005}$	$8.41^{+0.02}_{-0.02}$	Shen2011
2MASSJ234449.5+122143	23h44m49.56s	+12d21m43.1s	0.199	1.0	—	—	—
2MASXJ09210862+4538575	09h21m08.06s	+45d38m57.0s	0.175	1.0	$43.972^{+0.004}_{-0.004}$	$8.83^{+0.04}_{-0.04}$	Shen2011
2MASXJ00370409-0109081	00h37m04.01s	-01d09m08.0s	0.074	1.0	$45.170^{+0.000}_{-0.000}$	$8.44^{+0.50}_{-0.50}$	Shen2011
2MASXJ02335161+0108136	02h33m51.60s	+01d08m14.0s	0.022	1.0	—	—	—
2MASXJ07582810+3747121	07h58m28.01s	+37d47m12.0s	0.041	1.0	$45.330^{+0.000}_{-0.000}$	$8.90^{+0.53}_{-0.53}$	Tri2013
2MASXJ0208238-002000	02h08m23.08s	-00d20m01.0s	0.074	1.0	—	—	—
2MASXJ02061600-0017292	02h06m16.00s	-00d17m29.0s	0.043	1.0	$43.850^{+0.000}_{-0.000}$	$8.18^{+0.00}_{-0.00}$	Du2014
2MASXJ10493088+2257523	10h49m30.90s	+22d57m52.0s	0.033	1.0	—	—	—
2MASXJ12485992-0109353	12h48m59.90s	-01d09m35.0s	0.089	1.0	—	—	—
2MASXJ14070036+2827141	14h07m00.40s	+28d27m15.0s	0.077	1.0	—	—	—
2MASXJ02143357-0046002	02h14m33.50s	-00d46m00.0s	0.026	1.0	—	—	—
2MASXJ09234300+2254324	09h23m43.00s	+22d54m33.0s	0.033	1.0	$45.104^{+0.000}_{-0.000}$	$7.58^{+0.04}_{-0.04}$	Dasyra.2011
2MASXJ12170991+0711299	12h17m09.90s	+07d11m30.0s	0.008	1.0	$42.080^{+0.000}_{-0.000}$	$7.71^{+0.00}_{-0.00}$	Woo2012
2MASXJ12232410+0240449	12h23m24.10s	+02d40m45.0s	0.024	1.0	$42.830^{+0.006}_{-0.006}$	$7.51^{+0.07}_{-0.07}$	HK2014
2MASXJ13381586+0432330	13h38m15.90s	+04d32m33.0s	0.023	1.0	$45.146^{+0.000}_{-0.000}$	$7.56^{+0.00}_{-0.00}$	WZ2007
2MASXJ13495283+0204456	13h49m52.80s	+02d04m45.0s	0.033	1.0	$42.394^{+0.000}_{-0.000}$	$6.66^{+0.00}_{-0.00}$	Zhu2010
2MASXJ23044349-0841084	23h04m43.50s	-08d41m09.0s	0.047	1.0	$43.720^{+0.000}_{-0.000}$	$8.47^{+0.00}_{-0.00}$	WL2004
SDSSJ115138.24+004946.4	11h51m38.20s	+00d49m47.0s	0.195	1.0	$42.790^{+0.040}_{-0.040}$	$6.00^{+0.00}_{-0.00}$	GH2008
SDSSJ170246.09+602818.8	17h02m46.10s	+60d28m19.0s	0.069	1.0	—	—	—

Note. — Column (1): AGN name; Column (2): Right ascension of the AGN; Column (3): Declination of the AGN; Column (4): Redshift z ; Column (5): Optical classification derived from the emission line ratio of the AGN: “1.0” for type 1 AGN with broad emission

lines, “2.0” for type 2 AGN with only narrow emission lines, values between 1.0 and 2.0 for intermediate types; Column (6): Power emitted at $\lambda = 5100 \text{ \AA}$; Column (7): Black hole mass (in unit of solar mass M_{\odot}); Column (8): References from which we collect $\lambda L_{\lambda}(5100 \text{ \AA})$ and M_{BH} — N1987 = Neugebauer et al. (1987); Mar2003 = Marziani et al. (2003); SG1983 = Schmidt & Green (1983); WPM1999 = Wandel, Peterson & Malkan (1999); Kaspi2000 = Kaspi et al. (2000); WL2004 = Wu & Liu (2004); WZ2007 = Wang & Zhang (2007); GH2008 = Greene & Ho (2008); Ves2006 = Vestergaard et al. (2006); Dong2010 = Dong et al. (2010); Sani2010 = Sani et al. (2010); Zhu2010 = Zhu et al. (2010); Dasyra2011 = Dasyra et al. (2011); Shen2011 = Shen et al. (2011); Woo2012 = Woo et al. (2012); Tri2013 = Trichas et al. (2013); Rose2013 = Rose et al. (2013); Du2014 = Du et al. 2014; HK2014 = Ho & Kim (2014).

Table 5. Basic Parameters of 30 Sources from Our PG Quasar Sample, *2MASS* Quasar Sample, and S³AGA AGN Sample Which Show No Silicate Emission but a Featureless Thermal Continuum

Source	R.A.	Dec.	Redshift	Type	$\lambda L_{\lambda}(5100\text{\AA})$ (ergs s ⁻¹)	$\lg(M_{\text{BH}})$ (M_{\odot})	Reference
(1)	(2)	(3)	(4)	(5)	(6)	(7)	(8)
PG0838+770	08h44m45.26s	+76d53m09.5s	0.131	1.0	44.727 ^{+0.015} _{-0.015}	8.154 ^{+0.080} _{-0.099}	Ves2006
PG1226+023	12h29m06.70s	+02d03m08.6s	0.158	1.0	46.060 ^{+0.014} _{-0.014}	9.262 ^{+0.130} _{-0.186}	Mar2003
PG1354+213	13h56m32.80s	+21d03m52.4s	0.300	1.0	44.977 ^{+0.072} _{-0.086}	8.627 ^{+0.088} _{-0.110}	Ves2006
PG1427+480	14h29m43.07s	+47d47m26.2s	0.221	1.0	44.759 ^{+0.021} _{-0.022}	8.088 ^{+0.081} _{-0.099}	Ves2006
PG1448+273	14h51m08.76s	+27d09m26.9s	0.065	1.0	44.482 ^{+0.011} _{-0.011}	6.970 ^{+0.080} _{-0.098}	Ves2006
PG1501+106	15h04m01.20s	+10d26m16.2s	0.036	1.0	44.285 ^{+0.010} _{-0.011}	8.523 ^{+0.079} _{-0.097}	Ves2006
PG1543+489	15h45m30.24s	+48d46m09.1s	0.400	1.0	45.445 ^{+0.037} _{-0.041}	7.998 ^{+0.085} _{-0.105}	Ves2006
2MASSJ010835.1+214818	01h08m35.10s	+21d48m18.0s	0.285	1.9	—	—	—
2MASSJ024807.3+145957	02h48m07.36s	+14d59m57.7s	0.072	1.0	43.910 ^{+0.170} _{-0.170}	7.46 ^{+0.00} _{-0.00}	Rose2013
2MASSJ082311.3+435318	08h23m11.27s	+43d53m18.5s	0.182	1.5	—	—	—
2MASSJ145410.1+195648	14h54m10.17s	+19d56m48.7s	0.243	1.9	—	—	—
2MASXJ17223993+3052521	17h22m39.90s	+30d52m53.0s	0.043	1.0	—	—	—
2MASXJ13130577+0127561	13h13m05.80s	+01d27m56.0s	0.029	1.0	—	—	—
2MASXJ13130565-0210390	13h13m05.70s	-02d10m39.0s	0.084	1.0	—	—	—
2MASXJ15055659+0342267	15h05m56.50s	+03d42m26.0s	0.036	1.0	43.450 ^{+0.000} _{-0.000}	7.55 ^{+0.00} _{-0.00}	Dong2010
2MASXJ09191322+5527552	09h19m13.20s	+55d27m55.0s	0.049	1.0	—	—	—
2MASXJ12384342+0927362	12h38m43.40s	+09d27m37.0s	0.083	1.0	—	—	—
2MASXJ16164729+3716209	16h16m47.30s	+37d16m21.0s	0.152	1.0	—	—	—
2MASXJ11230133+4703088	11h23m01.30s	+47d03m09.0s	0.025	1.0	—	—	—
2MASXJ11110693+0228477	11h11m06.90s	+02d28m48.0s	0.035	1.0	—	—	—
2MASSJ1448250+355946	14h48m25.10s	+35d59m47.0s	0.113	1.0	—	—	—
SDSSJ090738.71+564358.2	09h07m38.70s	+56d43m58.0s	0.099	1.0	—	—	—
SDSSJ124035.81-002919.4	12h40m35.80s	-00d29m19.0s	0.081	1.0	—	—	—
SDSSJ101536.21+005459.3	10h15m36.20s	+00d54m59.0s	0.120	2.0	—	—	—
SDSSJ164840.15+425547.6	16h48m40.10s	+42d55m48.0s	0.129	1.0	—	—	—
SDSSJ091414.34+023801.7	09h14m14.30s	+02d38m02.0s	0.073	2.0	—	—	—
SDSSJ164019.66+403744.4	16h40m19.70s	+40d37m45.0s	0.151	1.0	—	—	—
SDSSJ104058.79+581703.3	10h40m58.70s	+58d17m04.0s	0.071	1.0	—	—	—
UGC05984	10h52m16.70s	+30d03m55.0s	0.035	2.0	—	—	—
UGC06527	11h32m37.60s	+52d56m53.0s	0.026	1.0	—	—	—

Note. — Column (1): AGN name; Column (2): Right ascension of the AGN; Column (3): Declination of the AGN; Column (4): Redshift z ; Column (5): Optical classification derived from the emission line ratio of the AGN: “1.0” for type 1 AGN with broad emission lines, “2.0” for type 2 AGN with only narrow emission lines, values between 1.0 and 2.0 for intermediate types; Column (6): Power at $\lambda = 5100 \text{ \AA}$; Column (7): Black hole mass (in unit of solar mass M_{\odot}); Column (8): References from which we collect $\lambda L_{\lambda}(5100 \text{ \AA})$ and M_{BH} — Mar2003 = Marziani et al. (2003); Ves2006 = Vestergaard et al. (2006); Dong2010 = Dong et al. (2010); Rose2013 = Rose et al. (2013).

Table 6. Basic Parameters of 24 Sources from Our PG Quasar Sample, *2MASS* Quasar Sample, and S³AGA AGN Sample Which Show a Thermal Continuum Superimposed with PAH Features

Source	R.A.	Dec.	Redshift	Type	$\lambda L_{\lambda}(5100\text{\AA})$ (ergs s ⁻¹)	$\lg(M_{\text{BH}})$ (M _⊙)	Reference
(1)	(2)	(3)	(4)	(5)	(6)	(7)	(8)
PG0007+106	00h10m31.01s	+10d58m29.5s	0.089	1.0	44.816 ^{+0.014} _{-0.015}	8.728 ^{+0.081} _{-0.099}	Ves2006
PG0157+001	01h59m50.21s	+00d23m40.6s	0.164	1.0	44.975 ^{+0.017} _{-0.018}	8.166 ^{+0.081} _{-0.100}	Ves2006
PG0923+129	09h26m03.29s	+12d44m03.6s	0.029	1.0	43.860 ^{+0.097} _{-0.125}	8.598 ^{+0.092} _{-0.117}	Ves2006
PG0934+013	09h37m01.03s	+01d05m43.5s	0.050	1.0	43.875 ^{+0.097} _{-0.126}	7.041 ^{+0.092} _{-0.117}	Ves2006
PG1022+519	10h25m31.28s	+51d40m34.9s	0.045	1.0	43.696 ^{+0.097} _{-0.126}	7.145 ^{+0.092} _{-0.117}	Ves2006
PG1115+407	11h18m30.29s	+40d25m54.0s	0.154	1.0	44.619 ^{+0.017} _{-0.018}	7.667 ^{+0.080} _{-0.099}	Ves2006
PG1119+120	11h21m47.10s	+11d44m18.3s	0.049	1.0	44.132 ^{+0.012} _{-0.012}	7.470 ^{+0.079} _{-0.097}	Ves2006
PG1126-041	11h29m16.66s	-04d24m07.6s	0.060	1.0	44.385 ^{+0.012} _{-0.012}	7.749 ^{+0.080} _{-0.098}	Ves2006
PG1149-110	11h52m03.54s	-11d22m24.3s	0.049	1.0	44.107 ^{+0.097} _{-0.126}	7.924 ^{+0.092} _{-0.117}	Ves2006
PG1244+026	12h46m35.25s	+02d22m08.8s	0.048	1.0	43.801 ^{+0.030} _{-0.032}	6.523 ^{+0.080} _{-0.099}	Ves2006
PG1415+451	14h17m00.70s	+44d56m06.0s	0.114	1.0	44.561 ^{+0.017} _{-0.018}	8.014 ^{+0.080} _{-0.098}	Ves2006
PG1425+267	14h27m35.61s	+26d32m14.5s	0.366	1.0	45.761 ^{+0.100} _{-0.130}	9.734 ^{+0.097} _{-0.126}	Ves2006
PG1519+226	15h21m14.26s	+22d27m43.9s	0.137	1.0	44.710 ^{+0.019} _{-0.020}	7.942 ^{+0.081} _{-0.099}	Ves2006
PG1612+261	16h14m13.20s	+26d04m16.2s	0.131	1.0	44.717 ^{+0.026} _{-0.028}	8.058 ^{+0.081} _{-0.100}	Ves2006
PG1613+658	16h13m57.18s	+65d43m09.6s	0.129	1.0	44.650 ^{+0.070} _{-0.070}	8.990 ^{+0.10} _{-0.10}	N1987, Kaspi2000
PG2130+099	21h32m27.81s	+10d08m19.5s	0.063	1.0	44.280 ^{+0.011} _{-0.011}	7.947 ^{+0.081} _{-0.099}	Mar2003
2MASSJ165939.7+183436	16h59m39.77s	+18d34m36.8s	0.170	1.0	44.241 ^{+0.006} _{-0.006}	8.950 ^{+0.03} _{-0.03}	Shen2011
2MASXJ08381094+2453427	08h38m10.90s	+24d53m43.0s	0.029	1.0	—	—	—
2MASXJ22533142+0048252	22h53m31.40s	+00d48m26.0s	0.072	1.0	—	—	—
2MASXJ15085397-0011486	15h08m53.90s	-00d11m49.0s	0.054	1.0	—	—	—
2MASXJ14175951+2508124	14h17m59.50s	+25d08m12.0s	0.016	1.0	—	—	—
2MASXJ12042964+2018581	12h04m29.70s	+20d18m58.0s	0.023	1.0	—	—	—
2MASXJ10032788+5541535	10h03m27.90s	+55d41m54.0s	0.146	2.0	—	—	—
2MASSJ16593976+1834367	16h59m39.80s	+18d34m37.0s	0.171	1.0	—	—	—

Note. — Column (1): AGN name; Column (2): Right ascension of the AGN; Column (3): Declination of the AGN; Column (4): Redshift z ; Column (5): Optical classification derived from the emission line ratio of the AGN: “1.0” for type 1 AGN with broad emission lines, “2.0” for type 2 AGN with only narrow emission lines, values between 1.0 and 2.0 for intermediate types; Column (6): Power at $\lambda = 5100 \text{ \AA}$; Column (7): Black hole mass (in unit of solar mass M_{\odot}); Column (8): References from which we collect $\lambda L_{\lambda}(5100 \text{ \AA})$ and M_{BH} — N1987 = Neugebauer et al. (1987); Mar2003 = Marziani et al. (2003) Kaspi2000 = Kaspi et al. (2000); Ves2006 = Vestergaard et al. (2006); Shen2011 = Shen et al. (2011).